ELECTRICAL AND OPTICAL STUDIES ON CARBON NANOTUBE ARRAYS

BY

TANER OZEL

DISSERTATION

Submitted in partial fulfillment of the requirements
for the degree of Doctor of Philosophy in Physics
in the Graduate College of the
University of Illinois at Urbana-Champaign, 2009

Urbana, Illinois

Doctoral Committee:

Professor James N. Eckstein, Chair
Associate Professor Moonsub Shim, Director of Research
Professor Paul M. Goldbart
Professor John D. Stack

ABSTRACT

Single-walled carbon nanotubes (SWNTs) have been studied as a prominent class of high performance electronic materials for next generation electronics. Their geometry dependent electronic structure, ballistic transport and low power dissipation due to quasi one dimensional transport, and their capability of carrying high current densities are some of the main reasons for the optimistic expectations on SWNTs. However, device applications of individual SWNTs have been hindered by uncontrolled variations in characteristics and lack of scalable methods to integrate SWNTs into electronic devices. One relatively new direction in SWNT electronics, which avoids these issues, is using arrays of SWNTs, where the ensemble average may provide uniformity from device to device, and this new breed of electronic material can be integrated into electronic devices in a scalable fashion.

This dissertation describes (1) methods for characterization of SWNT arrays, (2) how the electrical transport in these two-dimensional arrays depend on length scales and spatial anisotropy, (3) the interaction of aligned SWNTs with the underlying substrate, and (4) methods for scalable integration of SWNT arrays into electronic devices. The electrical characterization of SWNT arrays have been realized by polymer electrolyte-gated SWNT thin film transistors (TFTs). Polymer electrolyte-gating addresses many technical difficulties inherent to electrical characterization by gating through oxide-dielectrics. Having shown polymer electrolyte-gating can be successfully applied on SWNT arrays, we have studied the length scaling dependence of electrical transport in SWNT arrays. Ultrathin films formed by sub-monolayer surface coverage of SWNT

arrays are very interesting systems in terms of the physics of two-dimensional electronic transport. We have observed that they behave qualitatively different than the classical conducting films, which obey the Ohm's law. The resistance of an ultrathin film of SWNT arrays is indeed non-linear with the length of the film, across which the transport occurs. More interestingly, a transition between conducting and insulating states is observed at a critical surface coverage, which is called percolation limit. The surface coverage of conducting SWNTs can be manipulated by turning on and off the semiconductors in the SWNT array, leading to the operation principle of SWNT TFTs. The percolation limit depends also on the length and the spatial orientation of SWNTs. We have also observed that the percolation limit increases abruptly for aligned arrays of SWNTs, which are grown on single crystal quartz substrates. In this dissertation, we also compare our experimental results with a two-dimensional stick network model, which gives a good qualitative picture of the electrical transport in SWNT arrays in terms of surface coverage, length scaling, and spatial orientation, and briefly discuss the validity of this model.

However, the electronic properties of SWNT arrays are not only determined by geometrical arguments. The contact resistances at the nanotube-nanotube and nanotube-electrode (bulk metal) interfaces, and interactions with the local chemical groups and the underlying substrates are among other issues related to the electronic transport in SWNT arrays. Different aspects of these factors have been studied in detail by many groups. In fact, I have also included a brief discussion about electron injection onto semiconducting SWNTs by polymer dopants. On the other hand, we have compared the substrate-SWNT interactions for isotropic (in two dimensions) arrays of SWNTs grown on Si/SiO_2

substrates and horizontally (on substrate) aligned arrays of SWNTs grown on single crystal quartz substrates. The anisotropic interactions associated with the quartz lattice between quartz and SWNTs that allow near perfect horizontal alignment on substrate along a particular crystallographic direction is examined by Raman spectroscopy, and shown to lead to uniaxial compressive strain in as-grown SWNTs on single crystal quartz. This is the first experimental demonstration of the hard-to-achieve uniaxial compression of SWNTs. Temperature dependence of Raman G-band spectra along the length of individual nanotubes reveals that the compressive strain is non-uniform and can be larger than 1% locally at room temperature. Effects of device fabrication steps on the non-uniform strain are also examined and implications on electrical performance are discussed.

Based on our findings, there are discussions about device performances and designs included in this dissertation. The channel length dependences of device mobilities and on/off ratios are included for SWNT TFTs. Time response of polymer-electrolyte gated SWNT TFTs has been measured to be ~300 Hz, and a proof-of-concept logic inverter has been fabricated by using polymer electrolyte gated SWNT TFTs for macroelectronic applications. Finally, I dedicated a chapter on scalable device designs based on aligned arrays of SWNTs, including a design for SWNT memory devices.

To the memory of

Ilker Diker (1981-1999).

He was a brother to me…

ACKNOWLEDGMENTS

This work would not have been possible without the support of many people. First of all, I would first like to sincerely thank my advisor, Moonsub Shim, for his guidance and support throughout the course of my graduate studies. I am grateful for his patience, open door policy and his dedication to train his graduate students as highly qualified scientists. I am also indebted to Moonsub not only for advising me on my research but also for training me on how to set up and use laboratory equipment. I am proud to be one of his first generation students and I am happy to keep this honor all my life.

I would like to express my gratitude to our collaborators John Rogers and David Cahill. I have collaborated with Prof. Rogers for many years and his clear and simple way of thinking has inspired me all the time.

I am also indebted to Anshu Gaur, Coskun Kocabas, Kwangu Kang, Seong Jun Kang, Daner Abdula, Tony Banks and Scott Maclaren who helped me carry this work forward. Their contributions are very valuable for this thesis.

I would like to thank all of my past and present group friends. Among them, I feel obliged to name Ju Hee Back, Giles Siddons and David Merchin, who gave me a warm welcome to the group. I should also thank Kwan-Wook Kwon for setting a good role model and being a good friend in the lab, and Khoi Nguyen for her smiley face and positive energy.

Most importantly, I want to thank my wife, my parents and close friends for their continuing support. Without their support, I might have chosen the easy way out. I don't

know any words to express my gratitude to my wife for bearing with me and my way of life.

Finally, I would like to thank the Department of Physics, National Science Foundation, and the U.S. Department of Energy for their financial support. This material is based upon work supported by the NSF (Grants No. CCF-0506660, NIRT-0403489 and DMR-0348585). Scanning electron microscopy and atomic force microscopy were carried out in the Center for Microanalysis of Materials, University of Illinois at Urbana−Champaign, which is partially supported by the U.S. Department of Energy under Grant No. DEFG02-91-ER45439.

TABLE OF CONTENTS

CHAPTER 1

CARBON NANOTUBES: BASICS, CHARACTERIZATION AND INTEGRATION INTO ELECTRONIC DEVICES

1.1. Popular Carbon Materials as Contemporary Electronic Materials

Carbon and carbon compounds have lured mankind's interest since the prehistoric times even though carbon composes only ~0.02% of the Earth's crust.[1] Figure 1.1 shows the photograph of a cave painting art, which tells us that people were using carbon materials more than 30,000 years ago.[2]

Figure 1.1: Prehistoric drawings on the walls of Cave Chauvet. Chemical analysis suggests that charcoal was used to draw the animal figures.[2] The source of the photograph is Wikimedia's public files.

In this dissertation, I will discuss the electrical transport in two dimensional arrays of carbon nanotubes, which are quasi-one dimensional molecules composed of only carbon atoms. However, I find it useful to discuss a few prominent allotropes of carbon other than nanotubes, before I move into the details of carbon nanotubes.

Each carbon atom has 4 valence electrons: $2s^2 2p^2$. Since the energy difference between *2p* and *2s* energy levels is smaller than the binding energy of the chemical bonds, the electronic wave functions of these electrons can mix with each other and adjust the occupation of the *2s* and *2p* orbitals.[3] This mixing of atomic orbitals is called sp^n hybridization. In sp^n (n=1,2,3 for carbon) hybridization, the *2s* orbital is hybridized with n *2p* orbitals and (n+1) σ bonds are formed. Hybridization of atomic orbitals allows carbon atoms to form molecules in many possible configurations, and the physical properties of the molecules strongly depend on the type of hybridization.[3] Of the various molecular configurations for solid carbon, diamond and graphite are the most abundant allotropes of carbon.[3]

Diamonds possess physical properties which make them desirable for many industrial applications. In diamond, carbon atoms make very strong covalent bonds with one another and form a three dimensional crystal structure and are tetrahedrally bonded with sp^3 hybridization very similar to silicon and germanium's crystal structures. Besides being mechanically very hard, thermally very conducting and optically transparent, pure diamond crystals are electrically insulating because there are eight valence electrons per primitive cell and the energy bands do not overlap.[4]

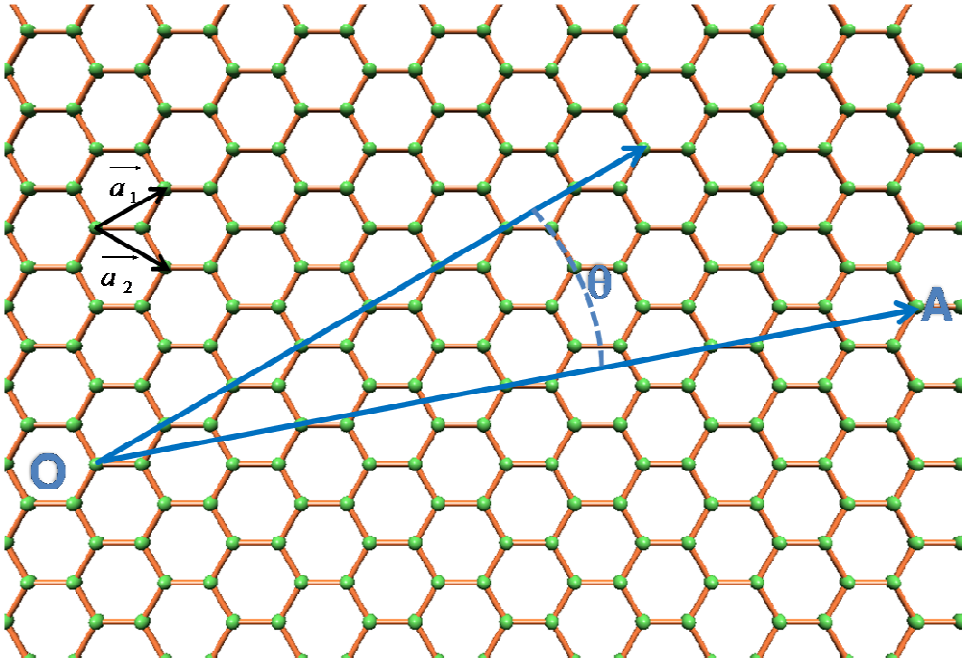

Figure 1.2: A cartoon picture depicting the crystal structure of a graphene layer. Green dots resemble the carbon lattice. $\vec{a}_1$ and $\vec{a}_2$ are the lattice vectors. Carbon nanotubes can be hypothetically considered as graphene layers rolled into hollow cylinders. In that case $\overrightarrow{OA}$ is the chiral vector, which is pointing the overlapping lattice points on the nanotube's surface. The angle, θ, is the chiral angle associated with the chiral vector.

Graphite, on the other hand, is another three dimensional allotrope of carbon with very different physical properties from diamond mostly due to the sp^2 bonding of carbon atoms. Graphite is formed at normal pressures unlike diamond, since it is the thermodynamically stable form of carbon at room temperature and pressure.[3] The crystal structure of graphite looks like a three-dimensional stack of honeycomb looking planar hexagonal carbon lattices. These planes are called graphene layers. The crystal structure of graphene is depicted in Figure 1.2. Graphene layers interact very weakly with one another. Therefore graphite is soft and top layers are easily detached from the underlying layers when it is in mechanical contact with another surface. Thus, graphite is

the popularly chosen material as the lead of pencils. On the other hand, only two of the *2p* electrons are necessary for sp^2 binding, leaving one *2p* electron from each carbon atom to form a delocalized π-bond. The π-bond electrons are delocalized on the graphene layers making each graphene layers very conducting. However, electrical conduction in between planes is very weak. Hence, graphite is not a popular electronic material.

1.2. Graphene and Carbon Nanotubes

Graphene and carbon nanotubes are very similar to graphite in the sense that they all have sp^2 hybridized carbon bonds. The delocalized π-bond electrons make graphene an exceptionally conducting material.[5] The low energy bands in single layer graphene (SLG) have been shown to have a linear dispersion relation as if the charge carriers are massless relativistic fermions, and thus graphene has attracted the interest of many physicists recently.[6] Even though graphene has been studied theoretically for a long time, first experiments on isolated single layers of graphene have been realized very recently.[6,7] As of now, microscopic sized SLG samples can be mechanically exfoliated from highly ordered pyrolytic graphite and macroscopic sized polycrystalline SLG samples can be synthesized by chemical vapor deposition. [6,8] On the other hand, carbon nanotubes (CNTs) and their synthesis methods have been experimentally studied for many years.[3] The crystal structure of carbon nanotubes can be simply described as graphene layers rolled up into tubes. In the earlier days of CNT research, CNTs were synthesized in the form of multiple graphene layers rolled up as a set of concentric cylinders, i.e. multi-walled carbon nanotubes (MWNTs). However, it is also possible to grow single-walled carbon nanotubes (SWNTs), which consist of a single cylindrical

graphene layer. A cartoon image of a SWNT is shown in Figure 1.3. The typical diameters of SWNTs range from 0.4 nm to ~5 nm and the length of the SNWTs range from microns to centimeters, depending on the synthesis methods.[9--11] SWNTs are quasi one-dimensional systems due to the great aspect ratio of length-to-diameter.

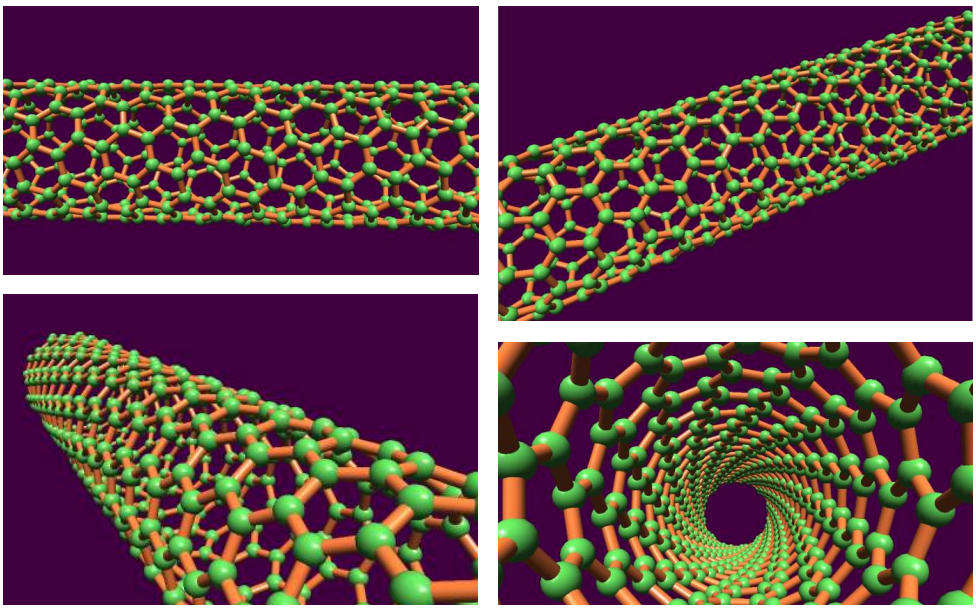

Figure 1.3: A cartoon picture depicting the crystal structure of a (8, 4) single-walled carbon nanotube. Green dots resemble the carbon lattice. The same crystal structure is shown from different angles.

SWNTs form a class of electronic nanomaterials that can be derived by bottom-up chemical synthesis approaches and have very simple atomic composition and molecular configurations.[12] They not only offer the experimental possibility of studying one-dimensional electronics and the strong coupling between structure and electronics in nanoscale systems, but also are high-performance electrical and mechanical materials which could have a big impact on the next generation electronics. Therefore, SWNTs have attracted a well-deserved interest from the scientific and engineering communities over the last two decades.

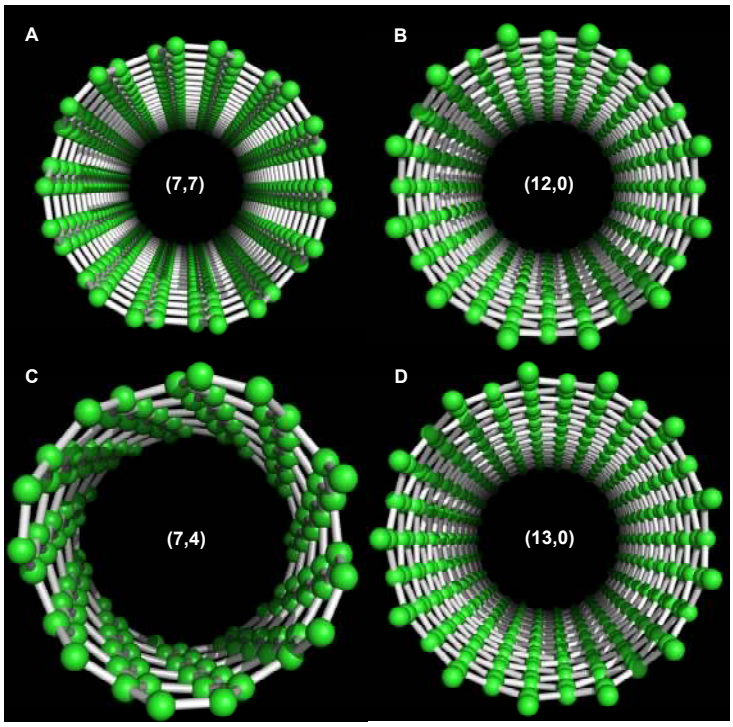

Figure 1.4: Cartoon images exemplify different crystal structures for different (n, m) chiralities. The chiralities are indicated at the center of each image. Green dots resemble the carbon lattice. The longitudinal axes of nanotubes are perpendicular to the plane of the paper. The "CNTbands tool" from the NanoHub site was used to generate the images.[8,9]

SWNTs exhibit both metallic and semiconducting characteristics due to the boundary condition imposed by the closed cylindrical structure. In fact, the electrical characteristics of the SWNTs are mostly determined by the chiral angle shown in Figure 1.2.[3] The chiral vector goes around the circumference of the SWNT. The chiral vector, $\overrightarrow{C_h}$, is usually expressed in the basis of real space unit vectors ($\overrightarrow{a_1}$ and $\overrightarrow{a_2}$) of the hexagonal lattice as $(n,m) \equiv n \cdot \overrightarrow{a_1} + m \cdot \overrightarrow{a_2}$, where *n* and *m* are integers satisfying the inequality $0 \le m \le n$. SWNTs satisfying the condition $(n, m = n)$ are called armchair nanotubes. If m is zero, then the SWNTs are called zigzag nanotubes. All other SWNTs

are called chiral nanotubes. The molecular configurations for each one of these types are exemplified in Figure 1.4.

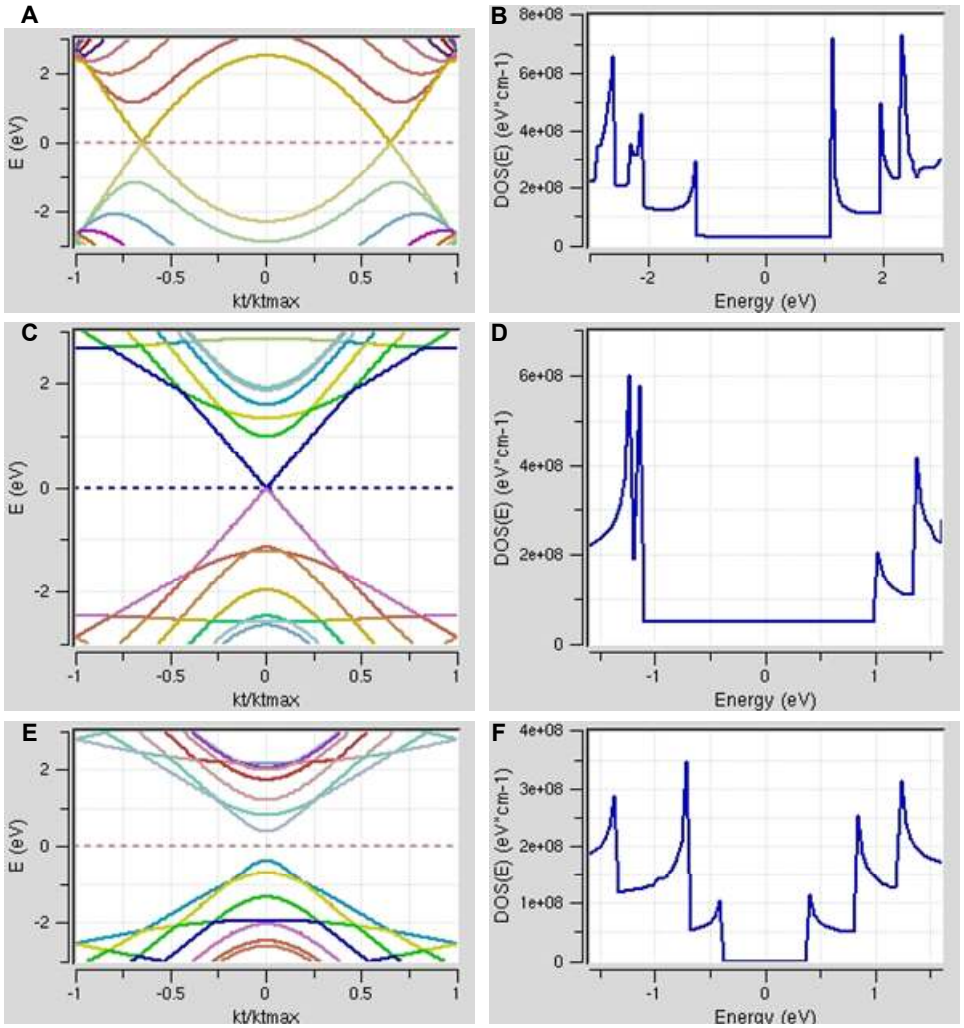

Figure 1.5: Energy dispersion relations for (a) armchair (7, 7), (c) metallic zigzag (12, 0), (e) semiconducting zigzag (13, 0) nanotubes, and (b, d, f) the corresponding density of states are numerically calculated following the extended Huckel theory with the help of the "CNTbands tool" from the NanoHub site.[8,9] The free parameters, tight binding overlap integral and the average carbon-carbon bond length, were set 3.0 eV and 0.142 nm, respectively.

It is well-known that the electrical properties of SWNTs depend strongly on the chirality. Figure 1.5 summarizes tight binding calculations for the electronic band structure of three different SWNTs: armchair (7, 7), zigzag (12, 0), and zigzag (13,

0).[13,14] SWNTs have very diverse electrical characteristics. As seen in the Figure 1.5, the armchair SWNT and the zigzag (12, 0) SWNT have finite density of states around the Fermi level, thus exhibit metallic behavior. On the other hand zigzag (13, 0) SWNT has no allowed electronic states around the Fermi level and the conduction and valence bands do not overlap, hence it exhibits semiconducting behavior. Indeed, whether a SWNT is inherently a semiconductor or a metal can be determined by its chirality. A SWNT is a semiconductor if *(n-m)* is a multiple of three and a metal if otherwise.[3,15]

The electronic band structure of semiconducting SWNTs are qualitatively very similar to one another for low energy bands. However, the bandgap is inversely proportional to the SWNT diameter, $d_t = \frac{\left\|\overrightarrow{C_h}\right\|}{\pi} = \left\|\overrightarrow{a_1}\right\|\sqrt{n^2 + m^2 + nm}$. On the other hand, metallic SWNTs have qualitatively two different types of electronic band structure in the vicinity of the Fermi level. Figure 1.5(a) and (c) demonstrates the qualitative differences, i.e. there is a two-fold band degeneracy at the Fermi level in Figure 1.5(a), but the 4-fold accidental band degeneracy at the Fermi level occurs at the Γ-point ($k = 0$) for the case shown in Figure 1.5(c). However, there are deviations from this model in real nanotubes. The effects of curvature and deformation break the nearest-neighbor bond symmetry, and hence the degeneracy of the bonding and anti-bonding bands except for armchair SWNTs.[16] Therefore, a small bandgap opens in metallic nanotubes with the exception of armchair nanotubes, which are also called true metallic SWNTs. However, these bandgaps are smaller than thermal fluctuations at room temperature for SWNTs, which have diameters greater than 0.6 nm.[16]

Of particular interest are the singularities in the one dimensional density of states, $DOS(E) \propto \frac{1}{\vec{\nabla}_{\vec{k}} E(\vec{k})} \propto \sum_i \frac{1}{\sqrt{E - E_i}}$, corresponding to the extrema in the energy dispersion relations, i.e. $\vec{\nabla}_{\vec{k}} E(\vec{k}) = 0$, or corresponding to the energy at each sub-band threshold (E_i). These are called van Hove singularities, and they do not appear neither in two dimensional graphene nor in the three dimensional graphite. [3,15] Van Hove singularities are observed in Figure 1.5 due to the quasi one-dimensional nature of SWNTs. Besides van Hove singularities, the quasi one-dimensional nature of SWNTs is the reason why low energy excitations are collective in nature rather than being single particle excitations.[17]

1.3. Raman Spectroscopy to Characterize Single-Walled Carbon Nanotubes

Raman scattering is inelastic scattering of light from a sample. Raman spectroscopy of a three-dimensional single molecule is usually a great challenge, because only a very small number of photons scatter inelastically, leading to a very weak Raman signal. However, van Hove singularities observed in one-dimensional molecules allows us to acquire strong Raman signals under certain resonance conditions. Therefore, resonance Raman spectroscopy has been a useful tool to study the vibrational modes of SWNT lattice. Since electrons and phonons are strongly correlated in low-dimensional materials, resonant Raman spectroscopy also provides plentiful information about the electrical properties of SWNTs. Before I explain how Raman spectroscopy is used to characterize SWNTs, I shall discuss the principle of Raman scattering briefly.

In Raman scattering, an electron is excited to a virtual energy level by the incoming photon and then the electron relaxes back to the same electronic state but to a different vibrational state after exchanging energies with a scattered phonon. The photon will either gain (Anti-Stokes process) or lose (Stokes process) energy to the phonon. However, the overall energy of the system is conserved. The energy of the scattered photon is measured experimentally, and the phonon energy is calculated by the energy difference in photon's energy. In a typical Raman spectrum, the intensity of the detected phonon is plotted as a function of the wavenumber (Raman shift), which is the inverse of the wavelength corresponding to the phonon's energy.

In resonance Raman scattering, an electron is excited to a real energy level rather than a virtual level. Once this resonance condition is satisfied, the Raman signal is enhanced by ~3 orders of magnitude. Therefore, one can acquire a strong Raman signal form an individual SWNT if the energy of the incoming or the scattered photon matches with the energy spacing between two van Hove singularities.

Figure 1.6 shows a typical Raman spectrum of an isolated SWNT on a Si/SiO2 substrate collected by a Jobin Yvon HR Raman microscope with a 633 nm He-Ne laser. As seen in Figure 1.6, multiple Raman bands are observed in a single Raman spectrum. In this thesis, the Raman peaks are fit to Lorentzian function unless otherwise is mentioned, and the peak center of each Lorentzian fit is loosely named as the Raman frequency. Actually, Raman shift is proportional to the phonon frequency, but they are different. Below, I summarize some of the important Raman modes.

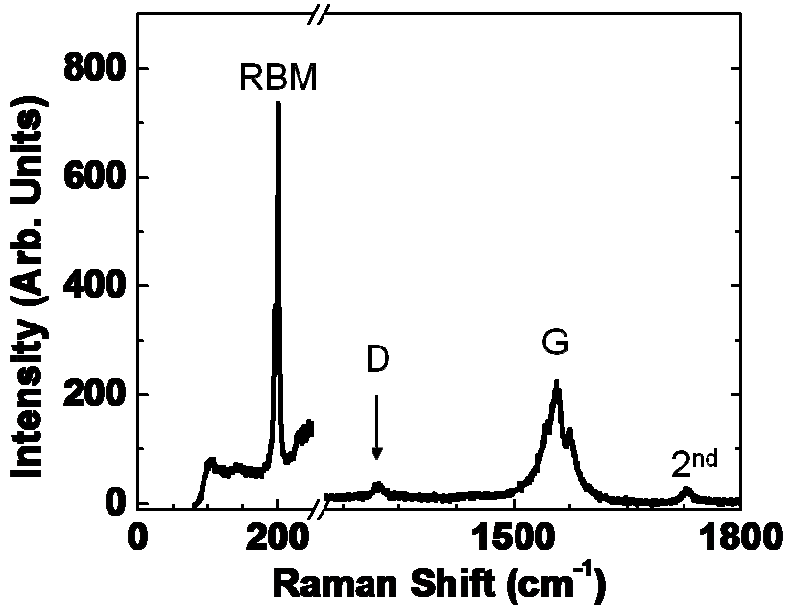

Figure 1.6: A typical Raman spectrum of a single SWNT. The wavelength of the incident laser is 633 nm. Radial breathing (RBM), disorder (D) and tangential (G) modes are indicated.

1.3.1. Radial Breathing Mode

Radial breathing mode (RBM) peaks are typically observed between 100 cm^{-1} and 350 cm^{-1}. The RBM peak frequency has been observed to be almost inversely proportional to the nanotube diameter.[3,15] The diameter dependence of the RBM peak frequency is not surprising since lattice vibrations in the radial direction are closely related to the circumference of the nanotube. More importantly, the RBM frequency can be used to assign the chirality of SWNTs. The revised Kataura plot shown in Figure 1.7 is helpful for assigning the chiral index, as one only observes an RBM signal if the excitonic transition energy is in resonance with either the incident or scattered photon's energy.[18] Each point in Figure 1.7 corresponds to a certain excitonic transition of SWNTs with known chiralities. Once an experimental is value determined for the RBM

frequency, corresponding excitonic transition and the chirality of the SWNT can be determined within the resonance window of the incident and the scattered light.

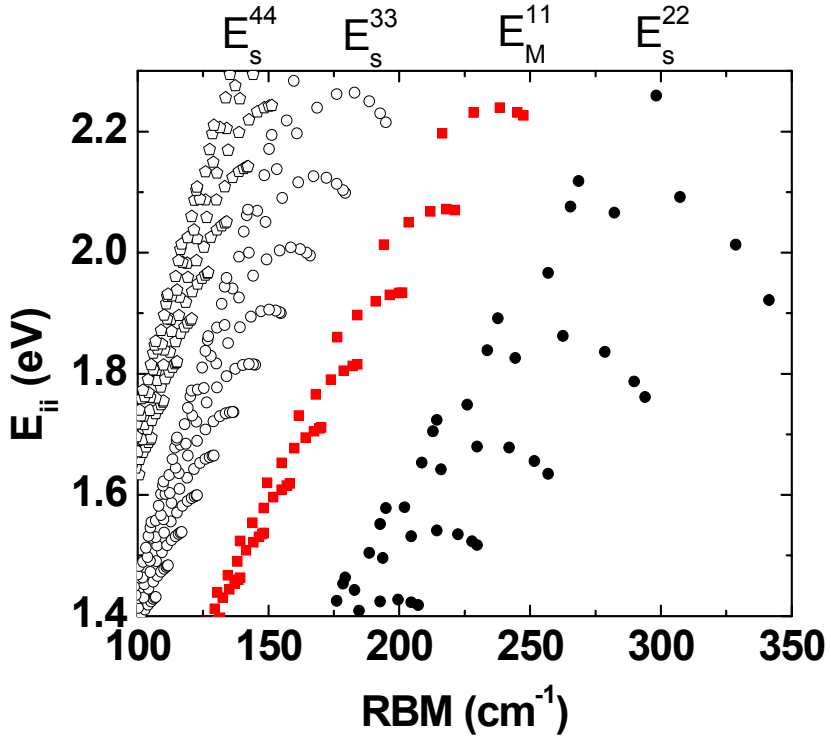

Figure 1.7: A revised Kataura plot. The excitonic transition energy as a function of the RBM frequency is plotted for different optical transitions between different vHs as labeled above the graph.

1.3.2. Tangential Mode (G-band)

Tangential mode (G-band) is associated with the in-plane (tangential for a SWNT) vibrational modes of the graphene with E_{2G} symmetry.[3,19] In SWNTs G-band is composed of multiple peaks due to the Brilloiun zone folding of the graphene and the symmetry-breaking curvature effects.[20] The most intense G-band peak, i.e. G^+ peak is typically centered at ~1590 cm^{-1} at room temperature for undoped SWNTs independent of the laser wavelength. The assignment of G-band peaks differs for metallic and

semiconducting SWNTs. In this dissertation, the G-band Raman characterization will be limited to semiconducting SWNTs. G^+ peak is assigned to longitudinal optical (LO) modes for semiconducting SWNTs.[20] For semiconducting SWNT, G^+ peak frequency is independent of the SWNT diameter.[20] On the other hand, lower frequency G-band peaks are strongly diameter dependent.[20]

G-band frequency is mostly determined by the average carbon-carbon bond length and stiffness. G-band frequency has been observed to depend on chemical and electrostatic doping, mechanical strain and temperature.[19,21--32] For instance, studies on charge transfer into semiconducting SWNTs have suggested that G-band frequency blueshifts (increases) upon doping, since the energy of the Raman active optical phonons is renormalized due to the coupling of phonons to virtual electron-hole pairs.[22] We will revisit the effect of doping on the G-band frequency of semiconducting SWNTs in section 2.7, and describe the diameter dependent charge injection into semiconducting SWNTs. On the other hand, G-band frequency is also expected to shift with lattice distortion in case of a mechanical strain.[29,30,33] For instance, G-band frequency redshifts (blueshifts) with increasing uniaxial strain (compression) in semiconducting SWNTs.[32,34] However, the effect of strain depends on the chiral angle.[31] Similarly, one can also argue that the thermal expansion of the lattice may result in a G-band frequency shift. This argument is not wrong, but it is incomplete. The anharmonic coupling of the optical phonons to the low energy acoustic phonons, as well as a weaker contribution from the thermal expansion of the lattice decrease G-band frequency with increasing temperature.

In summary, G-band peaks provide valuable information about the coupling of the Raman active optical phonons to electrons and phonons, and lattice distortion due to mechanical strain.

1.3.3. Disorder Mode (D-band) & 2D-band

D-band or disorder mode is typically observed between 1200 cm^{-1} and 1400 cm^{-1}. 2D-band or G'-band is typically observed between 2400 cm^{-1} and 2800 cm^{-1}. Unlike G-band, these are double-resonance scatterings, and therefore the frequency depends on the wavelength of the incident laser. D-band scattering involves a single phonon scattering and a defect scattering. For 2D-band, two phonons scatter. In defect-free semiconducting nanotubes, it is very unlikely to observe a D-band Raman signal. However, it is more likely to be observed in metallic SWNTs due to finite electronic density of states near the Fermi level. Therefore D-band Raman signal can be observed in metallic SWNTs.[35--39] Moreover the D-band intensity increases as defects are introduced into the system.[40] Therefore the ratio of the D-band intensity to the G-band intensity is sometimes used as a measure of the change in the structural disorder of SWNTs.[3,39,40] D-band peak frequency, if it is observed, can also be used for determining the shift in Fermi level due to doping.[38]

In summary, strong coupling of electrons and phonons in 1D and the strong dependence of electrical characteristics on the structure, combined with the variety of information that can be gathered by Raman scattering, makes Raman spectroscopy a very powerful characterization method for nanotubes. Therefore, we have frequently used Raman spectroscopy to complement the electrical data we have gathered from SWNTs.

1.4. Single-Walled Carbon Nanotube Field Effect Transistors

The first proof-of-concept SWNT field effect transistor (FET) was reported in 1998 by Delft University researchers.[41] Since then, SWNT FETs have provided experimental evidence for understanding electron transport in one dimension. The applications of SWNT FETs are not limited to addressing scientific problems. SWNT FETs have also been proposed to be the basic element of next generation analog and digital circuit designs based on SWNTs.[42--47]

Within the last decade, FETs have been fabricated on individual SWNTs, sets of a few SWNTs, networks of SWNTs, and aligned arrays of SWNTs.[32,41,48--50] Furthermore, individual SWNTs and SWNT bundles have also been used as interconnects in electronic devices.[51] Recently, applications of SWNT FETs have been extended to more improved analog and digital electronic devices. [42--47] The different approaches to incorporate SWNTs into electronic devices are among the major reasons why there exist huge differences between the reported characteristics for SWNT devices. In this thesis, I will discuss the characteristics of individual SWNTs, SWNT networks and horizontally aligned arrays of SWNTs in FETs. But, I shall first discuss the basics of SWNT FET fabrication.

1.4.1. General Fabrication Techniques and Basics of Operation

FETs are composed of at least three terminals: source, drain and gate. Individual SWNTs or arrays of SWNTs are the active electronic material in the SWNT FETs, i.e. the effective semiconducting channel. The gate terminal controls the electrical conductivity of the semiconducting channel by allowing the application of a transverse

electric field, because the charge carrier population in the conduction band strongly depends on the Fermi level, which can be controlled by this transverse electric field. Source and drain terminals apply a longitudinal electric field in the channel, which is necessary for carrier flow in the channel. The operation of SWNT FETs can be modeled very similarly to the way Si metal-oxide-semiconductor field effect transistors (MOSFETs) are modeled, although the physics of the transportation is not identical. Therefore, the device characterization can be carried out with existing models in the small bias limit.

There are two major steps in SWNT FET fabrication: SWNT growth and microfabrication of terminals. We grow our SWNTs by thermal chemical vapor deposition (CVD). Prior to CVD growth, we pattern the catalyst on the substrate and activate the metal catalyst particles by reducing them in H_2 atmosphere until the furnace reaches the growth temperature, which is typically 900 ^{o}C. The CVD reaction takes place in the presence of a carbon feedstock gas such as ethanol vapor, methane, or ethylene, Ar as a carrier gas and H_2. All gases are required to be of high purity. For SWNT growth, a variety of metal particles have been shown to be effective catalysts for the CVD process. Typically Fe, Ni, Co and Mo catalyst particles are used. During the reaction, supersaturated carbon-bearing molecules are catalytically decomposed on the catalyst surface. Once supersaturation occurs, it has been assumed that graphitic carbon precipitates in the form of nanotubes from the catalyst particle.[52]A recent study shows that any nanoparticle, even Au, Ag, Si and Ge, can act as a catalyst.[53,54] However, Au does not have a catalytic function to produce graphite on bulk crystal surface.[54] A

possible explanation is that the metal nanoparticles form a cluster-like structure so that the carbon atoms are soluble in the cluster, thus the metal particles provide a platform on which carbon atoms can form a hemispherical cap with a graphitic structure and SWNTs grow from the this graphitic seed.[53]However, the CVD growth mechanism of SWNTs is still an unsolved puzzle. SWNTs grow with different yields, orientations, lengths and diameters. These parameters can be controlled by the choice of substrate, catalyst, catalyst density, gas ratio, and growth time. Typical growth times range from 5 minutes to 1 hour. After SWNT growth, the devices are completed by the microfabrication of terminals. Electrodes are patterned by optical lithography and metal (typically Au or Pd with a thin adhesion layer of Ti or Cr) electrodes are deposited by electron beam evaporation. Source and drain electrodes are contacted with the semiconducting channel. Gate terminal is either separated from SWNT channel by a thin layer of insulating oxide or the channel is gated by a polymer electrolyte solution as it will be discussed in detail in the next chapter.

1.5. Scope of the Thesis

In this thesis, I discuss the characteristics of individual SWNTs, SWNT networks, and aligned arrays of SWNTs. We have performed experiments on SWNT materials by complementary Raman spectroscopy and electrical measurements. Chapter 2 discusses polymer electrolyte gating as an exceptional technique for characterization of SWNT FETs. For DC electrical characterization of SWNT FETs, polymer electrolyte gating is discussed to be more effective than gating through oxide dielectrics. Chapter 3 demonstrates how polymer electrolyte gating can be used for channel length-scaling

characterization of SWNT networks, and compares random networks of SWNTs to anisotropic arrays of SWNTs, which are horizontally aligned on quartz substrates. Chapter 4 focuses on our studies on the interaction between horizontally aligned SWNTs and the underlying quartz substrate. Chapter 5 summarizes our studies on the effects of microfabrication on the aligned SWNT arrays. Finally, I offer new device designs based on aligned SWNT arrays for future research in Chapter 6.

1.6. List of References

[1] D. L. Heiserman, *Exploring Chemical Elements and Their Compounds* (Mcgraw-Hill Inc., New York, NY, 1992), p. 376.

[2] J. Clottes, *Chauvet Cave: The Art of Earliest Times* (University of Utah Press, Salt Lake City, Utah, 2003), p.232.

[3] R. Saito, G. Dresselhaus, and M. S. Dresselhaus, *Physical Properties of Carbon Nanotubes* (Imperial College Press, London, 1998), p. 259.

[4] C. Kittel, *Introduction to Solid State Physics* (J. Wiley, New York, 2005), p. 680.

[5] S. V. Morozov, K. S. Novoselov, M. I. Katsnelson, F. Schedin, D. C. Elias, J. A. Jaszczak, and A. K. Geim, Phys. Rev. Lett. **100**, 016602 (2008).

[6] K. S. Novoselov, A. K. Geim, S. V. Morozov, D. Jiang, M. I. Katsnelson, I. V. Grigorieva, S. V. Dubonos, and A. A. Firsov, Nature **438**, 197 (2005).

[7] P. R. Wallace, Phys. Rev. **71**, 622 (1947).

[8] K. S. Kim, Y. Zhao, H. Jang, S. Y. Lee, J. M. Kim, K. S. Kim, J. Ahn, P. Kim, J. Choi, and B. H. Hong, Nature **457**, 706 (2009).

[9] Q. Yang, S. Bai, J. Sauvajol, and J. Bai, Adv. Mater. **15**, 792 (2003).

[10] X. Zhao, Y. Liu, S. Inoue, T. Suzuki, R. O. Jones, and Y. Ando, Phys. Rev. Lett. **92**, 125502 (2004).

[11] L. X. Zheng, M. J. O'Connell, S. K. Doorn*, et al*, Nat. Mater. **3**, 673 (2004).

[12] H. J. Dai, Surf. Sci. **500**, 218 (2002).

[13] D. Kienle, J. I. Cerda, and A. W. Ghosh, J. Appl. Phys. **100**, 043714 (2006).

[14] Youngki Yoon , James K Fodor , Jing Guo , Akira Matsudaira , Diego Kienle , Gengchiau Liang , Gerhard Klimeck , and Mark Lundstrom , *CNTbands*, 2006.

[15] A. Jorio, R. Saito, J. H. Hafner, C. M. Lieber, M. Hunter, T. McClure, G. Dresselhaus, and M. S. Dresselhaus, Phys. Rev. Lett. **86**, 1118 (2001).

[16] A. Kleiner and S. Eggert, Phys. Rev. B **63**, 073408 (2001).

[17] M. Bockrath, D. H. Cobden, J. Lu, A. G. Rinzler, R. E. Smalley, L. Balents, and P. L. McEuen, Nature **397**, 598 (1999).

[18] J. Maultzsch, R. Pomraenke, S. Reich, E. Chang, D. Prezzi, A. Ruini, E. Molinari, M. S. Strano, C. Thomsen, and C. Lienau, Phys. Rev. B **72**, 241402 (2005).

[19] A. M. Rao, P. C. Eklund, S. Bandow, A. Thess, and R. E. Smalley, Nature **388**, 257 (1997).

[20] A. Jorio, A. G. Souza Filho, G. Dresselhaus*, et al*, Phys. Rev. B **65**, 155412 (2002).

[21] M. Shim, T. Ozel, A. Gaur, and C. J. Wang, J. Am. Chem. Soc. **128**, 7522 (2006).

[22] J. C. Tsang, M. Freitag, V. Perebeinos, J. Liu, and P. Avouris, Nature Nanotech. **2**, 725 (2007).

[23] H. D. Li, K. T. Yue, Z. L. Lian*, et al*, Appl. Phys. Lett. **76**, 2053 (2000).

[24] N. R. Raravikar, P. Keblinski, A. M. Rao, M. S. Dresselhaus, L. S. Schadler, and P. M. Ajayan, Phys. Rev. B **66**, 235424 (2002).

[25] Q. Zhang, D. J. Yang, S. G. Wang, S. F. Yoon, and J. Ahn, Smart Mater. Struct. **15**, S1 (2006).

[26] N. Bonini, M. Lazzeri, N. Marzari, and F. Mauri, Phys. Rev. Lett. **99**, 176802 (2007).

[27] Y. Y. Zhang, L. M. Xie, J. Zhang, Z. Y. Wu, and Z. F. Liu, J. Phys. Chem. C **111**, 14031 (2007).

[28] E. D. Minot, Y. Yaish, V. Sazonova, J. Y. Park, M. Brink, and P. L. McEuen, Phys. Rev. Lett. **90**, 156401 (2003).

[29] S. B. Cronin, A. K. Swan, M. S. Unlu, B. B. Goldberg, M. S. Dresselhaus, and M. Tinkham, Phys. Rev. Lett. **93**, 167401 (2004).

[30] S. B. Cronin, A. K. Swan, M. S. Unlu, B. B. Goldberg, M. S. Dresselhaus, and M. Tinkham, Phys. Rev. B **72**, 035425 (2005).

[31] B. Gao, L. Jiang, X. Ling, J. Zhang, and Z. F. Liu, J. Phys. Chem. C **112**, 20123 (2008).

[32] T. Ozel, D. Abdula, E. Hwang, and M. Shim, ACS Nano **3**, 2217 (2009).

[33] A. G. Souza Filho, N. Kobayashi, J. Jiang, A. Gruneis, R. Saito, S. B. Cronin, J. Mendes Filho, G. G. Samsonidze, G. Dresselhaus, and M. S. Dresselhaus, Phys. Rev. Lett. **95**, 217403 (2005).

[34] W. Yang, R. Wang, and H. Yan, Phys. Rev. B **77**, 195440 (2008).

[35] D. Abdula, K. T. Nguyen, and M. Shim, J. Phys. Chem. C **111**, 17755 (2007).

[36] H. Farhat, H. Son, G. G. Samsonidze, S. Reich, M. S. Dresselhaus, and J. Kong, Phys. Rev. Lett. **99**, 145506 (2007).

[37] K. T. Nguyen, A. Gaur, and M. Shim, Phys. Rev. Lett. **98**, 145504 (2007).

[38] M. Shim, A. Gaur, K. T. Nguyen, D. Abdula, and T. Ozel, J. Phys. Chem. C **112**, 13017 (2008).

[39] K. T. Nguyen and M. Shim, J. Am. Chem. Soc. **131**, 7103 (2009).

[40] A. Dillon, P. Parilla, J. Alleman, T. Gennett, K. Jones, and M. Heben, Chem. Phys. Lett. **401**, 522 (2005).

[41] S. J. Tans, A. R. M. Verschueren, and C. Dekker, Nature **393**, 49 (1998).

[42] Z. Chen, J. Appenzeller, Y. Lin, J. Sippel-Oakley, A. G. Rinzler, J. Tang, S. J. Wind, P. M. Solomon, and P. Avouris, Science **311**, 1735 (2006).

[43] M. Shim, Mater. Matters **2**, 16 (2007).

[44] S. Kim, S. Ju, J. H. Back, Y. Xuan, P. D. Ye, M. Shim, D. B. Janes, and S. Mohammadi, Adv. Mater. **21**, 564 (2009).

[45] S. J. Kang, C. Kocabas, T. Ozel, M. Shim, N. Pimparkar, M. A. Alam, S. V. Rotkin, and J. A. Rogers, Nat. Nanotech. **2**, 230 (2007).

[46] Q. Cao, H. S. Kim, N. Pimparkar, J. P. Kulkarni, C. J. Wang, M. Shim, K. Roy, M. A. Alam, and J. A. Rogers, Nature **454**, 495 (2008).

[47] A. Bachtold, P. Hadley, T. Nakanishi, and C. Dekker, Science **294**, 1317 (2001).

[48] E. S. Snow, J. P. Novak, P. M. Campbell, and D. Park, Appl. Phys. Lett. **82**, 2145 (2003).

[49] T. Ozel, A. Gaur, J. A. Rogers, and M. Shim, Nano Lett. **5**, 905 (2005).

[50] C. Kocabas, S. J. Kang, T. Ozel, M. Shim, and J. A. Rogers, J. Phys. Chem. C **111**, 17879 (2007).

[51] P. L. McEuen, M. S. Fuhrer, and H. K. Park, IEEE Trans. Nanotech. **1**, 78 (2002).

[52] Y. Homma, Y. Kobayashi, T. Ogino, D. Takagi, R. Ito, Y. J. Jung, and P. M. Ajayan, J. Phys. Chem. B **107**, 12161 (2003).

[53] D. Takagi, Y. Homma, H. Hibino, S. Suzuki, and Y. Kobayashi, Nano Lett. **6**, 2642 (2006).

[54] D. Takagi, H. Hibino, S. Suzuki, Y. Kobayashi, and Y. Homma, Nano Lett. **7**, 2272 (2007).

CHAPTER 2

CHARACTERIZATION OF CARBON NANOTUBES USING POLYMER ELECTROLYTE GATING

Significant components of this chapter was published as "Polymer Electrolyte Gated Carbon Nanotube Network Transistors", T. Ozel, A. Gaur, J. A. Rogers, and M. Shim, **Nano Letters, 5**, 905 (2005). The subsection 2.7, "*Tuning of Charge Carrier Polarity in Carbon Nanotube Field Effect Transistors under Ambient Conditions"* makes use of arguments and figures published in "Insights on Charge Transfer Doping and Intrinsic Phonon Line Shape of Carbon Nanotubes by Simple Polymer Adsorption", M. Shim, T. Ozel, A. Gaur, and C. Wang, **J. Am. Chem. Soc., 128**, 7522 (2006).

2.1. Introduction

Single-walled carbon nanotubes (SWNTs) have been studied intensively as prototypical 1D systems as well as potential high-performance materials to extend the capabilities of electronic applications.[1] However, reliable characterization methods are essential in interpreting the experimental data for charge transport in SWNTs, and challenges to integrate SWNTs into current micro- and macro-electronics need to be overcome to exploit the exceptional electronic properties of SWNTs in electronic circuits. Difficulties associated with n-channel operation in air, the role of nanotube-metal contacts, highly environment sensitive performance of SWNT devices, inefficient gating of nanotube transistors and large hysteresis in transfer curves are some of the critical issues to be overcome for electronic characterization.[2--4] In SWNT transistors, some of

these issues have been addressed by using top gates with high-κ dielectric materials or ultra-thin gate oxides and choice of contact metal.[5--8]

Here, we propose polymer electrolyte gating as a method for effective electrical characterization of SWNTs and SWNT networks.[9,10] Polymer electrolytes can be used to simultaneously gate the SWNT channels with nearly ideal efficiencies and to control charge carrier type in SWNT transistors. Polymer electrolyte gated transistors are very easy to fabricate and more importantly, polymer electrolyte gating eliminates hysteresis and the short Debye lengths of the electrolyte solution can screen out many external effects (e.g. changes brought on by variations in gas adsorption from the ambient atmosphere) providing a simple yet versatile method of studying electron transport in individual SWNTs and networks of SWNTs.

2.2. Methods

Carbon nanotube field effect transistors were fabricated as described in Chapter 1.3.1. Two distinct types of polymer electrolytes were used as gate materials on top of carbon nanotube field effect transistors, as discussed in our published work.[10] Polymer electrolytes were made by directly dissolving $LiClO_4 \cdot 3H_2O$ in poly(ethylene oxide) (PEO, $M_n = 550$) or in polyethylenimine (PEI, $M_n = 800$) in air at room temperature with 2.4:1 and 1:1 polymer to salt weight ratios, respectively. The chemical structures of the mentioned polymers are shown in Figure 2.1. PEI is an effective electron donor for carbon nanotubes, as discussed later.[2] The electrolytes were injected into a fluidic channel (made from polydimethylsiloxane, PDMS) over the transistor channels for the highly efficient electrolyte gating. The gate voltage was applied through a silver wire,

which was dipped in the electrolyte as shown in Figure 2.1(c). The gate potential induced on the polymer electrolyte was used as a means to form a charge double-layer at the nanotube-electrolyte interface having a very short Debye length. The electric field formed at the electrolyte-nanotube interface was used to tune the carrier density in the channel, and hence the channel conductance.

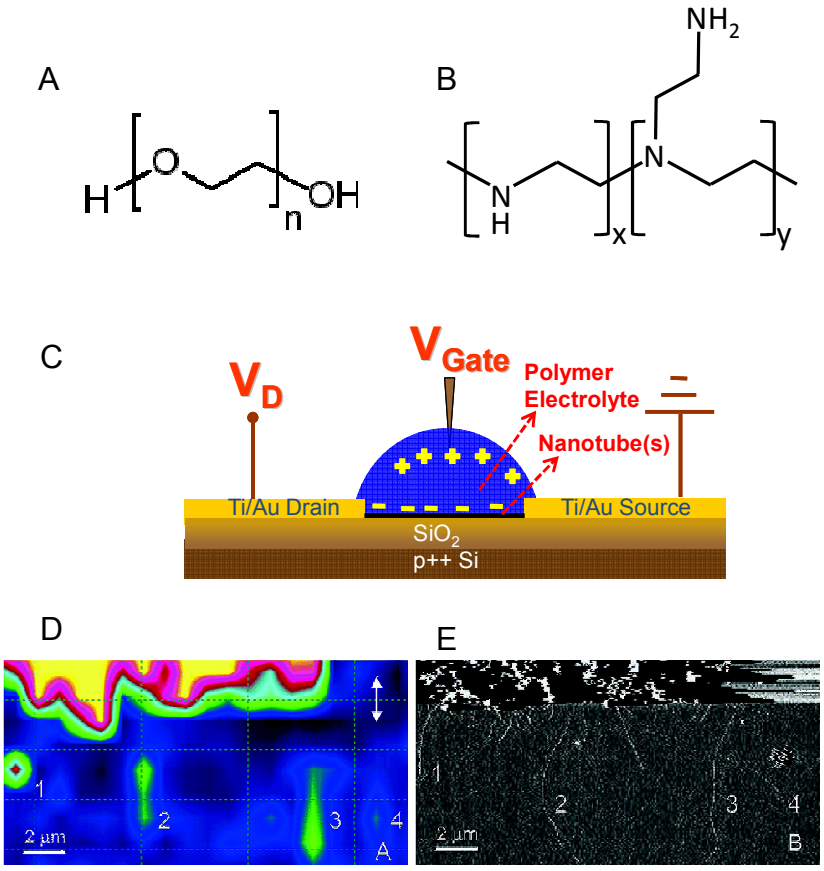

Figure 2.1: (a) PEO Chemical Structure (-CH_2CH_2O-)$_n$ (b) PEI Chemical Structure (-NHCH2CH2-)x[-N(CH2CH2NH2)CH2CH2-]y (c) Schematic Diagram of PEO electrolyte gating of a Carbon Nanotube Field Effect Transistor. (d) Raman map of integrated intensity around the G-band (1575–1610 cm^{-1}). The map is collected using 633 nm (1.96 eV) excitation source at 1 µm scan step. The laser polarization is indicated by the double-headed arrow at the top-right corner. The bright area at the top of the figure is the patterned catalysts which can serve to facilitate alignment and locating SWNTs. The small spot left of SWNT labeled 3 in the Raman map is due to higher background noise. (e) Corresponding atomic force microscope image of the same area. The numbers 1–4 indicate the corresponding SWNTs in Raman map and AFM image.

The Raman measurements were all carried out with a 633 nm laser source with a 100X objective corresponding to a ~1 μm diameter spot size with incident laser power less than 2.5 mW. To characterize the PEI n-doping of carbon nanotubes samples were grown from patterned catalyst islands, which were also used as registration markers. Complimentary topographic AFM images and Raman maps were collected to make sure the same nanotubes were compared before and after PEI doping as shown in Figure 2.1(d).

2.3. Highly Efficient Gating using Polymer Electrolytes

We have successfully demonstrated that polymer electrolytes can be used to gate both individual SWNTs and networks of SWNTs with almost-ideal gating efficiencies. The change in the Fermi level of the SWNT channel equals to $\alpha \cdot eV_{GS}$, where α is the gate efficiency parameter and V_{GS} is the gate potential. In the ideal case α is 1, and α is 0 for no gating. In the early literature, electrical characterization of SWNTs was realized by SWNT FETs which are gated through thick layers of dielectrics (typically 100-500 nm thick silicon dioxide thermally grown on degenerately doped conducting silicon substrates). This type of FET operation is called back-gating in this dissertation. The gate efficiency parameter for back-gating is typically between 1% and 10% depending on the thickness of the dielectric layer. Thicker the dielectric layer leads to smaller the gate efficiency parameter. Therefore, more than 10 Volts is typically required to turn on and off back-gated SWNT FETs. The high voltage operation does not only increase the power consumption, but also causes charges to get trapped either in the oxide or at the oxide

interface. The trapped charges contribute to the channel conductance and hysteresis is observed in the channel conductance as the gate voltage is swept in cycles.

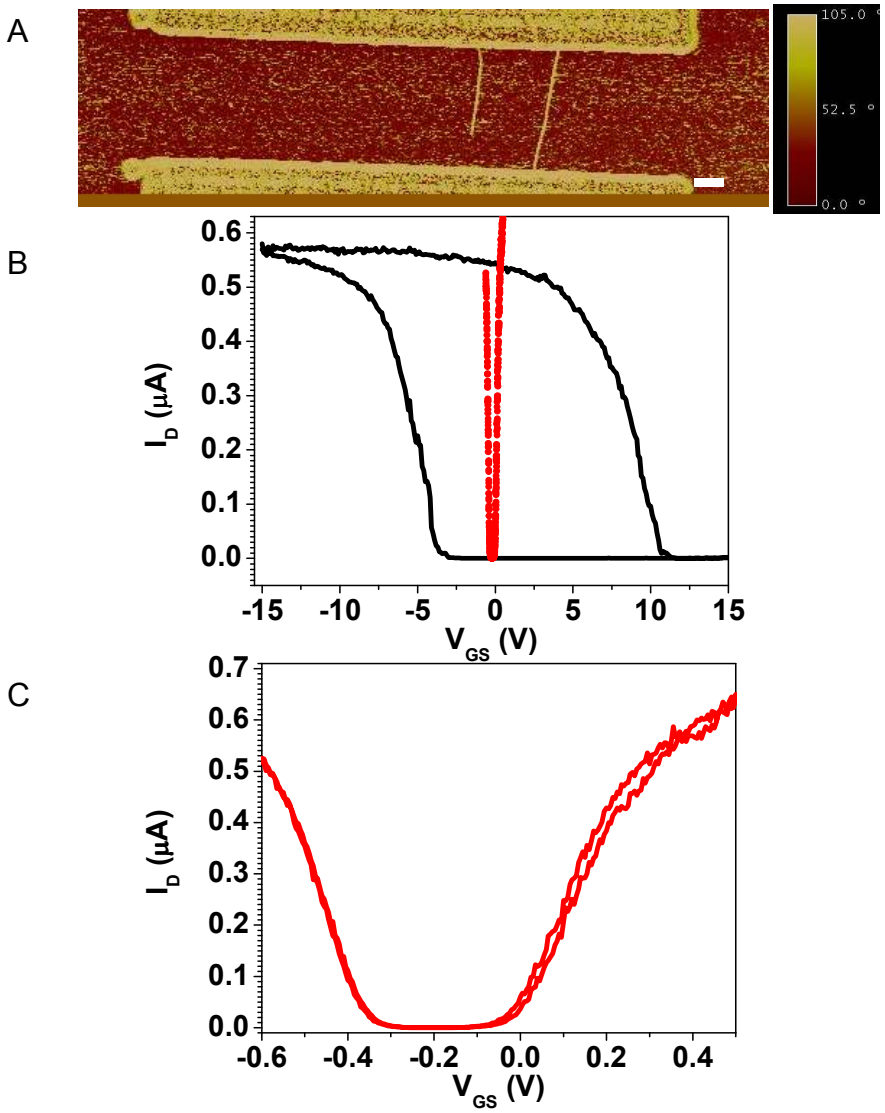

Figure 2.2: (a) AFM image of a single connection device. (b) Transfer curve (drain current vs. the gate potential) for the shown device for both back-gating (black) and polymer electrolyte gating (red). (c) Transfer curve for the polymer electrolyte gating.

A typical SWNT field effect transistor, which has only one SWNT in the channel, is shown in Figure 2.2. The device characteristics of SWNT field effect transistors

operating with PEO based electrolytes are compared to back gate operation in the same figure. The results are consistent for both individual SWNTs and SWNT networks. SWNT networks will be discussed later in the text. The transfer curves of the same single SWNT measured with back gate prior to polymer electrolyte addition (black curve) and with PEO electrolyte gating are plotted together in Figure 2.2(b). The efficiency of the polymer electrolyte gate is high enough that the transistors can operate at an order of magnitude lower gate voltages in comparison to the back-gating efficiency. A very large hysteresis is observed in the back-gated measurement, i.e. the transfer curve (drain current vs. gate potential) is significantly different when the gate voltage is swept in the positive and negative directions. Therefore, interpretation of the electrical measurements becomes challenging. The short Debye lengths of the electrolyte solution can screen out charge trap sites, and hence almost no hysteresis is observed for the PEO electrolyte gated measurement of the same device as shown in Figure 2.2(c).

We estimate the gate efficiency parameter, α, by following Rosenblatt et al.[11] The subthreshold current, i.e. the channel current for gate potentials beyond the threshold voltage, is very small and drops to the noise level abruptly. The linear slope of the subthreshold current in the logarithmic scale with respect to the gate potential, i.e. the subthreshold slope or swing rate, $S = \frac{\partial \log(I_D)}{\partial V_{GS}} \cong \frac{k_B T \ln(10)}{q} \times \frac{1}{\alpha} \approx 60\, mV/dec \times \frac{1}{\alpha}$, can be used to calculate the gate efficiency parameter for any traditional FET. Here, I_D is the channel current, V_{GS} is the gate potential, k_B is the Boltzmann constant, T is the room temperature, and q is the carrier charge. We measure the sub-threshold slope from Figure

2.3 to be 60 mV/dec at room temperature, which corresponds to the ideal gate efficiency, i.e. α=1.

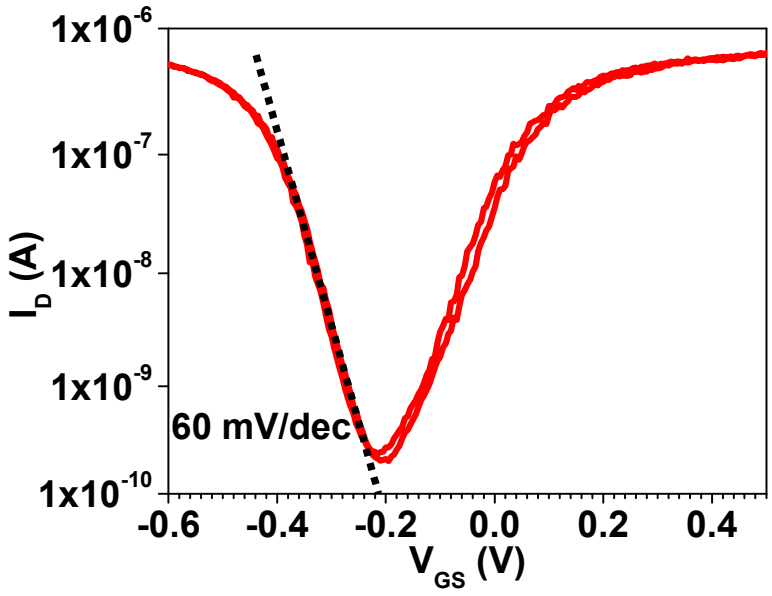

Figure 2.3: Transfer curve for the polymer electrolyte gated device in a semilog plot. Black dotted line shows the sub-threshold slope.

2.4. Realization of Ambipolar Operation

Besides efficient gating, the realization of electron conduction as well as hole conduction is important both for a more complete understanding of the charge transport in SWNTs and for fabrication of complimentary SWNT transistors. Only p-channel operation is observed for the back-gated carbon nanotube transistor shown in the Figure 2.2(b). Indeed this is true for almost all carbon nanotube transistors having electrodes of medium and high work functions (Cr, Ti, Au, Pd) in air.[12] Our earlier work has shown that ambipolar operation under vacuum is realized for Pd contacted SWNT devices with all p-type behavior under O_2 ambient.[13]Ambipolar operation has also been shown for

carbon nanotube transistors contacted with low work function electrodes such as Ca.[12] However, the on conductance for these ambipolar transistors is significantly lower than p-type carbon nanotube transistors. Another approach to maintaining ambipolar behavior is to use high-κ or ultra-thin dielectric layers for gating.[5,6] However, these transistors require sophisticated fabrication methods, and transistors with high-κ gate dielectrics have an intrinsic hysteresis problem due to substrate charge trapping. We have proposed PEO- electrolyte gating as a very easy to apply method to maintain ambipolar operation as well as highly efficient gating, no hysteresis in the transfer curves without loss of high channel conductance.

In Figure 2.2, the n-channel (electron conduction), which does not appear at all for back-gating of the same device through the 300 nm thick SiO_2 insulating layer, is observed to be as conductive as the p-channel (hole conduction) without any hysteresis and the on-current is about the same for both polymer electrolyte gating and back-gating. The output curves, i.e. the channel conductance as function of the channel bias at fixed gate voltages, of the same device for PEO electrolyte gating are displayed in Figure 2.4. Typical FET characteristics are maintained for both p- and n-channels.

Realization of ambipolar operation at room conditions raises the question of whether only n-type operation, which is critical for many device applications, can also be maintained at room conditions using polymer electrolyte-gating. An obvious way to achieve this is to change the work function of the reference electrode and replace the Ag wire with another material as the gate electrode. However, one should be very careful with the choice of this pseudo-reference electrode, since the redox chemistry depends on

the work function of the electrode and the electrode may react with the electrolyte before Fermi level reaches the conduction band. Another easy approach to maintain n-type behavior is to simply select an electron-rich polymer, such as polyethylenimine (PEI), for the electrolyte to chemically alter the Fermi level of the SWNTs at zero gate bias. We will discuss the details of PEI-electrolyte gating later in this chapter.

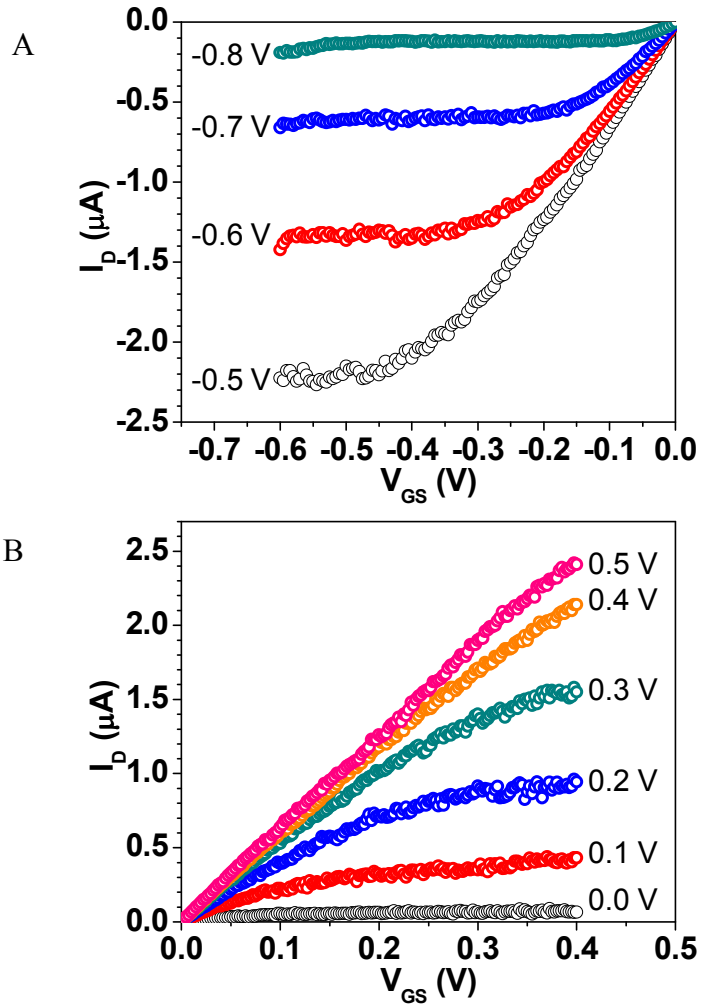

Figure 2.4: Output curves for the polymer electrolyte gated device. Both p- and n-type conductance are observed for the carbon nanotube field-effect transistor.

2.5. Experimental Verification of Inherent Linearity in Carbon Nanotube Field Effect Transistors

2.5.1. Significance of Linear Gain

Intrinsic mobility values higher than those of any known semiconductor have been measured and reported for SWNTs.[14,15] Following the reported high mobility values, the promise of SWNTs for terahertz digital electronic applications is one of the major reasons why SWNTs have been studied so widely by researchers in the field of semiconductors. SWNTs also have promise for radio frequency (RF) analog applications, which are critical in communications technology.[15] In a recent successful attempt to implement carbon nanotubes into RF analog devices, our collaborators have shown that arrays of aligned carbon nanotubes can be used as active circuit elements for detecting radio signals.[16]

RF electronics is widely used for communications technology, which demands compatibility with multiple signal environments. To minimize the interference of multiple signals, the non-linearity of the RF device should be minimized.[15] The schematic diagram of a common-drain amplifier is shown in Figure 2.5. The input signal, V_{in}, is applied to the gate of the field effect transistor and the output signal, V_{out}, is read across the load, which is in series to the transistor. The output signal is proportional to the drain current, I_D, which is a function of both the gate-source bias (the input signal for this particular case) and the drain-source bias, V_{DS}. For a good RF device, the output signal should be a linear function of the input signal. Baumgardner et al. have proposed that carbon nanotube field effect transistors can be inherently linear, once the contacts are

ohmic and the quantum capacitance is less than the electrostatic gate capacitance. However, they were not able verify their hypothesis experimentally because their devices suffered from low electrostatic gate capacitances.[15] We propose that polymer electrolytes offer very high electrostatic gate capacitances, due to very short Debye lengths, and therefore polymer electrolyte gating can be used to experimentally verify that carbon nanotube field effect transistors are inherently linear. In order to examine our experimental findings, the channel conductance and the gate capacitance for carbon nanotube field effect transistors are discussed below.

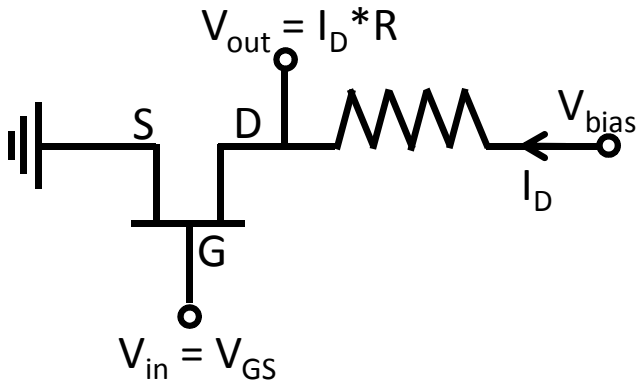

Figure 2.5: Schematic diagram for a proposed read-out circuit for carbon nanotube field effect transistor, a common-drain amplifier.

2.5.2. Landauer-Buttiker Formalism

To calculate the channel conductance, we follow previous theoretical works.[17--19] Assuming contacts to be ohmic so that the device I-V curves obey the Ohm's Law, the electric field in the channel is constant, the transmission coefficient, $T(E)=t$, is constant and the channel conductance is ballistic, the part of the channel current due to electron conductance can be estimated by Fermi statistics, in terms of the chemical

potential (μ) and the energy band-gap (2Δ) of the semiconducting carbon nanotube, the temperature (T), the electron's charge (e), Boltzmann's constant (k), and Planck's constant (h) as follows:

$$i = \frac{4e}{h} t \int_{\Delta}^{\infty} dE f(E-\mu) \cong t \frac{4e}{h} kT \ln\left[1+\exp[(\mu-\Delta)/kT]\right] \qquad \text{Eq. 2.1}$$

The result can be generalized for ambipolar conduction by also considering hole conduction as well as electron conduction. Considering the limit where the quantum capacitance, C_q, is much greater than the electrostatic gate capacitance, C_e, the chemical potential of the carbon nanotube can be estimated as $\mu \approx eV_{GS}$. Under all of the above assumptions, and defining the threshold voltage as $V_T \equiv \Delta / e$, we can estimate the channel conduction as it is stated in the following equation, which is linear for the $e|V_{GS}-V_T| >> kT$ limit:

$$i \approx \frac{4e}{h} kT \left\{ t_e \ln\left[1+\exp[e(V_{GS}-V_{T,e})/kT]\right] + t_h \ln\left[1+\exp[-e(V_{GS}-V_{T,h})/kT]\right] \right\} \qquad \text{Eq. 2.2}$$

The subscripts e and h in the equation correspond to electron and hole conduction.

2.5.3. Gate Capacitance

The physical limit under which all of the above discussions are valid requires the electrostatic gate capacitance to be greater than the quantum capacitance. As a first approximation, the quantum capacitance can be considered as the difficulty of placing an electron into the nanotube, and the quantum capacitance per unit length can thus be

estimated as $C_q = \frac{4e^2}{\pi\hbar v_F} \cong 4\times10^{-10}\, F/m$, when the conduction only upto the first sub-band edge is included.[11] The electrostatic gate capacitance can be simply estimated by using the capacitance of a coaxial cable. For polymer electrolyte gating, the dielectric thickness can be taken as the Debye length of the electrolyte, $\lambda = \left(\frac{2\rho e^2}{\varepsilon\varepsilon_0 kT}\right)^{-1/2}$, where ρ is the concentration of the electrolyte, ε is the dielectric constant and ε_0 is the permittivity of the free space. Therefore, the electrostatic gate capacitance is $C_e = \frac{2\pi\varepsilon\varepsilon_0}{\ln(1+\frac{\lambda}{r})}$, where r is the nanotube radius. For the PEO/$LiClO_4$ electrolyte used in the measurements, the salt concentration is ~2.4 molar and the dielectric constant of the bulk electrolyte is ~10.[9] However, at the nanotube-electrolyte interface the effective dielectric constant is about one half of the bulk value.[20] Therefore, the electrostatic gate capacitance per unit length is calculated to be $4\times10^{-9}\, F/m$, if the diameter of the carbon nanotube is 2 nm. Following these estimates, the quantum capacitance is about one order of magnitude smaller than the electrostatic gate capacitance. Therefore, the large electrostatic gate capacitances achieved by polymer electrolytes can be used to test whether nanotube transistors can be inherently linear or not.

2.5.4. Experimental Verification of Inherent Linearity

The time response of electrolytes upon alternating electrical bias is limited by the slow mobility of the large ions in the electrolyte. Therefore electrolyte gating is not compatible with the demands of the high-speed communication tools. However,

electrolyte gates can be used to test the transport theory at the large electrostatic gate capacitance limit to evaluate the feasibility of further research to develop highly capacitive gate dielectrics for analog RF applications of carbon nanotube transistors. Even though theoretically nanotube transistors are expected to show inherently linear behavior, this inherent linearity has not been verified by experimental studies. Here, we provide the first experimental evidence of inherent linearity of carbon nanotube transistors by polymer electrolyte gating.

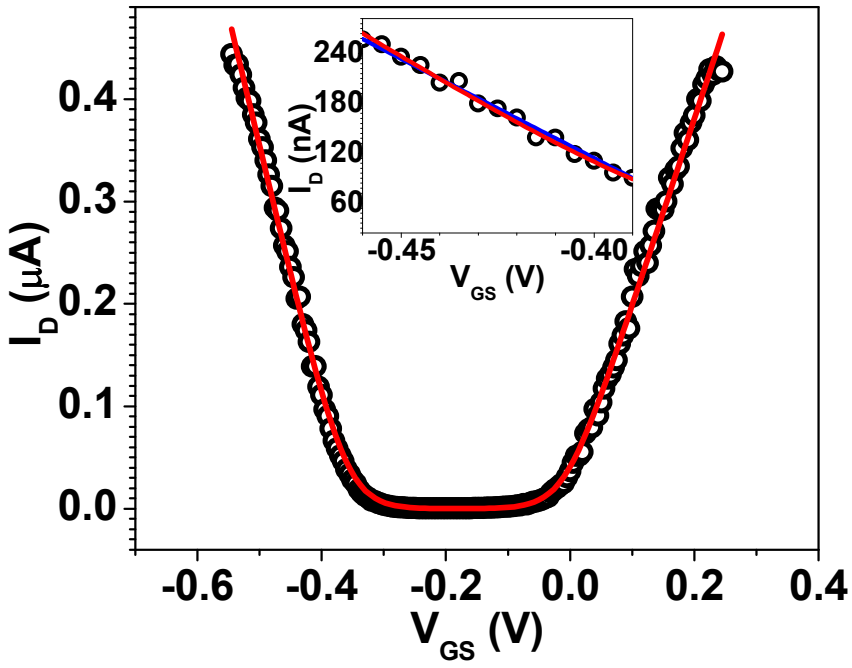

Figure 2.6: Transfer curve for a PEO electrolyte gated carbon nanotube FET with a channel length of 4 microns. The inset shows the same data with a zoomed-in scale. The source-drain bias is 0.1 V.

In Figure 2.6 the transfer curve of a polymer electrolyte gated ambipolar carbon nanotube transistor is shown. The data is fit to the equation 2.2, which is a modified Landauer-Buttiker equation for ambipolar conduction at the limit of large electrostatic

gate capacitance. The data is fit well to the Landauer-Buttiker model for our range of gate capacitances, and both electron and hole conduction shows very good linearity as a function of gate bias away from the threshold voltages as it can also be shown from the equation 2.2.

2.6. Polymer Electrolyte Gating of Carbon Nanotube Networks and Sub-monolayer Thin Film Carbon Nanotube Transistors

We have shown that polymer electrolytes can be used to gate individual carbon nanotubes with almost ideal efficiencies under ambient conditions without any need for sophisticated fabrication techniques. More importantly, polymer electrolyte gating eliminates hysteresis and short Debye lengths of the electrolyte solution opens the possibility for very high gate capacitances and can also screen out many external effects (e.g. changes brought on by variations in gas adsorption from the ambient) providing simple yet versatile method of studying electron transport in networks of prototypical 1D materials. Here, we first demonstrate that polymer electrolyte gating can be successfully applied to two dimensional carbon nanotube random networks.

Carbon nanotube TFTs were fabricated by catalytic chemical vapor deposition (CVD) on Si/SiO_2 substrates as described earlier. Briefly, ferritin (Sigma, diluted 20 times in de-ionized water) was used to deliver catalysts for nanotube synthesis at 900^oC with ultra-high purity CH_4 and H_2. Nanotubes form a random network on the substrate which acts as an effective thin layer of semiconductor. Metal electrodes, Au (30 nm) with Cr (2 nm) adhesion layer, were deposited by electron beam evaporation on patterns defined by UV lithography. Following lift-off, equally spaced stripe patterns of SWNT

networks along the channel length are obtained by second lithography step and O_2 plasma etch. This stripe pattern prevents device-to-device cross-talk as well as the leakage to the silicon back gate. The transistors were gate by polymer electrolytes as discussed earlier. Average nanotube density is about 6 μm^{-2}. The diameters of SWNTs vary between 1 to 3 nm as verified by Raman spectra and AFM imaging.

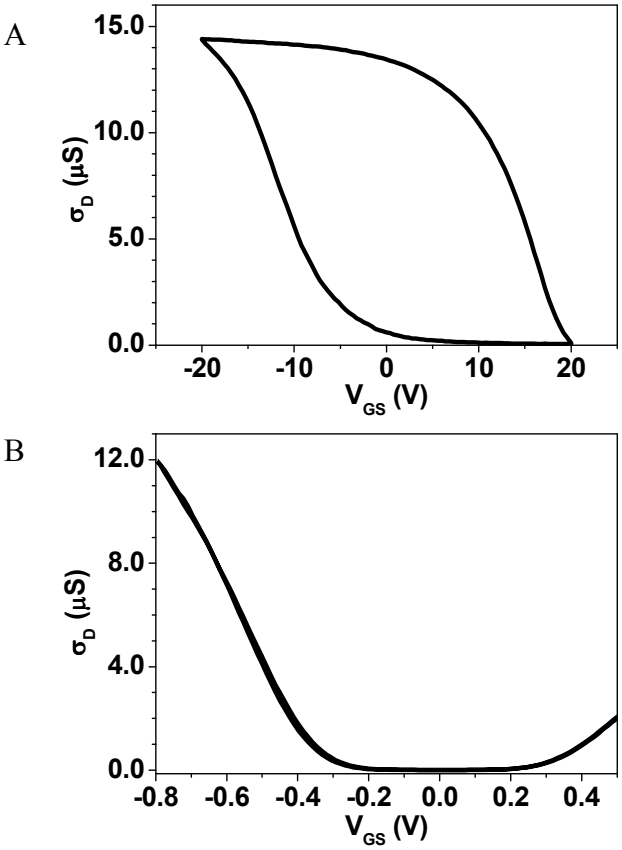

Figure 2.7: (a) Back-gated and (b) PEO electrolyte gated transfer curves for a thin film carbon nanotube transistor with a channel length of 100 microns.

The device characteristics of SWNT network TFTs operating with PEO based electrolyte are compared to back gate operation in Figure 2.7. Consistent with results of individual SWNTs, polymer electrolytes can be successfully employed on networks of SWNTs for highly efficient gating. Figure 2.7(b) shows transfer characteristics of a

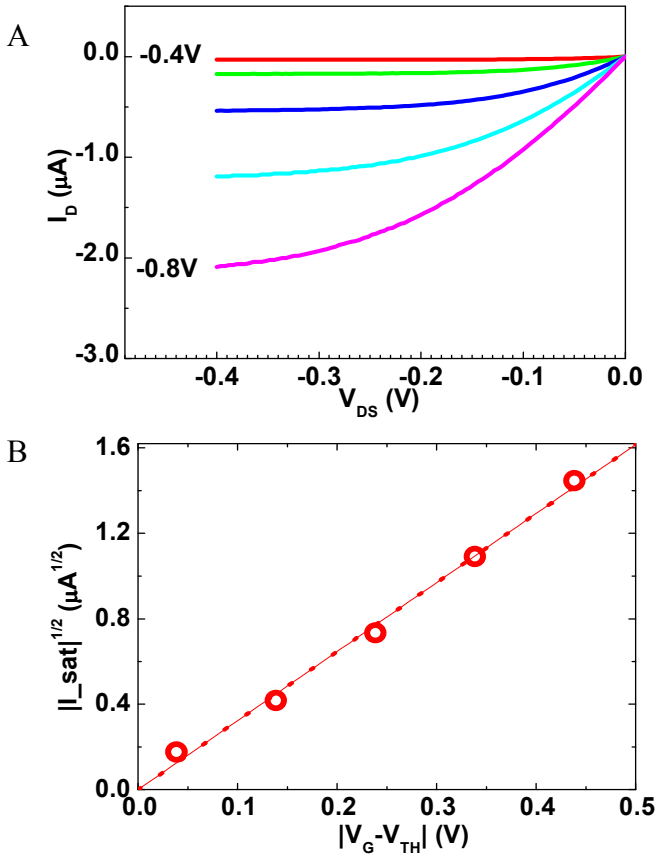

Figure 2.8: (a) Output curve of the thin film carbon nanotube transistor and (b) the scaling of the saturation current with the applied gate potential.

typical device with PEO electrolyte gating. Large hysteresis observed in the back-gate operation is eliminated when the device is gated through the PEO electrolyte. The efficiency of the polymer electrolyte gate is high enough that the transistors can operate at an order of magnitude lower gate voltage range. Following Rosenblatt et al.,[11] we estimate the gate efficiency parameter to be ~0.6 from sub-threshold swing of ~100 mV/decade for 100 μm channel length devices on random networks of SWNTs. This gate efficiency parameter is smaller than that reported for PEO gating of individual SWNT but may be due to small but non-zero residual off currents of ~ 0.25 nA in the network TFTs. The output characteristics for a typical PEO electrolyte gated device are shown in Figure

2.8(a). The saturation current follows square law dependence on gate voltage as shown in Figure 2.8(b) as it does for typical Si MOSFETs.

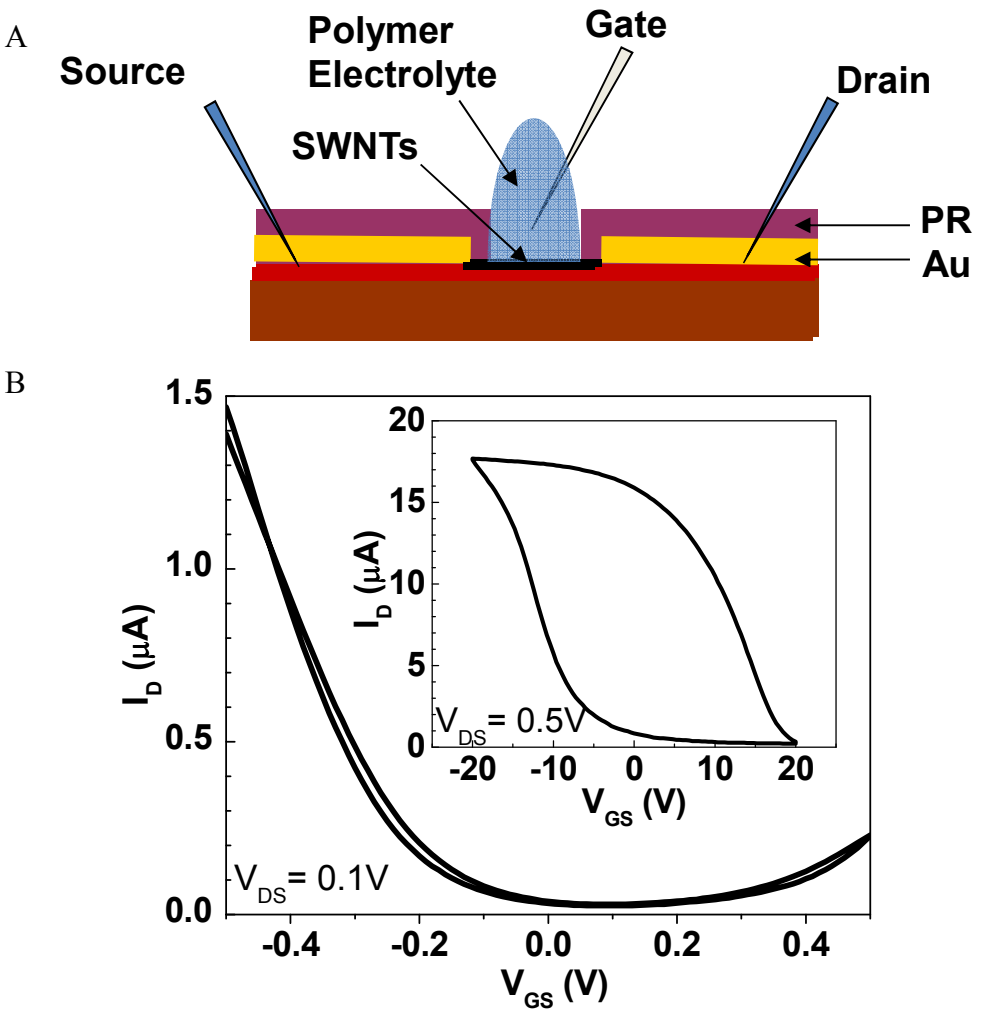

Figure 2.9: (a) Schematics for the test experiment. The contacts and the electrodes are covered by the insulating photoresist. (b) Transfer curve of the PEO electrolyte gated device with covered contacts and the corresponding transfer curve for the back-gated measurement.

Since we are utilizing relatively high concentrations of electrolytes, possible leakage current from ionic conduction through the polymer electrolytes should be examined before further analysis of device characteristics. In order to test ionic

conduction and contact contributions, we have fabricated devices where the electrodes are covered with an insulating photoresist layer by an additional lithography step as shown in Figure 2.9(a). Here, the direct contact between polymer electrolytes and the metal electrodes, which can change the metal work function and allow ionic conduction between drain and source electrodes (i.e. leakage current), is avoided. The inset in Figure 2.9(b) shows the back gate measurements of a SWNT network device with covered electrodes. No significant deviation in the device characteristics is observed after covering the electrodes. Operation of this device with PEO electrolyte is shown in Figure 2.9(b). Similar on and off currents and transconductance are observed with or without covered electrodes. These results suggest negligible contribution from ionic conduction in the measured current.

2.7. Tuning of Charge Carrier Polarity in Carbon Nanotube Field Effect Transistors under Ambient Conditions

Having demonstrated that polymer based electrolytes can be used to gate SWNTs and SWNT networks with almost ideal efficiencies and knowing that the electronic character of SWNT is highly sensitive to the ambient due to all surface atom make-up, we have investigated the possibility of n-doping of SWNTs. The ability to control and tune the doping level of SWNTs is a critical need for electronic applications. Having as-grown nanotubes exhibit only p-type operation in air due to O_2 adsorption on the sidewalls and at the metal contacts have been a limitation on the nanotube applications.[13,21--24] Stable n-type operation in air has been previously accomplished by the choice of contact metal, however it requires H_2 annealing prior to metal

evaporation or poor performance limited by the large Schottky barrier is observed.[12] On the other hand, non-covalent adsorption of amine rich polymer coating offers an easier alternative for n-doping in air. Since the high density of electron-donating amine groups of polyethylenimine (PEI) has been proposed to n-dope nanotubes previously, we have studied PEI to n-dope SWNTs.[2]

We will initially discuss the microscopic nature of the PEI doping by studying the changes in Raman modes upon PEI-doping of individual SWNTs. Later we will show the realization of dominant n-channel operation in carbon nanotube transistors gated by PEI based electrolytes, which will be followed by a brief discussion on proof-of-concept logic circuit applications.

2.7.1. Polythyleneimine Doping of Individual Carbon Nanotubes

A complete picture of charge transport in SWNTs cannot be solely attained by electrical measurements. Electrical characterization may be limited due to complications at the contacts.[13]Thus, non-invasive optical probes, such as resonant Raman spectroscopy, are widely used for more comprehensive characterization of SWNTs.[25,26]

Here, we carry out resonant Raman measurements at the single nanotube level to examine charge transfer doping in SWNTs upon PEI adsorption. Our approach to characterize the PEI doping is to examine isolated individual SWNTs before and after PEI adsorption by micro-Raman measurements.[27] Complimentary AFM and Raman maps have been used to register the isolated SWNTs before and after PEI doping as discussed earlier in the section 2.2.

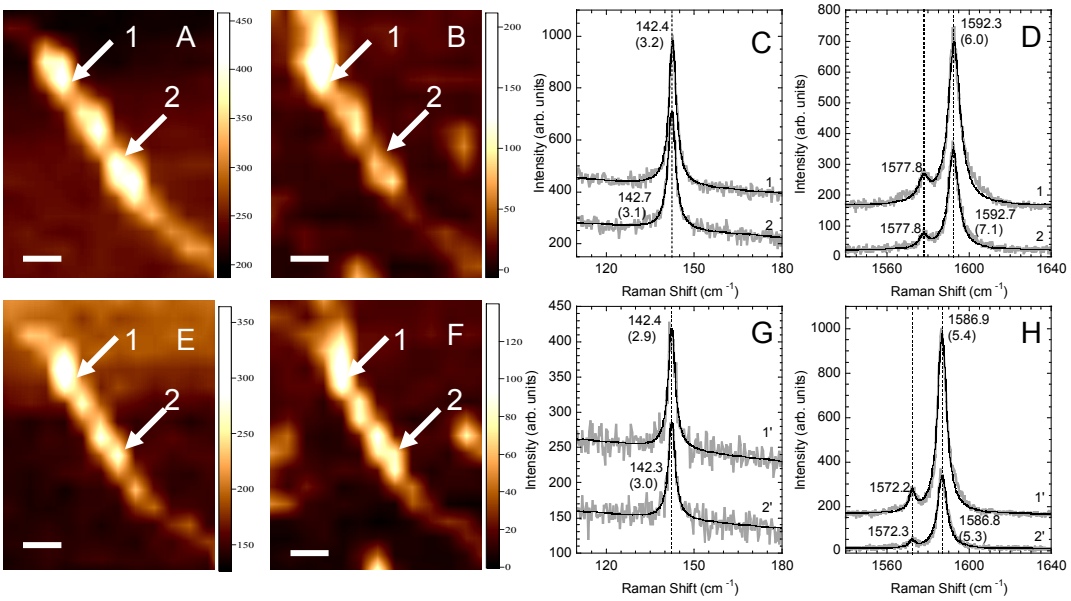

Figure 2.10: Raman maps of the radial breathing mode (a&e) and the G-band (b&f) regions of the same semiconducting single-walled carbon nanotube before (a-b) and after (e-f) n-doping with polyethylenimine. All scale bars are 1 µm. Spectra at the spots indicated by the arrows in the Raman map are shown in (c) and (d) for as-synthesized and (g) and (h) for after polymer adsorption. Grey lines are the data and the black lines are the Lorentzian curve fits. Raman maps are collected with 633 nm (1.96 eV) laser excitation. Spectra are offset for clarity.

The spectra shown in Figure 2.10 are extracted from the indicated points (1 and 2) on the Raman maps. The RBM peaks suggest the SWNT that we study is a semiconducting carbon nanotube with a possible chiral index of (19, 5). For each spectra the peak position and the full width at half maximum (FWHM) are indicated on the graph. No changes are observed in the spectral position and the line width of the RBM along the length of the SWNT or upon PEI adsorption for this SWNT within the instrumental spectral resolution (1 cm^{-1}). RBM frequency may be constant since charge injection is expected to change the in-plane C–C bond lengths but not necessarily the out-of-plane vibrational modes. Unlike the RBM, there is a large shift in the spectral position of the G-band upon PEI adsorption. The most intense peak at higher frequency (G^{+})

downshifts from 1592.3 cm^{-1} to 1586.9 cm^{-1} and the lower frequency peak (G^-) also exhibits very similar downshift of 5.5 cm^{-1} upon PEI doping. The same changes are seen along the full length of the SWNT upon PEI adsorption. This downshift in the G-band is consistent with C–C bond length expansion expected upon electron injection and as observed in alkali metal doping of nanotube and graphite systems.[28--30] The downshift of ~6 cm^{-1} is comparable to the ~8 cm^{-1} shift observed in electrochemical doping with K and Li.[31] As a simple guide, if we assume the same G-band shift ($\Delta\omega_G$) to doping fraction change (ΔQ) ratio $\alpha \equiv \Delta\omega_G/\Delta Q \sim 370$ cm^{-1}/electrons per C atom as reported for alkali metal electrochemical doping, [31] this downshift corresponds to $\Delta Q \sim 0.02$. Considering that the amine groups of PEI are separated by 2 C atoms with mixture of primary, secondary and tertiary amines (i.e. possible differences in electron donating ability) and that the branched structure of the polymer is unlikely to yield close-packed chains, this magnitude of doping fraction change may be expected. However, there is a strong diameter dependence on the G-band shift upon PEI doping.

The diameter (d) dependence of the change in the G-band peak frequencies of semiconducting SWNTs upon PEI adsorption is shown in Figure 2.11. Larger diameter SWNTs show significantly larger downshift upon PEI doping whereas smaller diameter tubes show little or no change. This overall trend in the diameter dependence of the G-band spectral shift can be explained by a diameter dependent activation barrier for thermal ionization of electrons from the donor PEI to the semiconducting SWNTs. The G-band spectral shift shown in Figure 2.11(a) has been fit to this model under the following assumptions. Assuming the carriers injected on the SWNT are solely from PEI

adsorption and the G-band spectral shift due to electron injection is linearly proportional to the doping fraction change following the results from alkali metal electrochemical doping of SWNTs,[31] we relate the G-band spectral shift to $\Delta E \propto d^{-1}$, which is the difference between the donor energy level and the conduction band edge, as $\Delta\omega_G \propto \exp\left(-\frac{\Delta E}{kT}\right)$. The data is fit well to the experimental data supporting the thermal ionization model and giving the phenomenological equation:

$$\Delta\omega_G \approx 60cm^{-1}\exp\left(-0.1eV\cdot nm\frac{d}{kT}\right) \qquad \text{Eq. 2.3}$$

On the other hand, the data in Figure 2.11 does not perfectly match with the equation 2.3. We know that as-grown SWNTs on substrate are often initially p-doped by O_2 and the substrate itself.[32] In that case, we should take into account that SWNTs that we have studied may not be undoped prior to PEI doping. Indeed, PEI doping should reverse the effect of O_2 doping before n-doping the SWNT. Depending on where Fermi level lies prior to PEI doping, the G-band frequency may either increase or decrease initially.[33,34] This hypothesis explains the fluctuations in the plotted data in Figure 2.11.

Figure 2.11(b) shows that the line width change upon PEI doping is independent of diameter. There is no significant broadening suggesting that PEI adsorption does not cause changes in the extrinsic (e.g. additional scattering sites due to polymer-nanotube interaction, mechanical deformation, etc.) and intrinsic (e.g. perturbation to the electronic wave functions, Raman resonance conditions, etc.) properties that contribute to the

observed line widths of semiconducting SWNTs. These results can be further tested by electrical measurements as we will discuss in the following section. Comparison of device mobilities prior and after PEI adsorption will help us determine whether our spectroscopic results are supported by electrical measurements.[35]

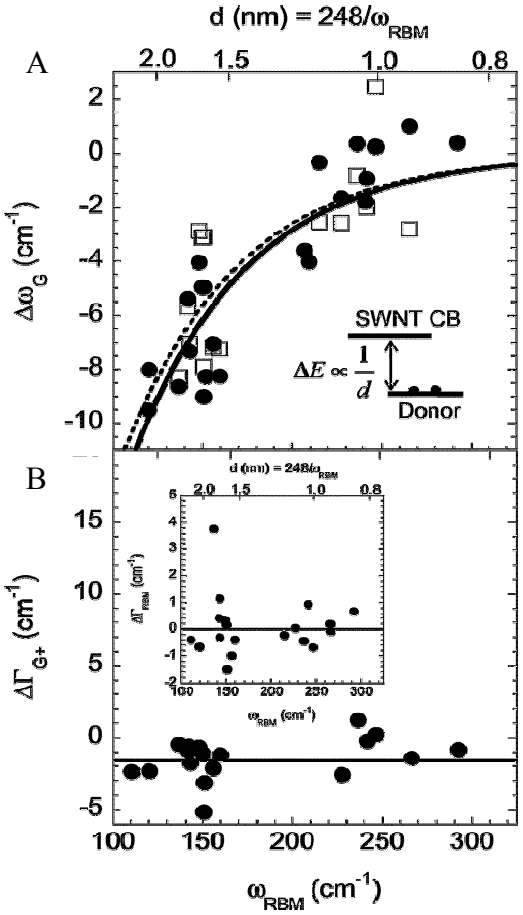

Figure 2.11: (a) Diameter dependence of the spectral shift of the G-band peaks, G^+ (filled circles) and G^- (open squares), upon n-doping with polyethylenimine. The curves are least-squares fits for carrier thermal ionization process as described in the text. Solid (dashed) line corresponds to fit to G^+ (G^-) peak shift. Lower inset is a schematic energy level diagram. Upper inset is the temperature dependence of the G+ peak shift for a 1.75 nm diameter SWNT doped with polyethylenimine at different temperatures. The solid line is a least-squares fit as discussed in the text. (b) Line width (full width at half-maximum) change of radial breathing mode ($\Delta\Gamma_{RBM}$) and the main feature in the G band ($\Delta\Gamma_{G+}$) for different diameter SWNTs upon doping with PEI. On average, the radial breathing mode (inset) shows no change and the G-band shows very slight line narrowing.

2.7.2. Polyethyleneimine Electrolyte Gating of Carbon Nanotubes and n-Type Field Effect Carbon Nanotube Transistors

Having shown PEI effectively injects electrons into SWNTs and the polymer based electrolytes can be used to electrochemically gate the carbon nanotube transistors with high efficiencies, we will now discuss the n-type field effect carbon nanotube transistors realized by PEI based electrolytes.

Figure 2.12 shows electrical measurements on the same random network device with back-gate (inset), PEO electrolyte gate (blue) and finally PEI electrolyte gate (red). The PEI absorption on the SWNT n-dopes the SWNT and the Fermi level is shifted even with zero gate bias. Therefore the threshold voltages for PEI electrolyte gated devices are shifted in the negative direction and the devices show dominantly n-type behavior within the gate bias range. The similarity of the n-channel conductance to the p-channel conductance prior to PEI adsorption supports our results for the Raman measurements that the PEI adsorption does not introduce any additional scattering sites that would degrade the mobility of SWNTs and SWNT networks. The channel length scaling of mobility for both p- and n-conduction is described in Chapter 3.

Careful readers may have noticed that the device shown in Figure 2.12 is the same as the device shown in Figure 2.10. For this device we have deliberately covered the source and drain electrodes by a layer of photoresist so that the electrolyte is isolated from the electrodes as discussed earlier. This extra step is not necessary for n-type operation. However it rules out the possibility of any changes in the work function of the source and drain contacts due to PEI adsorption supporting our hypothesis that the n-type

operation in the PEI electrolyte-gated devices can be solely realized by simple PEI adsorption.

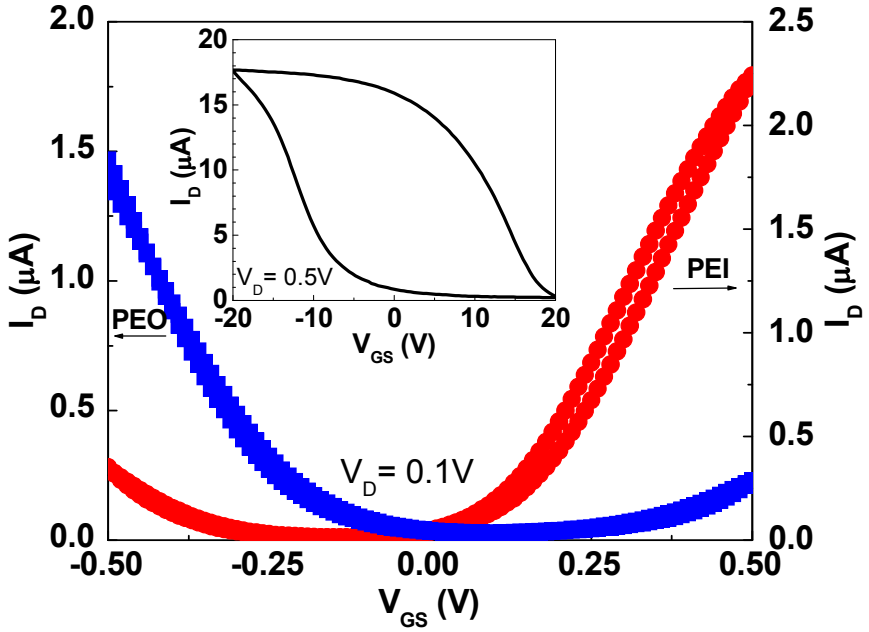

Figure 2.12: Transfer curves of a carbon nanotube thin film transistor with covered contacts as it is gated by PEO- and PEI-electrolytes. The corresponding transfer curve for the back-gated measurement is shown in the inset. 100 mV of source-drain bias is applied for the polymer electrolyte gated measurements whereas the source-drain bias is 500 mV for the back-gated measurement.

2.7.3. A Simple Route to Carbon Nanotube Logic Circuits

Easy fabrication, good device-to-device uniformity, and predictable performance combined with the ability to achieve both p- and n-channel operation make polymer electrolyte gated SWNT TFTS useful for complementary circuit designs in large-area low-cost electronics. As an example, we demonstrate an inverter in Figure 2.13, which takes advantage of PEO and PEI electrolyte-gated SWNT TFTs as p- and n-type field effect transistors (schematic shown in Figure 2.13(a)). Inverter is indeed a NOT gate in

digital logic, and it is the most basic logic gate element in digital electronics. The inset in Figure 2.13(b) shows the gate dependence of drain current of p- and n-devices operating

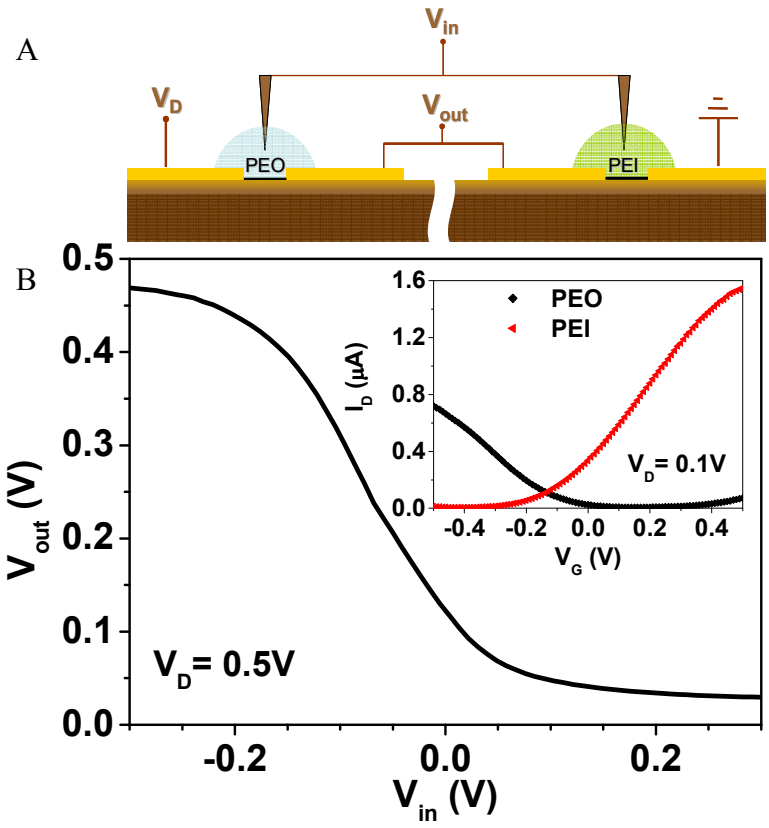

Figure 2.13: (a) Schematics of the proposed inverter logic gate. (b) Voltage transfer curve for the inverter. Inset shows the transfer curves of the two p- and n- carbon nanotube field-effect transistors used in the inverter.

separately. The voltage transfer curve for our proof-of-concept SWNT network inverter is shown in Figure 2.13(b). In an ideal inverter, this curve should be a step function. However, for real devices the slope of the transition between the on and off states is expected to be greater than 1. This slope, also called as the gain, is the device parameter that determines the quality of the inverter. From our voltage transfer curve we estimate the gain of the inverter to be ~1.8 proving the possibility that electrolytes based on dopant

polymers can be used to realize complimentary logic circuits form carbon nanotubes and networks of carbon nanotubes.

2.8. Time Response of Polymer Electrolyte Gating

We have shown several advantages in polymer electrolyte gating of carbon nanotube field effect transistors: 1) high gate efficiencies, 2) lack of hysteresis, 3) the ability to achieve both p- and n-channel conduction simply by choice of polymer material, and 4) facile application in complementary circuits. However, one obvious drawback of polymer electrolyte gating is the switching speed limited by ionic mobility of the gate medium rather than the carrier mobility of the semiconductor material. To estimate the upper limit of the switching speed, we have examined the time response of SWNT network TFTs. Figure 2.14 shows the response of a 100 μm channel PEO-gated TFT. The responses are measured by applying square-wave gate pulses with amplitude separation of 0 and -0.6 V at varying frequencies. As shown in the transfer characteristics in Figure 2.14(a), the device is on at -0.6 V and off at 0 V. Figure 2.14(b) and (c) show the response of the drain current as the TFT is switched on and off at frequencies of 10 Hz and 100 Hz, respectively. The difference in the magnitude of the separation between on and off currents decreases as the switching frequency increases. To quantify switching speed, we introduce the parameter $\eta = \frac{I_{on} - I_{off}}{I_{on} + I_{off}}$. η is 1 when the device can be completely turned off and 0 when the device cannot be turned off at all. This parameter η is plotted as a function of gate voltage pulse frequency in Figure 2.14(d). We define the cut-off frequency as the frequency where η drops to 1/e. The cut-

off frequency of the device shown in Figure 2.14 is 325 Hz which is surprisingly fast. This switching speed should be close to the upper limit for PEO/$LiClO_4$ system since we are using low molecular weight polymer which is liquid at room temperature (i.e. conditions similar to that for the highest achievable ionic mobility for this electrolyte system). We note that the definition of the cut-off frequency may be different depending on the application needs. However, the device can be completely switched off even at 50 Hz.

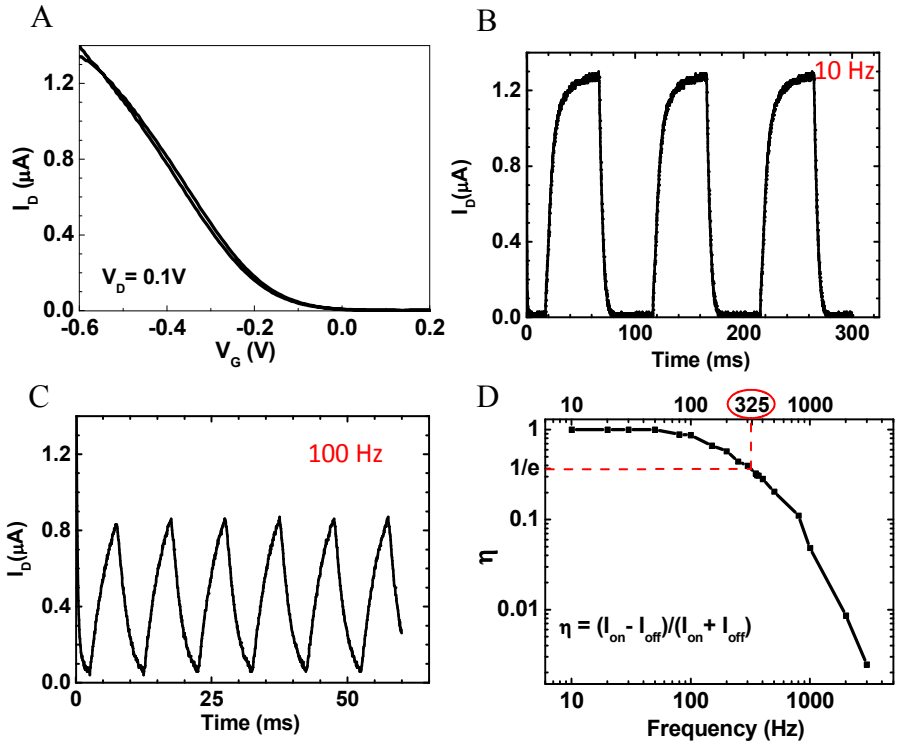

Figure 2.14: Frequency measurements on PEO electrolyte gated SWNT TFT. (a) Transfer characteristics. (b) and (c) are the drain current response to square wave pulse gate voltage for 10Hz and 100Hz, respectively. (d) The parameter η at different frequencies for the device with transfer characteristics shown in (a). A square wave pulse (-0.6V, 0V) is applied to PEO electrolyte gate.

Even though we have proposed polymer electrolyte gating only as a tool for DC characterization of SWNTs, at least low frequency applications (~100 Hz) appear within

reach with polymer electrolyte gated SWNTs. Current improvements in similar but improved polymer electrolyte systems, i.e. ionic gels, suggest polymer electrolyte-gated SWNT transistors can be driven at significantly higher switching speeds (~10 kHz).[36]

2.9. Conclusions

We have shown that carbon nanotube transistors can be efficiently gated by polymer electrolytes. We have demonstrated that PEI is an efficient n-doping polymer for SWNTs, and it can be used in polymer electrolytes without introducing any additional scattering sites and allowing highly efficient n-channel operation. The ability to control the mode of operation from p- to n-type demonstrates the versatility of polymer electrolytes beyond efficient gate media. We have also shown that polymer electrolyte gating can be applied on random networks of SWNTs as well as individual SWNTs. The almost ideal gating efficiencies, lack of hysteresis, ability to control the mode of operation from p- to n-type positions polymer electrolyte gating as a very powerful but still very easy to apply method for electrical characterization of SWNTs and SWNT networks. By using polymer electrolyte gating as a characterization tool, we have experimentally shown that SWNT transistors are inherently linear and can be made use of in analog RF applications. We have also offered polymer electrolyte gating to characterize the SWNT networks, and further length scale analysis of SWNT networks will be discussed in the following chapter. The simplicity with which complementary circuits can be fabricated by exploiting polymer electrolytes has been demonstrated with a proof-of-concept logic circuit. Switching speed of ~300 Hz has also been measured for

PEO electrolyte gated SWNT network TFTs giving an estimate of the upper limit for AC operation of these devices.

2.10. List of References

[1] M. Shim, Mater. Matters **2**, 16 (2007).

[2] M. Shim, A. Javey, N. W. S. Kam, and H. J. Dai, J. Am. Chem. Soc. **123**, 11512 (2001).

[3] W. Kim, A. Javey, O. Vermesh, Q. Wang, Y. Li, and H. Dai, Nano Lett. **3**, 193 (2003).

[4] E. S. Snow, J. P. Novak, P. M. Campbell, and D. Park, Appl. Phys. Lett. **82**, 2145 (2003).

[5] V. Derycke, R. Martel, J. Appenzeller, and P. Avouris, Nano Lett. **1**, 453 (2001).

[6] A. Javey, H. Kim, M. Brink, Q. Wang, A. Ural, J. Guo, P. McIntyre, P. McEuen, M. Lundstrom, and H. J. Dai, Nat. Mater. **1**, 241 (2002).

[7] A. Javey, J. Guo, Q. Wang, M. Lundstrom, and H. J. Dai, Nature **424**, 654 (2003).

[8] Y. Yaish, J. -. Park, S. Rosenblatt, V. Sazonova, M. Brink, and P. L. McEuen, Phys. Rev. Lett. **92**, 046401 (2004).

[9] G. P. Siddons, D. Merchin, J. H. Back, J. K. Jeong, and M. Shim, Nano Lett. **4**, 927 (2004).

[10] T. Ozel, A. Gaur, J. A. Rogers, and M. Shim, Nano Lett. **5**, 905 (2005).

[11] S. Rosenblatt, Y. Yaish, J. Park, J. Gore, V. Sazonova, and P. L. McEuen, Nano Lett. **2**, 869 (2002).

[12] Y. Nosho, Y. Ohno, S. Kishimoto, and T. Mizutani, Appl. Phys. Lett. **86**, 073105 (2005).

[13] M. Shim, J. H. Back, T. Ozel, and K. W. Kwon, Phys. Rev. B **71**, 205411 (2005).

[14] T. Durkop, S. A. Getty, E. Cobas, and M. S. Fuhrer, Nano Lett. **4**, 35 (2004).

[15] J. E. Baumgardner, A. A. Pesetski, J. M. Murduck, J. X. Przybysz, J. D. Adam, and H. Zhang, Appl. Phys. Lett. **91**, 052107 (2007).

[16] C. Kocabas, H. S. Kim, T. Banks, J. A. Rogers, A. A. Pesetski, J. E. Baumgardner, S. V. Krishnaswamy, and H. Zhang, Proc. Natl. Acad. Sci. U.S.A. **105**, 1405 (2008).

[17] R. Landauer, Philosophical Magazine **21**, 863 (1970).

[18] M. Buttiker, Phys. Rev. Lett. **57**, 1761 (1986).

[19] Y. Chen and M. S. Fuhrer, Phys. Rev. Lett. **95**, 236803 (2005).

[20] A. Abrashkin, D. Andelman, and H. Orland, Phys. Rev. Lett. **99**, 077801 (2007).

[21] P. G. Collins, K. Bradley, M. Ishigami, and A. Zettl, Science **287**, 1801 (2000).

[22] G. Dukovic, B. E. White, Z. Zhou, F. Wang, S. Jockusch, M. L. Steigerwald, T. F. Heinz, R. A. Friesner, N. J. Turro, and L. E. Brus, J. Am. Chem. Soc. **126**, 15269 (2004).

[23] S. Heinze, J. Tersoff, R. Martel, V. Derycke, J. Appenzeller, and P. Avouris, Phys. Rev. Lett. **89**, 106801 (2002).

[24] J. Park and P. L. McEuen, Appl. Phys. Lett. **79**, 1363 (2001).

[25] R. Saito, G. Dresselhaus, and M. S. Dresselhaus, *Physical Properties of Carbon Nanotubes* (Imperial College Press, London, 1998), p. 259.

[26] T. Ozel, D. Abdula, E. Hwang, and M. Shim, ACS Nano **3**, 2217 (2009).

[27] M. Shim, T. Ozel, A. Gaur, and C. J. Wang, J. Am. Chem. Soc. **128**, 7522 (2006).

[28] P. C. Eklund, G. Dresselhaus, M. S. Dresselhaus, and J. E. Fischer, Phys. Rev. B **16**, 3330 (1977).

[29] M. S. Dresselhaus and G. Dresselhaus, Adv. Phys. **30**, 139 (1981).

[30] G. Chen, C. A. Furtado, S. Bandow, S. Iijima, and P. C. Eklund, Phys. Rev. B **71**, 045408 (2005).

[31] A. Claye, S. Rahman, J. E. Fischer, A. Sirenko, G. U. Sumanasekera, and P. C. Eklund, Chem. Phys. Lett. **333**, 16 (2001).

[32] A. Gaur and M. Shim, Phys. Rev. B **78**, 125422 (2008).

[33] J. C. Tsang, M. Freitag, V. Perebeinos, J. Liu, and P. Avouris, Nat. Nanotech. **2**, 725 (2007).

[34] K. T. Nguyen and M. Shim, J. Am. Chem. Soc. **131**, 7103 (2009).

[35] T. Ozel, A. Gaur, J. A. Rogers, and M. Shim, Nano Lett. **5**, 905 (2005).

[36] M. J. Panzer and C. D. Frisbie, J. Am. Chem. Soc. **129**, 6599 (2007).

CHAPTER 3

CARBON NANOTUBE NETWORKS AND SUB-MONOLAYER THIN FILM TRANSISTORS

Significant components of this chapter was published as "Polymer Electrolyte Gated Carbon Nanotube Network Transistors", T. Ozel, A. Gaur, J. A. Rogers, and M. Shim, **Nano Letters, 5**, 905 (2005).

3.1. Introduction

Single-walled carbon nanotubes (SWNTs) have been studied as a prominent class of high performance electronic materials for next generation electronics.[1] Their geometry dependent electronic structure, ballistic transport and low power dissipation due to quasi one dimensional transport, and their capability of carrying high current densities are some of the main reasons for the optimistic expectations on SWNTs.[2--6] Proof-of-concept devices such as field effect transistors (FETs), logic circuits, and sensors have already been made.[7--11] Recent advances in optical studies are pushing the limits of SWNTs even further.[12--14] However, device applications of individual SWNTs have been hindered by uncontrolled variations in characteristics.[1] The device-to-device performance deviations arise from a distribution of diameter and chirality, variations at the metal contacts, and interactions with the substrate and the surrounding environment.[1,3,15--21] One relatively new direction in SWNT electronics, which

avoids some of these issues, is using networks of SWNTs where the ensemble average may provide uniformity from device to device.[22--24]

I have discussed earlier in the previous chapter that polymer electrolyte gating is a very powerful yet a very easy to apply technique to characterize carbon nanotubes. In this chapter, I discuss the channel length scaling in thin film transistors (TFTs) fabricated with networks of carbon nanotubes in order to elucidate the effects of channel length and spatial anisotropy on the network behavior of SWNT arrays.

3.2. Methods

Carbon nanotube networks were grown by catalytic chemical vapor deposition (CVD) on Si/SiO_2 substrates at 900^{o}C with ultra-high purity CH_4 and H_2. Individual SWNTs were grown from iron oxide nanoparticles derived from ferritin (Sigma, diluted 20 times in de-ionized water) at random lengths, diameters, chiral angles, directions and non-linear orientations. Randomly grown individual SWNTs form a sub-monolayer two dimensional network, which is isotropic at macroscopic lengths. Average nanotube density is about 6 μm^{-2} with SWNT diameters varying between 1 to 3 nm as verified by Raman spectra, SEM and AFM imaging. A typical Raman spectrum and an SEM image are shown in Figure 3.1. Following fabrication of source and drain electrodes by conventional photolithography and metal deposition methods as described in the previous chapters, equally spaced stripe patterns of SWNT networks along the channel length are obtained by second lithography step and O_2 plasma etching. SEM image of a completed device is shown in Figure 3.1(c). This stripe pattern prevents device-to-device cross-talk as well as the leakage to the silicon back-gate.

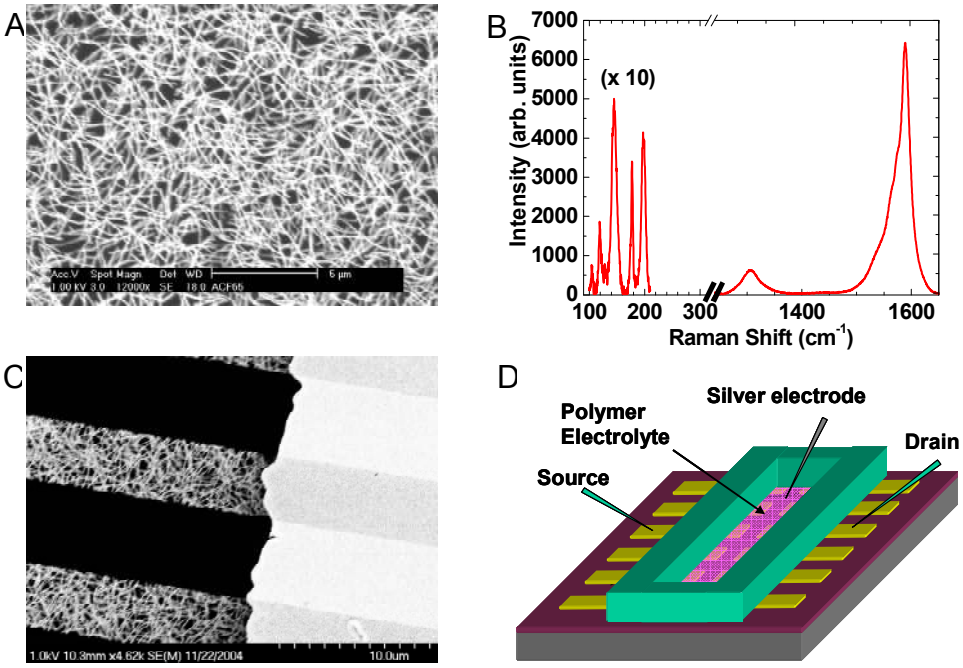

Figure 3.1: (a) SEM image showing a random network of carbon nanotubes. (b) Base-line corrected Raman Spectrum of the SWNT film at 633 nm excitation. The radial breathing modes apparent correspond to diameters between 1 and 3 nm. (c) Low magnification SEM image showing a portion of the channel with striping geometry of a typical device. (d) Schematic of polymer electrolyte gate measurements on carbon nanotube networks.

SWNT network TFTs have been gated by back-gating and polymer electrolyte gating. A schematic of a polymer electrolyte gated TFT is shown in Figure 3.1(d). The device characteristics of a TFT operating with PEO and PEI based electrolytes are compared to back gate operation in Figure 3.2. Summarizing the results of chapter 2, polymer electrolytes can be successfully employed on networks of SWNTs for highly efficient gating and controlling carrier type. Large hysteresis observed in the back-gate operation is eliminated. The same effect with n-channel rather than p-channel operation is observed with PEI electrolyte gating in Figure 3.2(d).

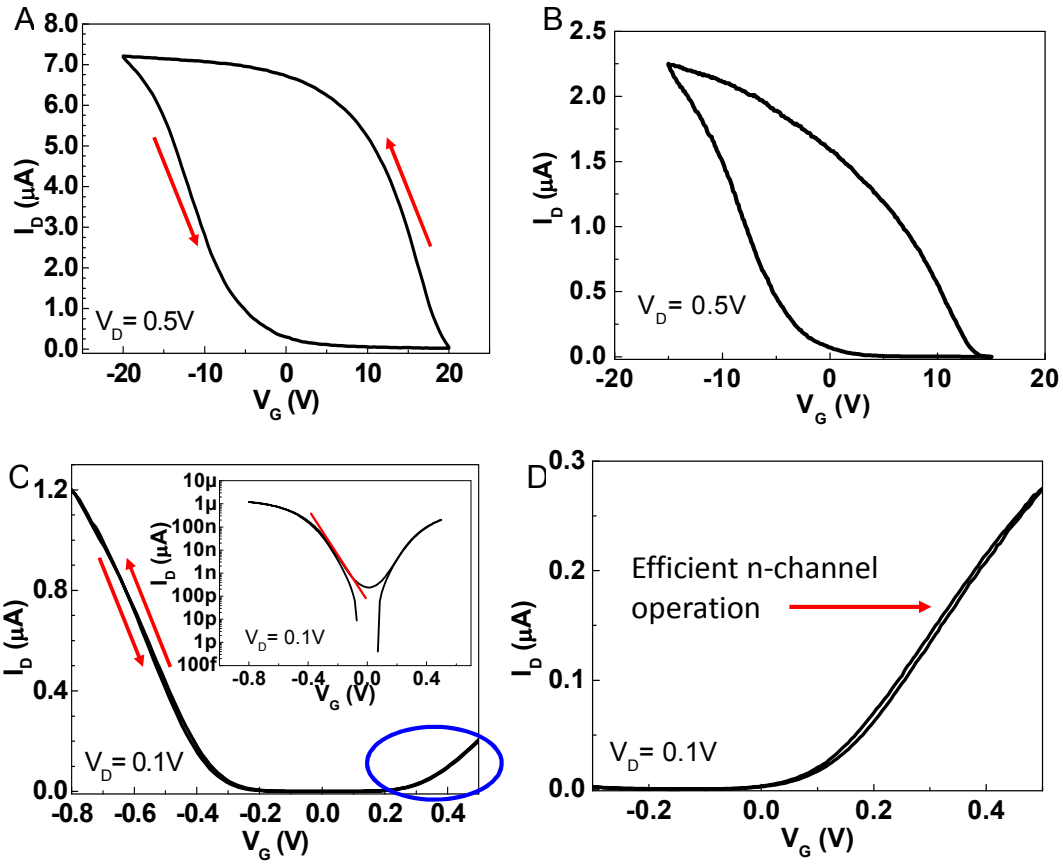

Figure 3.2: (a-b) Transfer characteristics of typical back-gated SWNT TFTs and corresponding PEO (c) and PEI (d) electrolyte gated measurements. In the transfer curves the drain-source voltage is 0.1 V for the polymer-gate measurements, whereas it is 0.5V for the back-gate measurements. Arrows in (a) and (c) correspond to forward and backward sweeps of the gate bias. The inset in (c) shows the transfer curve in semi-logarithmic scale. The red line in the inset shows the sub-threshold slope of the device.

3.3. Gate Capacitance

Polymer electrolyte gating with high efficiencies without the complications of hysteresis allows a more accurate analysis of device performance. To analyze device characteristics, we first estimate the gate capacitance (C_G) and the quantum (chemical) capacitance (C_Q) per unit area of the SWNTs as follows. Since C_G and C_Q are in series, the total capacitance is given by $C_T = (\frac{1}{C_G} + \frac{1}{C_Q})^{-1}$, and the smaller of C_G and C_Q

dominates. C_G for polymer electrolytes may be given as $C_G = \varepsilon\varepsilon_o/\lambda$. As discussed in the previous chapter, we assume the dielectric constant of the interface to be one half of the bulk electrolyte, $\varepsilon \sim 5$ and ε_o is the permittivity of free space.[25,26] λ is the Debye length given by $\sqrt{\frac{\varepsilon\varepsilon_0 kT}{2\rho e^2}}$, where kT is the thermal energy and e is the electric charge following the previous discussions. The concentrations (ρ) of the electrolytes used in our experiments are ~2.8 M and ~6.7 M for PEO/$LiClO_4$ and PEI/$LiClO_4$ electrolytes, respectively. Therefore, we estimate $C_G \sim 1$ F/m^2 for polymer electrolytes.

The quantum capacitance per unit area of the network can be estimated from the quantum capacitance per unit length (C_{Ql}) of individual SWNTs. For simplicity, we consider the network as parallel array of tubes. Per unit area quantity C_Q may then be thought of as the resultant capacitance of a number of parallel capacitors along the channel with capacitance C_{Ql} (i.e. the differential capacitance $C_Q \delta A$ in an area $\delta A = \delta w \cdot \delta l$ will be about the same as the resultant capacitance of δN parallel individual SWNTs along the length δl. Here, δw is the differential width). Thus, we have the following equality:

$$C_Q \delta w \cdot \delta l \approx \delta N (C_{Ql} \cdot \delta l) = \left(\frac{\partial N}{\partial w} \delta w \right) \cdot \left(C_{Ql} \cdot \delta l \right). \qquad \text{Eq. 3.1}$$

This equality leads to an even simpler relation, $C_Q \sim \frac{\partial N}{\partial w} C_{Ql}$. The linear density $\frac{\partial N}{\partial w}$ is estimated from the SEM images by randomly taking several linear cross sections and counting the total number of tubes that cross these sections. The linear density typically

varies between 3 μm^{-1} and 10 μm^{-1}. Mobilities are calculated using the value, $\frac{\partial N}{\partial w} \sim 10$ μm^{-1}, which should give conservative estimates. Due to the assumptions mentioned above, the mobility values are rough estimates but the length scaling trend is the same regardless of the actual value of $\frac{\partial N}{\partial w}$ since the same constant value is used to calculate the mobilities for all polymer gating measurements. With quantum capacitance per unit length, $C_{Ql} \sim \frac{4e^2}{\pi \hbar \upsilon_F} \approx 4 \times 10^{-10} F/m$ when only one sub-band is occupied, quantum capacitance per unit area is $\sim 4 \times 10^{-3} F/m^2$.[27] Since $C_Q << C_G$, the total capacitance $C_T \approx C_Q \approx 4 \times 10^{-3} F/m^2$ for polymer electrolyte gating. For back gate, $C_G \approx \varepsilon \varepsilon_o / t \approx 3.5 \times 10^{-4} F/m^2$ (where t is the thickness of the oxide layer and ε~3.9) is an order of magnitude smaller than C_Q, and therefore justifies the assumption $C_T \approx C_G$.

Assuming diffuse transport, the carrier mobility can then be estimated from the relation:

$$\mu \approx \left| \frac{\partial I_D}{\partial V_G} \right| \frac{L}{w\, C_T V_D}, \qquad \text{Eq. 3.2}$$

where L is the channel length and w is the channel width. The entire physical width of the channel is used to calculate device mobilities with equation (2) for all data presented here. Using an effective width of the sum of SWNT stripes will lead to mobilities that are about twice as high representing values that may be achieved with optimized stripe geometries. For our PEO electrolyte gated devices, hole mobility varies from 10 to 40

cm^2/Vs. These mobilities estimated from our PEO electrolyte gate measurements are in agreement with back-gate measurements for long channel lengths ($L > 10\ \mu m$). We have also extracted the effective per tube mobility from the thin film devices and compared it to the reported mobilities for single nanotube transistors. For a simple estimate of the per tube mobility, we have factored in the effective width (i.e. the sum of the widths of the SWNT stripes) and considered that only ~1.5 % of the each of the stripe width consists of tubes. This fill factor of 1.5 % comes from the estimate that there are only about 10 tubes per 1 μm and that the average diameter of the tubes is ~1.5 nm. These two factors give per tube mobility as $\mu_{tube} = \frac{2\mu_{device}}{0.015}$. The effective per tube mobility calculated from the device mobility range of ~10 to 40 cm^2/Vs measured for PEO gating corresponds to ~1300 to 5300 cm^2/Vs which is within the typical hole mobility range of 1000 to 6000 cm^2/Vs reported for back gated single tube transistors.[27,28] Similar analysis on PEI electrolyte gating measurements leads to same length scaling behavior with electron mobilities that are slightly smaller (by about a factor of 2) than the hole mobilities measured with PEO electrolyte gate for the entire channel length scale studied in this chapter.

3.4. Channel Length Scaling of Electron and Hole Conduction in Thin Film Carbon Nanotube Transistors

With the effectiveness of polymer electrolyte gating on networks of SWNTs established and with estimates of relevant capacitances, we now address performance scaling with device geometry and carrier type. Figure 3.3 compares both short and long

channel length limits for SWNT TFTs. For a short channel device, the channel length is comparable to or even smaller than the average length of the SWNTs as depicted in Figure 3.3(a). In the short channel limit, many SWNTs bridge the source and drain electrodes directly. On the other hand, in the long channel limit the channel length is much longer than the average length of SWNTs. SWNTs form a two dimensional network in the channel. The electrical pathways that connect the source and drain electrodes include multiple SWNTs in the long channel limit as depicted in Figure 3.3(b). The arrays of SWNTs in the channel go through a dramatic transition in terms of electrical characteristics as the channel length varies. Therefore, SWNT arrays differ from classical two-dimensional conducting films, for which conductance is inversely proportional to the channel length following Ohm's law. Typical transfer curves for short and long channel TFTs are also compared in Figure 3.3. For a short channel TFT, the channel is much more conducting than a long channel TFT. However, short channel TFTs cannot be turned off completely.

It is reasonable to consider SWNT arrays as conducting stick networks at a fixed gate potential. In a stick network, the channel conductance is proportional to $\left(\frac{L_s}{L_c}\right)^m$, where L_C is the channel length, L_S is the fixed length of the sticks, and m is a material independent parameter, which depends on the surface density of sticks normalized by the percolation limit and is always greater than or equal to one. The percolation limit can be defined as the critical surface density of sticks above which the stick network is conducting. It depends on the length and orientation of the sticks. The average length of the nanotubes can be considered to be the stick length for interpreting the data. The

percolation limit for a random two-dimensional network has been derived from geometric arguments to be $\frac{4.236^2}{\pi L_S^2}$, and the percolation limit increases as the stick network becomes less random in terms of spatial orientation. [29] For a perfectly anisotropic array of SWNTs with finite lengths, the percolation limit diverges.[29,30]

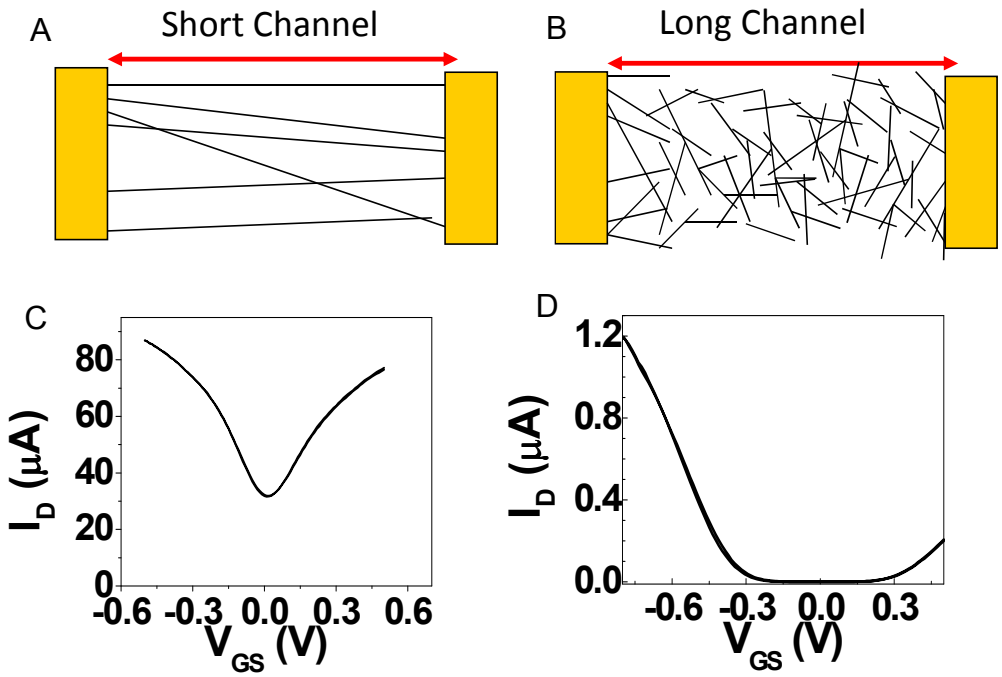

Figure 3.3: (a) Schematics for a SWNT TFT with a short channel. Source and drain electrodes are spanned by SWNTs (black lines). (b) Schematics for a SWNT TFT with a long channel. (c) The transfer curve for a short-channel SWNT TFT. (d) The transfer curve for a long-channel SWNT TFT. The source-drain bias is 0.1 V and the TFTs are PEO electrolyte gated.

Within the frame of stick network modeling, we can qualitatively figure out how the channel conductance should scale with the channel length at different gate voltages. However, one should be careful that this model does not include the resistance due to tube-tube junctions and metal-tube contacts. Hence, we use this model only for qualitative arguments. Let's name channel currents to be on- and off- currents when the

FET is turned on and off by applying gate bias. When the FET is on all SWNTs in the array contribute to the channel conductance. For the off-state, the semiconducting SWNTs in the array become non-conducting. Knowing that the parameter m is close to 1 for very high density of sticks and increases with decreasing density,[29] the parameter m is larger for the off-state. Therefore, one can expect the ratio of on-current to off-current (on/off ratio) to increase with increasing channel length. However, tube-tube junction resistances would be expected to become an important factor for longer channel lengths halting the increase of the on/off ratio.

Here, we present experimental results to support our hypothesis. The ratio of on-current to off-current (on/off ratio) is plotted as a function of channel length in Figure 3.4 for three different types of gating. For a comparison between hole and electron conduction, SWNT TFTs have been gated by both PEO (hole conduction) and PEI (electron conduction) electrolytes. In order to compare with earlier results, length scaling for back-gating is shown as well as the scaling for polymer electrolyte gating. Figure 3.4 indicates that all three gating results exhibit similar saturation behavior past $L \sim 30$ μm. The decay of on/off ratio at short lengths is due to percolation of all metallic tube pathways. Note that pathways composed only of small band gap semiconductors or a mixture of metals and small gap semiconductors may also contribute to increasing off current but for simplicity we may refer to these paths also as all metallic pathways at room temperature. Due to higher percentage of semiconducting tubes (~70%), the probability of all metal pathways quickly diminishes at long channel lengths. Since each path has tubes in series, the tube with the highest resistance (i.e. semiconductors when they are turned off) will dominate leading to an effective semiconductor behavior. We

note that two orders of magnitude higher resistance of metal-semiconductor junctions compared to metal-metal or semiconductor-semiconductor junctions [31] should significantly reduce the contributions from pathways that consist of a mixture of metallic and semiconducting tubes to the on-current.

Figure 3.5 compares the transconductance in the linear regime vs. L for back, PEO, and PEI gating. In the long channel limit ($L > 10\ \mu m$), same qualitative behavior is observed for all three cases. The offset for back gating is due to the difference in gate capacitance (i.e. the inefficient back gating leads to about an order of magnitude smaller transconductance). The lower left inset, which compares the linear hole mobility, shows nearly identical scaling in the long channel limit.

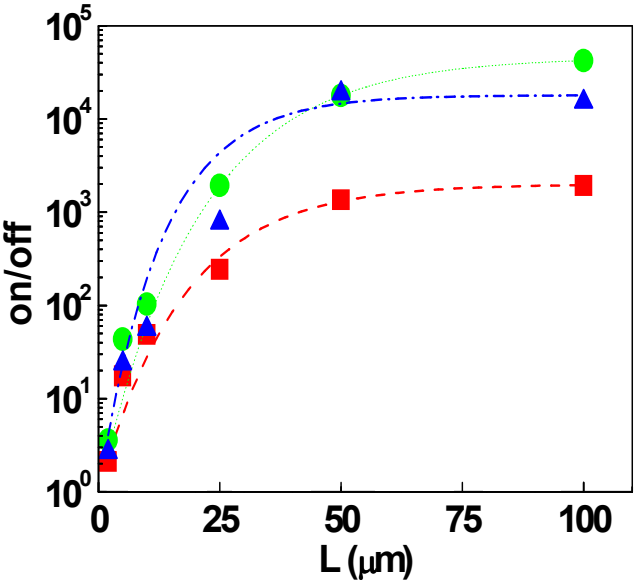

Figure 3.4: On/off current ratio scaling with channel length for back gate (square), PEO (circle), and PEI (triangle) electrolyte gates for a different set of devices with same device geometry. Dashed lines are guides to eye.

As the channel length decreases, distinctly different behavior is seen at $L \sim 10$ μm, which is comparable to the average tube length. Due to the transition from transport

via interconnected tube network to conduction through tubes that directly span the channel, fundamentally different behavior is expected when length scale approaches the average tube length. However, there is an additional deviation in the measured transconductance between back gating and polymer electrolyte gating. This discrepancy in the short channel limit can also be seen in the device mobility in the inset of Figure 3.5 where PEO electrolyte gating leads to nearly constant mobility with channel length whereas large decrease is seen in back gating. Measurements at each channel length shown in Figure 3.5 are made on the same devices and therefore this discrepancy between the two gating methods is not likely to be arising from network to direct connection transition.

When the channel length is comparable or smaller than the average tube length, transport through tubes that directly span source to drain leads to small channel resistance and the contact resistance may become important. In these devices, the electrodes are made of Au with Cr adhesion layer and we can consider Cr to be the contact metal. In this case, the Fermi level pinning should lead to Schottky contacts.[32,33] The observed length dependence in back-gating may then result from Schottky barrier limited transport (there may also be contributions from tunnel barriers at the contacts). In polymer electrolyte gating, the Schottky barrier should in principle become transparent because of the short depletion layer widths due to highly efficient band bending afforded by short Debye lengths of the electrolyte solution. Qualitatively same length scaling of electron (PEI gating) and hole (PEO gating) transport and ambipolar behavior observed for PEO gating (Figure 3.3 and 3.6(b)) but not for back gating (Figure 3.2(a) and 3.6(a)) further support this idea. These observations are consistent with contact resistance contributing

significantly to the apparent carrier mobility decrease in back gate measurements at short channel lengths.

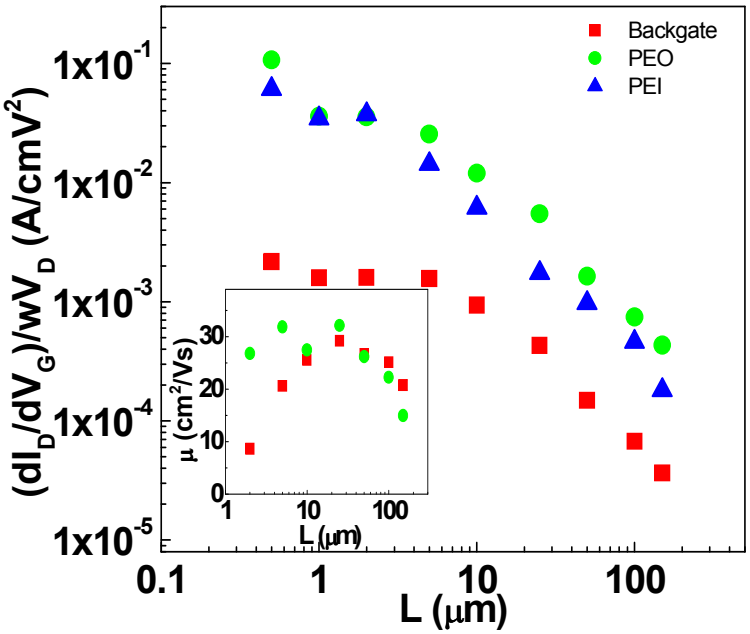

Figure 3.5: Scaling of drain-source voltage and channel width normalized transconductance in the linear regime with channel length for back gate (square), PEO (circle), and PEI (triangle) electrolyte gates. Note that all channel widths are 250 μm except for two shortest channel lengths (0.5 and 1 μm) which have widths of 10 μm. The inset shows the hole mobility scaling with channel length calculated from transconductance and capacitances discussed in the text. The mobility values are obtained by averaging two sets of devices to improve accuracy. Note that these are the device mobilities calculated using the entire channel width rather than effective widths of the nanotube network stripes.

However, direct comparison of the transfer characteristics of short channel devices suggests that other effects may give rise to the discrepancy between back and polymer electrolyte gating. Figure 3.6 compares the transfer characteristics of the same 2 μm channel SWNT TFT operating under back-gating and PEO electrolyte gating. The transconductance at positive gate voltages for forward sweep (negative to positive) decreases significantly and the current never quite reaches a minimum in back gating

whereas a distinct minimum and the onset of n-channel conduction is seen for PEO electrolyte gating. Contribution from contact resistance should appear largely as limited on-current and is unlikely to account for this observation. Comparison of back and polymer gating in Figure 3.6 suggests that there may be a significant reduction in back gate efficiency at short channel lengths. It is most likely that a combination of differences in contact resistances as well as in gate efficiencies gives rise to the observed divergent behavior between back and electrolyte gating of short channel devices. While further studies are required to elucidate these deviations arising at short channel lengths, polymer electrolyte gating of SWNT TFTs seems to conform better to expectations based on characteristics of individual tubes (i.e. nearly constant mobility at short channel lengths).

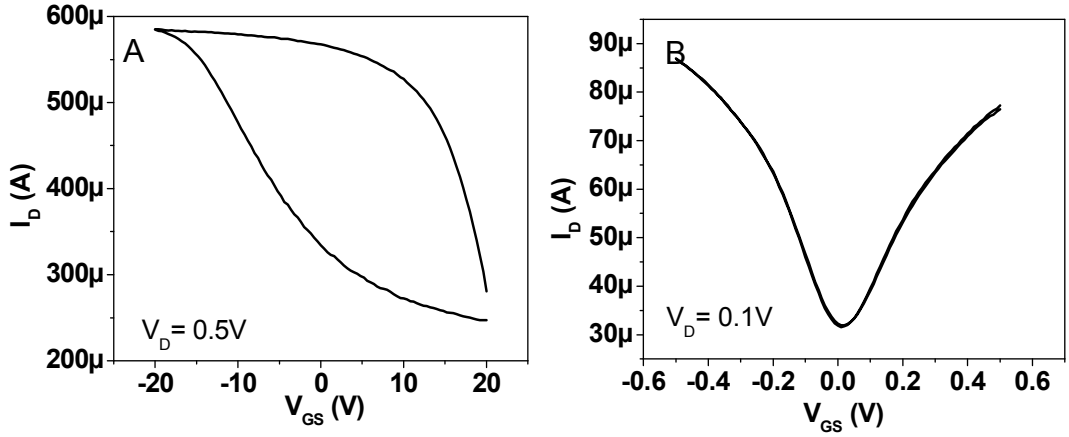

Figure 3.6: Comparison of transfer characteristics measured by back (a) and PEO electrolyte (b) gating on the same 2 µm channel length device.

3.5. Anisotropic Arrays of Carbon Nanotubes

Characterizing the length scaling in SWNT TFTs, we will now discuss the effect of spatial anisotropy of SWNT arrays on device behavior. Our previous analysis assumes the SWNT network to be isotropic in two dimensions. We have studied aligned arrays of linearly grown SWNTs as an anisotropic electronic material in the channel of SWNT TFTs. In this section, we will first discuss how to synthesize perfectly aligned arrays of SWNTs grown horizontally on the substrate.

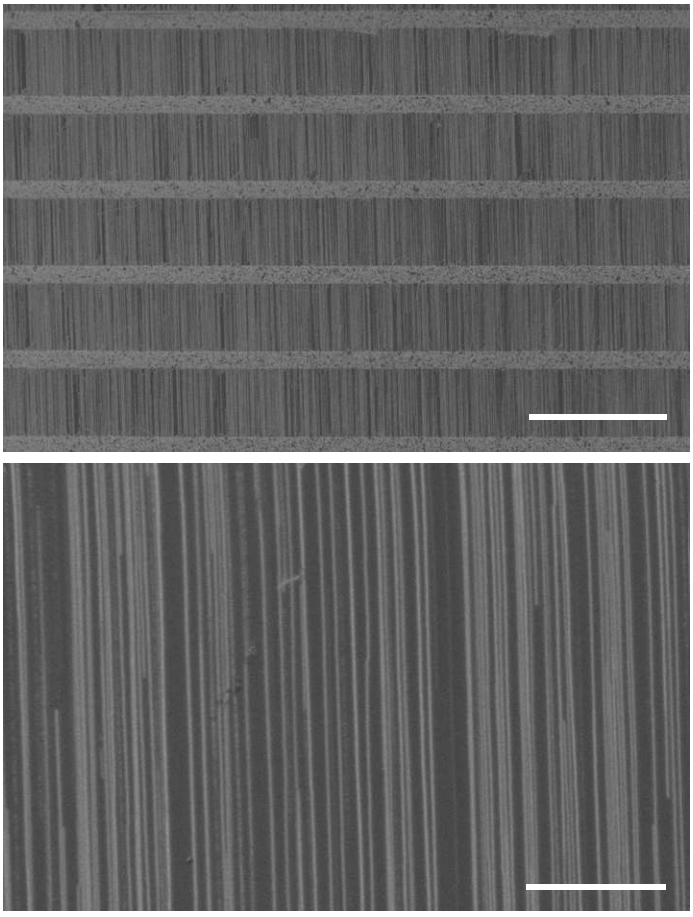

Figure 3.7: Scanning electron microscope images of aligned SWNTs grown from patterned iron oxide catalyst lines on single crystal quartz. The scale bars are 100 μm and 10 μm, respectively.

Arrays of SWNTs with almost perfect alignment and linearity have been shown to grow horizontally on single crystal quartz and sapphire substrates without any technical difficulties.[34--36] We have grown aligned arrays of carbon nanotubes on single crystal quartz substrates. Figure 3.7 shows typical SEM images of aligned SWNT arrays grown on ST-cut single crystal quartz by thermal CVD from patterned iron catalyst lines. Almost all SWNTs have grown linearly and parallel to one another on the substrate with very few exceptions as shown in Figure 3.7. Recent studies suggest that a strong interaction with the substrate is necessary for spatially guiding SWNTs perfectly along a particular crystallographic direction at high growth temperatures.[37] Whether or not such an interaction alters the characteristics of the resulting SWNTs will be discussed in the next chapter, however experimental evidence suggest that aligned SWNTs can be used as high performance electronic materials for TFT applications with even better performance than isotropic SWNT networks.[37]

We have fabricated TFTs on aligned arrays of SWNTs grown on ST-cut quartz very similar to SWNT network TFTs fabricated on Si/SiO_2 substrates. Figure 3.8 compares the channel length scaling of the on/off ratio for TFTs fabricated on networks of randomly grown SWNTs and aligned arrays of SWNTs. The electrical performance for both types of TFTs differs significantly as the channel length increases because arrays of aligned SWNTs never behave as a network. The overall device behavior is mostly dominated by the individual SWNTs that span the channel rather than a collective network behavior independent of the channel length.

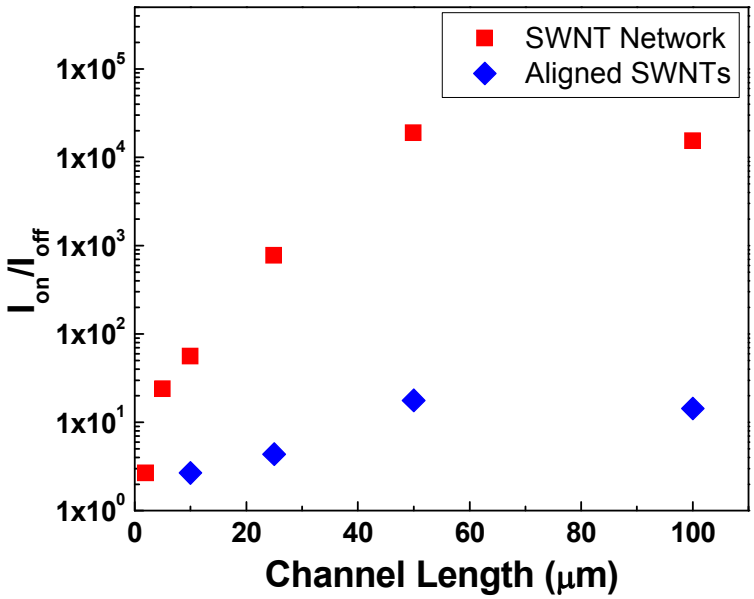

Figure 3.8: On/off current ratio scaling with channel length for randomly grown isotropic SWNT network (square) and aligned arrays of SWNTs (diamond) for a different set of devices with the same device geometry.

3.6. Conclusions & Future Challenges

We have characterized the channel length dependence of SWNT TFTs by polymer electrolyte gating. Qualitatively different behavior between back and polymer electrolyte gating at short channel lengths has been shown suggesting that polymer electrolyte gating may be a valuable and a very simple method of characterizing nanoscale semiconductor devices. The ability to control the mode of operation from p- to n-type demonstrates the versatility of polymer electrolytes beyond efficient gate media. We have shown that networks of randomly grown SWNTs make a class of high performance electronic materials at length scales greater than ~25 μm with device

mobility values greater than 10 cm^2/Vs and high on/off ratios. SWNT TFTs may be a cost-effective solution for many developing macro-electronic applications.

3.7. List of References

[1] M. Shim, Mater. Matters **2**, 16 (2007).

[2] M. S. Dresselhaus, G. Dresselhaus, and R. Saito, Phys. Rev. B **45**, 6234 (1992).

[3] R. Saito, G. Dresselhaus, and M. S. Dresselhaus, Physical Properties of Carbon Nanotubes (Imperial College Press, London, 1998), p. 259.

[4] J. W. Mintmire, B. I. Dunlap, and C. T. White, Phys. Rev. Lett. **68**, 631 (1992).

[5] C. Dekker, Phys. Today **52**, 22 (1999).

[6] P. L. McEuen, M. S. Fuhrer, and H. K. Park, IEEE Trans. Nanotech. **1**, 78 (2002).

[7] S. J. Tans, A. R. M. Verschueren, and C. Dekker, Nature **393**, 49 (1998).

[8] R. Martel, T. Schmidt, H. R. Shea, T. Hertel, and P. Avouris, Appl. Phys. Lett. **73**, 2447 (1998).

[9] J. Kong, N. R. Franklin, C. W. Zhou, M. G. Chapline, S. Peng, K. J. Cho, and H. J. Dai, Science **287**, 622 (2000).

[10] V. Derycke, R. Martel, J. Appenzeller, and P. Avouris, Nano Lett. **1**, 453 (2001).

[11] A. Bachtold, P. Hadley, T. Nakanishi, and C. Dekker, Science **294**, 1317 (2001).

[12] A. Hartschuh, H. N. Pedrosa, L. Novotny, and T. D. Krauss, Science **301**, 1354 (2003).

[13] M. S. Arnold, J. E. Sharping, S. I. Stupp, P. Kumar, and M. C. Hersam, Nano Lett. **3**, 1549 (2003).

[14] H. Htoon, M. J. O'Connell, P. J. Cox, S. K. Doorn, and V. I. Klimov, Phys. Rev. Lett. **93**, 027401 (2004).

[15] T. Durkop, S. A. Getty, E. Cobas, and M. S. Fuhrer, Nano Lett. **4**, 35 (2004).

[16] Y. Nosho, Y. Ohno, S. Kishimoto, and T. Mizutani, Appl. Phys. Lett. **86**, 073105 (2005).

[17] M. Shim, J. H. Back, T. Ozel, and K. W. Kwon, Phys. Rev. B **71**, 205411 (2005).

[18] M. Shim, A. Gaur, K. T. Nguyen, D. Abdula, and T. Ozel, J. Phys. Chem. C **112**, 13017 (2008).

[19] T. Ozel, D. Abdula, E. Hwang, and M. Shim, ACS Nano **3**, 2217 (2009).

[20] A. Gaur and M. Shim, Phys. Rev. B **78**, 125422 (2008).

[21] C. J. Wang, Q. Cao, T. Ozel, A. Gaur, J. A. Rogers, and M. Shim, J. Am. Chem. Soc. **127**, 11460 (2005).

[22] E. S. Snow, J. P. Novak, P. M. Campbell, and D. Park, Appl. Phys. Lett. **82**, 2145 (2003).

[23] Y. X. Zhou, A. Gaur, S. H. Hur, C. Kocabas, M. A. Meitl, M. Shim, and J. A. Rogers, Nano Lett. **4**, 2031 (2004).

[24] T. Ozel, A. Gaur, J. A. Rogers, and M. Shim, Nano Lett. **5**, 905 (2005).

[25] A. Abrashkin, D. Andelman, and H. Orland, Phys. Rev. Lett. **99**, 077801 (2007).

[26] G. P. Siddons, D. Merchin, J. H. Back, J. K. Jeong, and M. Shim, Nano Lett. **4**, 927 (2004).

[27] S. Rosenblatt, Y. Yaish, J. Park, J. Gore, V. Sazonova, and P. L. McEuen, Nano Lett. **2**, 869 (2002).

[28] A. Javey, J. Guo, Q. Wang, M. Lundstrom, and H. J. Dai, Nature **424**, 654 (2003).

[29] G. E. Pike and C. H. Seager, Phys. Rev. B **10**, 1421 (1974).

[30] C. Kocabas, N. Pimparkar, O. Yesilyurt, S. J. Kang, M. A. Alam, and J. A. Rogers, Nano Letters **7**, 1195 (2007).

[31] M. S. Fuhrer, J. Nygard, L. Shih, et al, Science **288**, 494 (2000).

[32] F. Leonard and J. Tersoff, Phys. Rev. Lett. **83**, 5174 (1999).

[33] F. Leonard and J. Tersoff, Phys. Rev. Lett. **84**, 4693 (2000).

[34] A. Ismach, L. Segev, E. Wachtel, and E. Joselevich, Angew. Chem. Int. Ed. **43**, 6140 (2004).

[35] C. Kocabas, S. H. Hur, A. Gaur, M. A. Meitl, M. Shim, and J. A. Rogers, Small **1**, 1110 (2005).

[36] C. Kocabas, S. J. Kang, T. Ozel, M. Shim, and J. A. Rogers, J. Phys. Chem. C **111**, 17879 (2007).

[37] S. J. Kang, C. Kocabas, T. Ozel, M. Shim, N. Pimparkar, M. A. Alam, S. V. Rotkin, and J. A. Rogers, Nature Nanotech. **2**, 230 (2007).

CHAPTER 4

NON-UNIFORM UNIAXIAL COMPRESSIVE STRAIN IN HORIZONTALLY ALIGNED CARBON NANOTUBES

Significant components of this chapter was published as "Non-Uniform Compressive Strain in Horizontally Aligned Single-Walled Carbon Nanotubes Grown on Single Crystal Quartz", T. Ozel, D. Abdula, E. Hwang, and M. Shim, **ACS Nano, 3**, 2217 (2009).

4.1. Introduction

Single-walled carbon nanotubes (SWNTs) possess a combination of exceptional electrical and mechanical properties that may help to advance multiple areas of technology including electronic and electromechanical systems.[1,2] However, as with many nanoscale materials, there remain challenges to overcome before SWNTs can be considered for integration into high performance devices beyond those of proof-of-concept. In general, most applications exploiting unique properties of nanoscale materials will require robust means of patterning/positioning of individual components into ordered assemblies or arrays. Near perfect horizontal alignment on crystalline substrates is arguably the biggest recent advance that has been made towards overcoming this challenge for SWNTs.[3--6] Direct chemical vapor deposition (CVD) of parallel arrays of SWNTs has been achieved on both single crystal quartz and sapphire substrates.[3,5,6] Levels of alignment > 99.9% has been demonstrated with growth on quartz.[7] This high

degree of alignment is exemplified in Figure 4.1 where SEM images of two different density samples are shown. For spatially guiding SWNTs perfectly along a particular crystallographic direction at high growth temperatures, relatively strong interaction with the substrate is expected and has been shown to be necessary.[8--10] However, whether or not such an interaction alters the characteristics of the resulting SWNTs has not been considered.

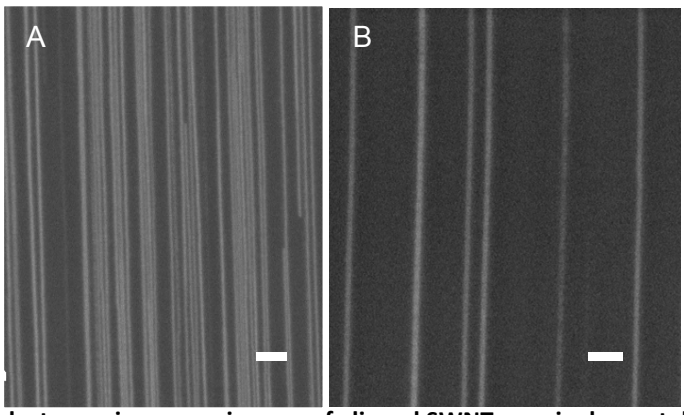

Figure 4.1: Scanning electron microscope images of aligned SWNTs on single crystal quartz with high (a) and low (b) densities. The scale bars are 2 μm.

Understanding interactions with the surrounding media including the substrate and controlling them are key challenges to overcome for any nanoscale material en route to applications. However, how the inherent properties of SWNTs are affected by forces that allow horizontal alignment on quartz has not been examined. The local chemical environment and its possible variations can and have led to controversies on our interpretation of observed behavior of SWNTs.[11--20] Elucidating how the interaction with the substrate that enables alignment affects desired properties is then critical. Here, we show that the substrate-SWNT interaction leads to non-uniform mechanical strain in aligned SWNTs grown on single crystal quartz. These strained SWNTs in turn allow

experimental observation of how difficult-to-achieve uniaxial compression affects vibrational properties of SWNTs.

4.2. Methods

SWNTs were grown by CVD on both pre-annealed ST-cut single crystal quartz (Hoffman Materials) and Si/SiO_2 (300 nm thermal oxide). The substrates were annealed in air at 900 C for 8 hours to reconstruct the surface crystal structure after sonicating in acetone bath for 5 minutes. We observed that the alignment quality is lowered for shorter annealing times or when we annealed the substrate at temperatures below 800 C and above 1000 C. Besides annealing, substrates with low polishing quality or substrates with unclean surfaces offered a lower quality of alignment.

Ferritin or e-beam evaporated Fe patterns and EtOH vapor were used as catalyst and the carbon source, respectively, following previous reports.[3,21] To minimize the effect of growth to growth variations on our analysis, samples on quartz and Si/SiO_2 substrates were grown in the same furnace simultaneously for comparison. However, the results were the same as the comparison of samples grown at different times.

Only samples with low density (< 1 SWNT/μm) were used to ensure that the results were not complicated by Raman signals from multiple SWNTs. Raman spectra were collected using a Jobin-Yvon confocal Raman microscope through a 100X air objective with a 633 nm laser source. The laser spot size was ~ 1 μm and the laser power was kept at 4.5 mW. We studied the effect of laser heating at different powers, but we did not detect any change in the Raman spectra for laser powers ranging from 0.1 mW to 10

mW unlike what we observed for SWNT bundles. The backscattered light was collected through a confocal hole and 1800 grooves/mm grating to a thermoelectrically cooled CCD detector with each pixel representing ~ 0.3 cm^{-1}. Unless otherwise noted, all spectra were collected on as-grown SWNTs where the last step before data collection was the CVD growth. For temperature dependence measurements, SWNTs were heated under Ar flow in a controlled environment chamber with an optical window for Raman measurements.[22]

4.3. Effects of Substrate Induced Alignment on the Raman Spectra of Carbon Nanotubes

The Raman spectra of as-grown SWNTs aligned on crystalline quartz often exhibit an anomalous up-shift in the G-band phonon mode frequencies. High G-band frequencies have been reported in the very first report of aligned growth on crystalline quartz[3] as well as in Supplementary Figure S3(b) of ref. [23] but has not been explained. The bottom spectrum in Figure 4.2(a) demonstrates this anomalous up-shift for an as-grown semiconducting SWNT where the G-band longitudinal optical (LO) mode, the G^+ peak, appears at 1605 cm^{-1}. For comparison, the top spectrum is of a typical semiconducting SWNT grown on Si/SiO_2 substrates. For this non-aligned SWNT, the G^+ peak appears at 1593 cm^{-1}. Since metallic SWNTs' Raman spectra are complicated by softening and broadening[24--27] caused by the Kohn anomaly,[26,28,29] our discussion here is limited to semiconducting SWNTs and therefore all acquired G-band spectra have been fitted to Lorentzian peaks.

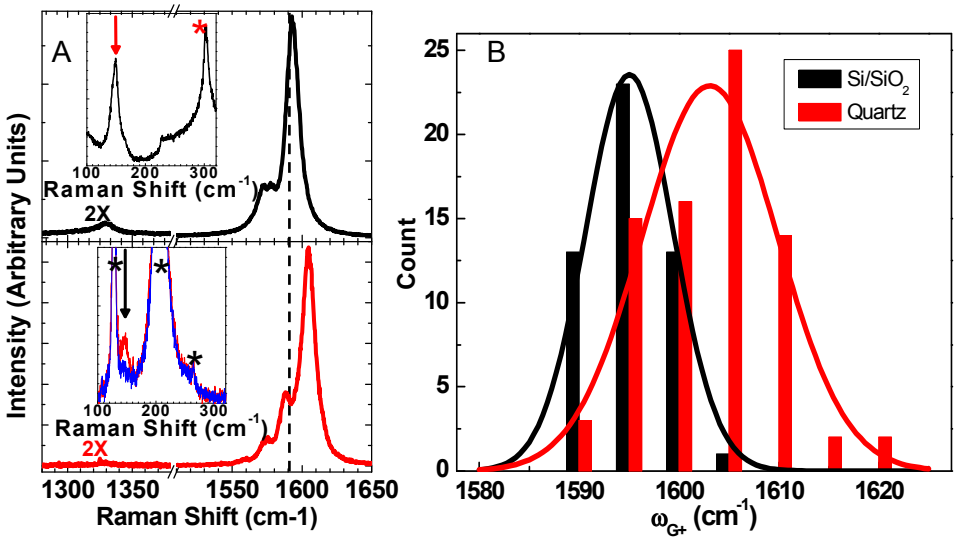

Figure 4.2: (a) Raman D- and G-band spectra of two different as-grown semiconducting SWNTs on Si/SiO_2 (top, black) and single crystal quartz (bottom, red) substrates. Insets are the corresponding radial breathing mode (RBM) regions. Two SWNTs exhibit nearly identical RBM frequencies indicated by the arrows at148 cm^{-1} for the top spectrum and at 147 cm^{-1} for the bottom spectrum. Peaks indicated by * are Raman peaks of the substrates. Blue curve in the bottom inset is the Raman spectrum of quartz substrate only. (b) Histograms of G^+ Raman peak frequency distribution of as-grown SWNTs on Si/SiO_2 (black) and single crystal quartz (red) substrates. Histograms are fitted to Gaussians. The average G^+ Raman peak frequency of SWNTs on quartz is up-shifted by ~8 cm^{-1}.

The insets in Figure 4.2(a) show the radial breathing mode (RBM) regions of the two semiconducting SWNTs. The same RBM frequency does not necessarily guarantee that these two are of identical chirality since local variations in the substrate may cause slight shifts in RBM frequencies.[30] However, given nearly identical RBM frequencies, it is possible that these two SWNTs are of the same chirality. More importantly, both theory and experiments indicate that ω_{G+} is independent of diameter and chirality for semiconducting SWNTs.[31,32] Figure 4.2(b) compares histograms of Raman G^+ peak frequencies (ω_{G+}) of 127 isolated semiconducting SWNTs on Si/SiO_2 and on crystalline quartz. From Gaussian fits (solid lines), the average ω_{G+} for SWNTs aligned on quartz is up-shifted by ~8 cm^{-1}. These observations verify that the anomalous up-shift is not a

result of chirality-dependent properties but rather a consequence of different interactions with the substrates.

4.4. Substrate Induced Uniaxial Compressive Strain on Carbon Nanotubes & the Temperature Tuning of the Strain

At a fixed temperature and laser energy and intensity, there are three known processes that can affect the G-band Raman spectra of SWNTs: 1) defect introduction,[33,34] 2) doping/carrier injection,[35--37] and, 3) mechanical strain.[38,39] We can minimize potential defect contributions by examining SWNTs with little or no D-band intensities. The histograms in Figure 4.2(b) include data only from SWNTs with D/G intensity ratio < 0.05 but including SWNTs with relatively large D/G ratio does not change the frequency distribution significantly. Most semiconducting SWNTs do not exhibit significant D-band intensities on both types of substrates. When the D-band is observable, the average value and the distribution of D/G ratios are similar for both cases indicating that there is no significant difference in the degree of disorder between SWNTs grown on Si/SiO_2 and single crystalline quartz. Furthermore, in Figure 4.2, the individual SWNT grown on Si/SiO_2, despite its larger D/G ratio, exhibits ω_{G+} much closer to the expected phonon frequency than the individual SWNT aligned on quartz, which does not exhibit a detectable D-band intensity. Based on all of these observations, we rule out physical disorder as a possible origin of the anomalous up-shift in the G-band frequency.

If we consider the up-shift in the G-band frequency to arise solely from doping effects, the degree of doping corresponding to the observed G-band frequency shift may

be estimated in the following two ways. First, if we follow Tsang et al.[37] and consider phonon energy renormalization due to doping, then the 8 cm^{-1} up-shift should correspond to a minimum of ~0.013 (0.004) carriers per C atom for 1 nm (2 nm) diameter semiconducting SWNT. Note that 1 to 2 nm is the diameter range observed for SWNTs grown on both substrates. These are rather high doping levels comparable to those of graphite intercalation compounds and are unlikely to be sufficiently explained by phonon energy renormalization which considers low doping limits. Second, if we then assume that the G-band frequency shift is comparable to that of graphite intercalation compounds following Rao et al.,[35] then the 8 cm^{-1} up-shift corresponds to an even larger doping fraction difference of 0.017 carriers (holes) per C atom. While the degree of substrate induced doping may vary locally,[36] given that quartz and the thermal oxide on Si are both highly insulating, it is unlikely that such a large difference in the average G-band frequency can be accounted for by doping effects. We are then left with the possibility of mechanical strain as the origin of the anomalous up-shift in the G-band frequency.

Previous experimental studies have shown that the G-band phonon energy decreases when SWNTs are under uniaxial tension.[38--40] Especially with the possibility of electronic structure modification with strain,[41,42] elucidating both tensile and compressive responses of SWNTs is important in terms of fundamental understanding of the material's property as well as enabling new technologies such as nanoelectromechanical systems and flexible electronics. A recent theoretical study has indicated that uniaxial compression of SWNTs should lead to significant up-shifts in the G-band phonon frequencies.[43] However, due to difficulties in applying uniaxial

compression, only hydrostatic pressure, often on ensembles of SWNTs, has been experimentally explored.[44--46] Given that relatively strong interaction with the substrate is needed to align along $[2\,\bar{1}\,\bar{1}\,0]$ direction at growth temperatures and that the degree of thermal contraction upon cooling should be different for SWNT and crystalline quartz, SWNTs should, in fact, be expected to be under compressive stress. If so, aligned SWNTs on quartz may provide readily accessible experimental conditions to examine often hard-to-achieve uniaxial compression.

In order to verify that aligned SWNTs grown on single crystal quartz are under compression, we now compare the temperature (*T*) dependence of Raman G-band frequencies of samples grown on single crystal quartz with that of samples grown on Si/SiO_2. Raman G-band spectra at different *T* for a typical SWNT grown on Si/SiO_2 and one grown on single crystal quartz are shown in Figure 4.3(a) and Figure 4.3(b), respectively. The near linear *T* dependence of ω_{G+} of SWNT on Si/SiO_2 as shown for three different SWNTs in the bottom data set in Figure 4.3(c) is expected in the *T* range studied here and is in quantitative agreement with previous reports.[47--50] From linear curve fits, we obtain the slope for the thermal response of SWNTs on Si/SiO_2 substrate as $\left(d\omega_{G+}/dT\right)_{Si/SiO_2} \sim -0.03$ cm^{-1}/K. We have observed $\left(d\omega_{G+}/dT\right)_{Si/SiO_2}$ ranging from -0.025 to -0.035 cm^{-1}/K. Previously reported values range similarly from ~ -0.02 to -0.04 cm^{-1}/K.[47--50] SWNTs grown on single crystal quartz that start out with anomalously up-shifted $\omega_{G+} > 1600$ cm^{-1} at room *T* also exhibit decreasing ω_{G+} with increasing *T* as shown in Figure 4.3(b). However, there is a distinct quantitative difference with *T* response being more than twice as large [$\left(d\omega_{G+}/dT\right)_{Quartz} \sim -0.075$ cm^{-}

^{1}/K] as shown for three different SWNTs on quartz in the upper graph of Figure 4.3(c). When ω_{G+} starts out > 1600 cm^{-1} at room T, we have observed $\left(d\omega_{G+}/dT\right)_{Quartz}$ to vary from −0.07 to −0.08 cm^{-1}/K, consistently lager than that of SWNTs on Si/SiO$_2$.

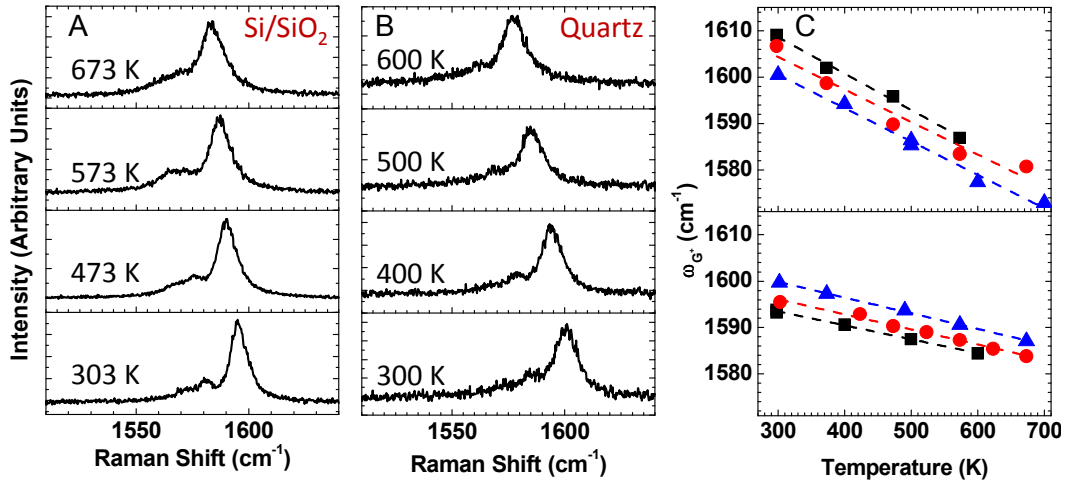

Figure 4.3: Raman G-band spectra of individual as-grown semiconducting SWNTs on Si/SiO$_2$ (a) and on single crystal quartz (b) substrates at the indicated temperatures. (c) Temperature dependence of G$^+$ Raman peak frequencies of several SWNTs grown on quartz (upper graph) and Si/SiO$_2$ (lower graph) substrates. The dashed lines are linear fits.

The T response of SWNTs grown on Si/SiO$_2$ (as well as on quartz when the initial ω_{G+} is near 1590 cm^{-1}) is similar to the reported results for SWNTs suspended above the substrate (−0.025 cm^{-1}/K as reported by Zhang et al. [50]). They are also very similar to theoretical expectations for graphene E_{2g} mode (G-band) that include 3- and 4-phonon scattering and lattice thermal expansion contributions.[51] Given the similarities between our results for SWNTs on Si/SiO$_2$ to both theory and experiments including suspended SWNTs, we assume $\left(d\omega_{G+}/dT\right)_{Si/SiO_2} \sim -0.03$ cm^{-1}/K to be the intrinsic response of semiconducting SWNTs in the absence of mechanical strain. Since the coefficient of thermal expansion (CTE) of Si/SiO$_2$ and the calculated CTE of SWNTs are similar,[52] it

is not surprising that SWNTs on Si/SiO_2 exhibit similar behavior as those suspended above the substrate. Single crystal quartz, on the other hand, exhibits a much larger thermal expansion upon heating. Within the *T* range studied here, single crystal quartz expands nearly linearly along the SWNT growth direction with CTE ~ 1.7 x 10^{-5} /K.[53,54] Although the axial CTE of SWNTs may depend on chirality, it is expected to be at least about an order of magnitude smaller than that of single crystal quartz along the growth direction.[53--55] Assuming, then, direct thermal expansion of SWNT to be negligible compared to that of the quartz substrate, a change in the uniaxial strain, $d\varepsilon$, of ~0.5% on SWNTs is expected for a *T* change, *dT*, of 300 K or $d\varepsilon / dT \approx 0.0017$ %/K. For simplicity, if we assume that the substrate induced strain does not alter the inherent anharmonic contributions to *T* dependent ω_{G+} shift, we can estimate the mechanical strain component of the observed *T* dependence as:

$\left(d\omega_{G+} / dT\right)_{Strain} \approx \left(d\omega_{G+} / dT\right)_{Quartz} - \left(d\omega_{G+} / dT\right)_{Si/SiO_2} = -0.075$ cm^{-1}/K + 0.03 cm^{-1}/K = -0.045 cm^{-1}/K. Since the multi-phonon terms are expected to dominate over the lattice expansion contribution in the inherent *T* dependence of ω_{G+},[47,49--52] this is a reasonable assumption. We then have $d\omega_{G+} / d\varepsilon \sim -27$ cm^{-1}/% strain in excellent agreement with calculated value of ~ -24 cm^{-1}/% strain for a semiconducting (17, 0) SWNT in the small strain limit.[43] These results, combined with the fact that compressive stress leads to an up-shift in ω_{G+} whereas tensile stress leads to a down-shift, indicate that horizontally aligned SWNTs grown on single crystal quartz substrate are, on average, under significant axial compression. The range of observed up-shift in ω_{G+} corresponds to a maximum compressive strain of up to ~1.1% (assuming zero-strain ω_{G+}

to be 1590 cm^{-1}). This is already a substantial amount but we suspect that there may be local regions of even higher degree of strain as discussed in the next section.

4.5. Non-uniformity of Axial Strain and its Origin

Having established that the observed anomalous average ω_{G+} up-shift and the large T response arise from single crystal quartz substrates inducing uniaxial compression, we now examine ω_{G+} along the length of individual SWNTs. Figure 4.4 compares ω_{G+} along a SWNT grown on Si/SiO_2 with that of one grown on quartz. As expected, there is very little variation (< 1 cm^{-1}) on SWNT grown on Si/SiO_2 substrate as shown in Figure 4.4(a). However, large and apparently random fluctuations (standard deviation of ~7 cm^{-1}) in ω_{G+} of SWNTs aligned on single crystal quartz are evident. The G^- peak frequency (ω_{G-}) variations along the length of the same SWNT, shown in Figure

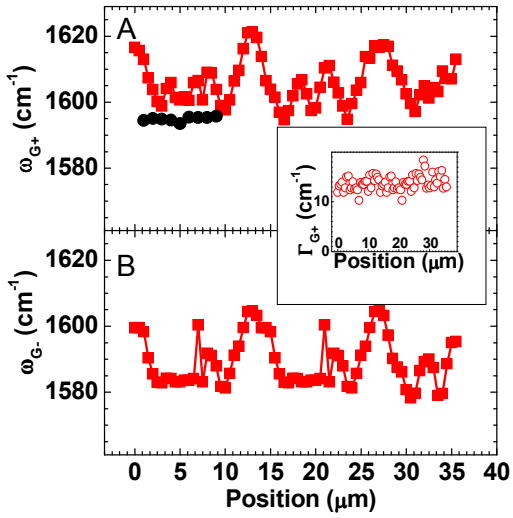

Figure 4.4: (a) Spatial profile of Raman G^+ peak frequency along the length of an as-grown semiconducting SWNT on a Si/SiO_2 (black circles) and quartz (red squares) substrates. (b) Spatial profile of Raman G^- peak frequency along the length of the same SWNT on quartz (red squares) as in (a). Inset shows the variation of the line width of the G^+ peak along the aligned SWNT on quartz.

4.4(b), follow ω_{G+} fluctuations closely. The line width (Γ_{G+}), on the other hand, appears to be independent of the G-band peak frequency variations (Figure 4.4 inset). While there is no obvious periodicity or trend, these ω_{G+} fluctuations with the minimum value always being greater than 1590 cm^{-1} suggest non-uniform compressive strain along the length of SWNTs.

In order to verify the non-uniformity of the substrate induced compressive strain, we again examine how ω_{G+} varies with T. Figure 4.5 shows the T dependence of ω_{G+} at two different locations of the same SWNT. Red circles are from a location with anomalously up-shifted ω_{G+} at room T (1607 cm^{-1}) and the blue circles are from a nearby location with "normal" (or unstrained) ω_{G+} at room T (1595 cm^{-1}). Results from a SWNT grown on Si/SiO_2 are also shown for comparison. The anomalous initial ω_{G+} region has a large $d\omega_{G+}/dT \sim -0.07$ cm^{-1}/K whereas the "normal" initial ω_{G+} region follows the same trend as SWNTs on Si/SiO_2. That is, only regions with initial high ω_{G+} values are under compressive strain. The inset shows the near linear dependence of thermal response of ω_{G+} shift on the initial room T ω_{G+} values for SWNTs on both Si/SiO_2 and quartz substrates. The spatial variations both in ω_{G+} and $d\omega_{G+}/dT$ support the idea that the compressive strain in as-grown SWNTs on quartz is non-uniform in nature.

Given the necessity of strong interaction for alignment and the large difference in CTE with the substrate, the presence of significant compressive strain in SWNTs aligned on quartz is, at least in hindsight, not surprising. However, the non-uniformity may be somewhat unexpected. To address the origin of this non-uniformity, we now consider

surface roughness of the substrate. Figure 4.6 compares Raman G-band image with the corresponding AFM image of two adjacent aligned SWNTs on single crystal quartz. One of the gold markers deposited prior to CVD growth to ensure same location being studied is also visible on the right edge of both images. Figure 4.6(b) is the G-band intensity map where we have integrated area only between 1590 and 1600 cm^{-1}. This selective Raman map highlights parts of SWNTs where there is minimal strain (i.e. regions where ω_{G+} values are close to the "normal" expected frequency of ~1590 – 1595 cm^{-1} correspond to the bright spots). Figure 4.6(a) is a composite of 2 AFM images where the middle part has been collected at a higher resolution and has been adjusted to highlight the surface roughness of the single crystal quartz substrate. The parallel lines that are at ~ 30° to

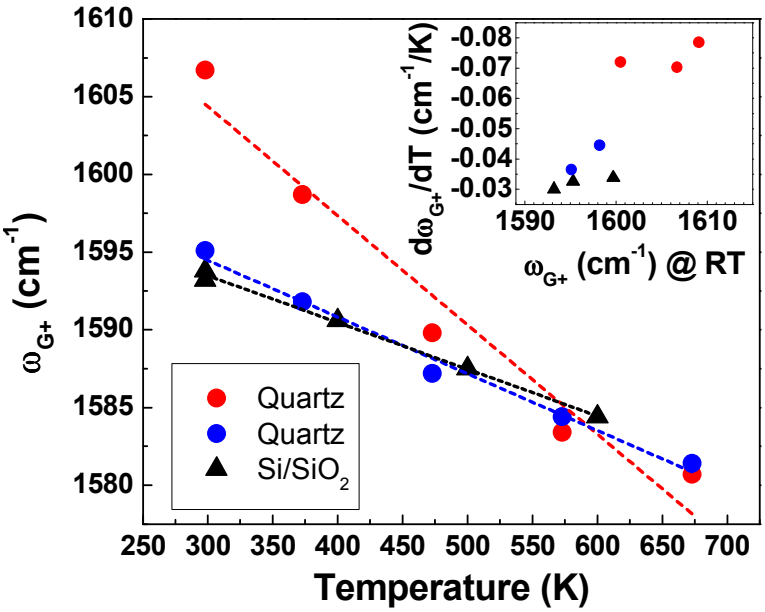

Figure 4.5: Temperature dependence of Raman G^+ peak frequency of individual SWNTs grown on quartz and on Si/SiO_2. The dashed lines are linear fits. Inset shows the relation between the thermal response of G^+ peak frequency shift and the room temperature G^+ peak frequency for various SWNTs grown on both types of substrates. In both the inset and the main panel, blues circles correspond to the less frequent regions of low room temperature G^+ peak frequency and the red circles correspond to the more common cases of high room temperature G^+ peak frequency on quartz. Black triangles are data from SWNTs on Si/SiO_2.

SWNT alignment direction are presumably polishing scratches – the vendor has indicated that the substrates have been polished with cerium oxide slurry with a polyurethane pad. While the polishing scratches are mostly parallel with each other and unidirectional at this magnification; their density, depth, and width appear to vary randomly. Comparison between the Raman G-band map and the AFM image reveals a striking correlation in the direction of the polishing scratch lines with the alignment of locations of ω_{G+} minima in the two neighboring SWNTs as indicated by the double-headed arrows. That is, the alignment of regions of minimum strain in the neighboring SWNTs coincides with the direction of polishing induced roughness. Based on this observation, we propose that the non-uniformity of compressive strain along the SWNT arises from variations in the interaction with the substrate due to the surface roughness caused mainly by polishing scratches. The random variations in ω_{G+} and in $d\omega_{G+}/dT$ along the length of a SWNT are then likely to be arising from the distributions of density, depth, and width of these scratches. While the strong interaction with the substrate and the large difference in CTE lead to compressive strain, these scratches create small "trenches" underneath the SWNTs that provide regions free of or at least reduced degree of strain.

We note that the widths of the polishing scratches are much smaller than our laser spot size of ~1 μm. Therefore, each Raman spectrum obtained here actually provides an average ω_{G+} value that reflects the density of these scratch lines on the substrate. That is, within the laser spot, some parts of the SWNT will be over the polishing scratches while other parts will not. This then implies that there are local regions where the compressive strain may be significantly larger than the maximum ~1% that we have estimated based

on the maximum ω_{G+} observed at room T.

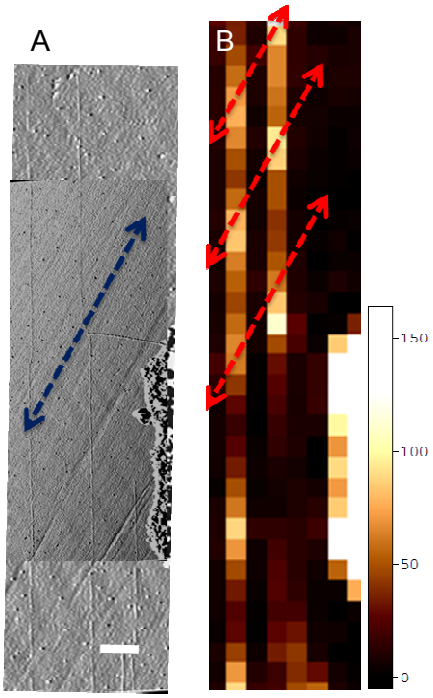

Figure 4.6: Side by side comparison of a composite AFM image (a) with Raman intensity map integrated between 1590-1600 cm^{-1} (a) of the same area showing SWNTs on single crystal quartz at room temperature. Scale bar of the AFM image corresponds to 1 μm. Raman map is at the same magnification. Intensity scale bar for the Raman map is shown on right of (a). The blue arrow in (b) indicates the direction of the polishing scratches. Three red arrows in (b) point in the same direction as the arrow in (a) and are placed over the bright spots in the Raman image indicating the alignment direction of low-strain points being coincidental with the polishing scratches.

4.6. Conclusions

We have shown that, on average, as-grown SWNTs horizontally aligned on single crystal quartz exhibit anomalously up-shifted G-band phonon energies. The magnitude of the up-shift can be as large as ~30 cm^{-1} and it is non-uniform along the length of SWNTs. The non-uniformity arises from the surface roughness of the polishing scratches. Comparison of T dependences of ω_{G+} of SWNTs grown on quartz and on Si/SiO_2 substrates has revealed that these unusual phonon frequencies are the consequences of

mechanical compression induced by the substrate. Strong interactions with the substrate that allows nearly perfect alignment when combined with a large difference in CTE leave the SWNTs under non-uniform but uniaxial compressive strain at room *T*. Given the mechanical strain has been shown to alter electronic band structure of SWNTs, whether substrate induced alignment effect the electrical properties of SWNTs becomes a question of practical interest. We will discuss the implications of the substrate induced strain on electrical performance of SWNT devices and effects of device fabrication steps on the substrate induced strain will be further discussed in the following chapter.

4.7. List of References

[1] R. Saito, G. Dresselhaus, and M. S. Dresselhaus, *Physical Properties of Carbon Nanotubes* (Imperial College Press, London, 1998), p. 259.

[2] R. H. Baughman, A. A. Zakhidov, and W. A. de Heer, Science **297**, 787 (2002).

[3] C. Kocabas, S. H. Hur, A. Gaur, M. A. Meitl, M. Shim, and J. A. Rogers, Small **1**, 1110 (2005).

[4] S. J. Kang, C. Kocabas, T. Ozel, M. Shim, N. Pimparkar, M. A. Alam, S. V. Rotkin, and J. A. Rogers, Nature Nanotechn. **2**, 230 (2007).

[5] S. Han, X. Liu, and C. Zhou, J. Am. Chem. Soc. **127**, 5294 (2005).

[6] A. Ismach, L. Segev, E. Wachtel, and E. Joselevich, Angew. Chem. Int. Ed. **43**, 6140 (2004).

[7] C. Kocabas, M. Shim, and J. A. Rogers, J. Am. Chem. Soc. **128**, 4540 (2006).

[8] N. Ishigami, H. Ago, K. Imamoto, M. Tsuji, K. Iakoubovskii, and N. Minami, J. Am. Chem. Soc. **130**, 9918 (2008).

[9] Q. Yu, G. Qin, H. Li, Z. Xia, Y. Nian, and S. S. Pei, J. Phys. Chem. B **110**, 22676 (2006).

[10] X. Liu, K. Ryu, A. Badmaev, S. Han, and C. Zhou, J. Phys. Chem. C **112**, 15929 (2008).

[11] R. J. Chen, N. R. Franklin, J. Kong, J. Cao, T. W. Tombler, Y. Zhang, and H. Dai, Appl. Phys. Lett. **79**, 2258 (2001).

[12] P. G. Collins, K. Bradley, M. Ishigami, and A. Zettl, Science **287**, 1801 (2000).

[13] G. Dukovic, B. E. White, Z. Zhou, F. Wang, S. Jockusch, M. L. Steigerwald, T. F. Heinz, R. A. Friesner, N. J. Turro, and L. E. Brus, J. Am. Chem. Soc. **126**, 15269 (2004).

[14] S. Heinze, J. Tersoff, R. Martel, V. Derycke, J. Appenzeller, and P. Avouris, Phys. Rev. Lett. **89**, 106801 (2002).

[15] S. Jhi, S. G. Louie, and M. L. Cohen, Phys. Rev. Lett. **85**, 1710 (2000).

[16] M. Shim, J. H. Back, T. Ozel, and K. W. Kwon, Phys. Rev. B **71**, 205411 (2005).

[17] M. Shim and G. P. Siddons, Appl. Phys. Lett. **83**, 3564 (2003).

[18] G. U. Sumanasekera, C. K. W. Adu, S. Fang, and P. C. Eklund, Phys. Rev. Lett. **85**, 1096 (2000).

[19] H. Ulbricht, G. Moos, and T. Hertel, Surf. Sci. **532-535**, 852 (2003).

[20] M. Shim, A. Gaur, K. T. Nguyen, D. Abdula, and T. Ozel, J. Phys. Chem. C **112**, 13017 (2008).

[21] C. Kocabas, S. J. Kang, T. Ozel, M. Shim, and J. A. Rogers, J. Phys. Chem. C **111**, 17879 (2007).

[22] A. Gaur and M. Shim, Phys. Rev. B **78**, 125422 (2008).

[23] L. Ding, A. Tselev, J. Wang, D. Yuan, H. Chu, T. P. McNicholas, Y. Li, and J. Liu, Nano Lett. **9**, 800 (2009).

[24] K. T. Nguyen, A. Gaur, and M. Shim, Phys. Rev. Lett. **98**, 145504 (2007).

[25] Y. Wu, J. Maultzsch, E. Knoesel, B. Chandra, M. Huang, M. Y. Sfeir, L. E. Brus, J. Hone, and T. F. Heinz, Phys. Rev. Lett. **99**, 027402 (2007).

[26] T. Ando, J. Am. Chem. Soc. **75**, 124701 (2006).

[27] H. Farhat, H. Son, G. G. Samsonidze, S. Reich, M. S. Dresselhaus, and J. Kong, Phys. Rev. Lett. **99**, 145506 (2007).

[28] N. Caudal, A. M. Saitta, M. Lazzeri, and F. Mauri, Phys. Rev. B **75**, 115423 (2007).

[29] S. Piscanec, M. Lazzeri, F. Mauri, A. C. Ferrari, and J. Robertson, Phys. Rev. Lett. **93**, 185503 (2004).

[30] Y. Zhang, J. Zhang, H. Son, J. Kong, and Z. Liu, J. Am. Chem. Soc. **127**, 17156 (2005).

[31] A. Jorio, A. G. Souza Filho, G. Dresselhaus*, et al*, Phys. Rev. B **65**, 155412 (2002).

[32] O. Dubay, G. Kresse, and H. Kuzmany, Phys. Rev. Lett. **88**, 235506 (2002).

[33] C. J. Wang, Q. Cao, T. Ozel, A. Gaur, J. A. Rogers, and M. Shim, J. Am. Chem. Soc. **127**, 11460 (2005).

[34] K. T. Nguyen and M. Shim, J. Am. Chem. Soc. **131**, 7103 (2009).

[35] A. M. Rao, P. C. Eklund, S. Bandow, A. Thess, and R. E. Smalley, Nature **388**, 257 (1997).

[36] M. Shim, T. Ozel, A. Gaur, and C. J. Wang, J. Am. Chem. Soc. **128**, 7522 (2006).

[37] J. C. Tsang, M. Freitag, V. Perebeinos, J. Liu, and P. Avouris, Nat. Nanotech. **2**, 725 (2007).

[38] S. B. Cronin, A. K. Swan, M. S. Unlu, B. B. Goldberg, M. S. Dresselhaus, and M. Tinkham, Phys. Rev. Lett. **93**, 167401 (2004).

[39] S. B. Cronin, A. K. Swan, M. S. Unlu, B. B. Goldberg, M. S. Dresselhaus, and M. Tinkham, Phys. Rev. B **72**, 035425 (2005).

[40] B. Gao, L. Jiang, X. Ling, J. Zhang, and Z. F. Liu, J. Phys. Chem. C **112**, 20123 (2008).

[41] T. W. Tombler, C. Zhou, L. Alexseyev, J. Kong, H. Dai, L. Liu, C. S. Jayanthi, M. Tang, and S. Y. Wu, Nature **405**, 769 (2000).

[42] E. D. Minot, Y. Yaish, V. Sazonova, J. Y. Park, M. Brink, and P. L. McEuen, Phys. Rev. Lett. **90**, 156401 (2003).

[43] W. Yang, R. Wang, and H. Yan, Phys. Rev. B **77**, 195440 (2008).

[44] M. S. Amer, M. M. El-Ashry, and J. F. Maguire, J. Chem. Phys. **121**, 2752 (2004).

[45] U. D. Venkateswaran, A. M. Rao, E. Richter, M. Menon, A. Rinzler, R. E. Smalley, and P. C. Eklund, Phys. Rev. B **59**, 10928 (1999).

[46] S. Lebedkin, K. Arnold, O. Kiowski, F. Hennrich, and M. M. Kappes, Phys. Rev. B **73**, 094109 (2006).

[47] H. D. Li, K. T. Yue, Z. L. Lian*, et al*, Appl. Phys. Lett. **76**, 2053 (2000).

[48] S. Chiashi, Y. Murakam, Y. Miyauchi, and S. Maruyama, Jpn. J. Appl. Phys. **47**, 2010 (2008).

[49] Q. Zhang, D. J. Yang, S. G. Wang, S. F. Yoon, and J. Ahn, Smart Mater. Struct. **15**, S1 (2006).

[50] Y. Y. Zhang, L. M. Xie, J. Zhang, Z. Y. Wu, and Z. F. Liu, J. Phys. Chem. C **111**, 14031 (2007).

[51] N. Bonini, M. Lazzeri, N. Marzari, and F. Mauri, Phys. Rev. Lett. **99**, 176802 (2007).

[52] N. R. Raravikar, P. Keblinski, A. M. Rao, M. S. Dresselhaus, L. S. Schadler, and P. M. Ajayan, Phys. Rev. B **66**, 235424 (2002).

[53] J. A.H., Proc. R. Soc. A **142**, 237 (1933).

[54] Joseph L. Rosenholtz, Dudley T. Smith, Am. Miner. **26**, 103 (1941).

[55] H. Jiang, B. Liu, Y. Huang, and K. C. Hwang, J. Eng. Mat. and Tech. **126**, 265 (2004).

CHAPTER 5

IMPLICATIONS OF THE SUBSTRATE INDUCED STRAIN ON THE ELECTRICAL PROPERTIES OF CARBON NANOTUBES

Significant components of this chapter was published as "Non-Uniform Compressive Strain in Horizontally Aligned Single-Walled Carbon Nanotubes Grown on Single Crystal Quartz", T. Ozel, D. Abdula, E. Hwang, and M. Shim, **ACS Nano, 3,** 2217 (2009).

5.1. Introduction

In the previous chapter, we have proposed that the interactions with the substrate that allow near perfect horizontal alignment in combination with large difference in the coefficients of thermal expansion may lead to uniaxial compressive strain along as-grown single-walled carbon nanotubes (SWNTs) on single crystal quartz substrates. The former discussion can be followed by an obvious question whether the aforementioned substrate induced uniaxial compression effects the electrical performance of SWNT electronic devices. In this chapter, we will initially discuss the possible effects of uniaxial mechanical strain on the electronic characteristics of horizontally aligned single-walled carbon nanotubes. We will discuss later whether the substrate induced uniaxial compression on aligned SWNTs can be maintained in SWNT electronic devices and the effects of device fabrication steps on electrical performance.

5.2. Effects of Strain on the Band-gap of Single-Walled Carbon Nanotubes

Earlier studies have shown that the electronic band gaps of SWNTs can be altered by mechanical stress.[1] The substrate-induced non-uniform uniaxial compression on as-grown SWNTs horizontally aligned on single crystal quartz substrates may then affect electrical characteristics of SWNT-based devices. On the contrary, transistors consisting of SWNTs grown on quartz exhibit performances comparable to those of SWNTs on Si/SiO_2 substrates.[2--6] For example, the inferred average per tube mobility of devices made of parallel arrays of thousands of SWNTs on quartz has been shown to be similar to the mobility of individual SWNTs on Si/SiO_2 substrates.[3] For a direct comparison, we

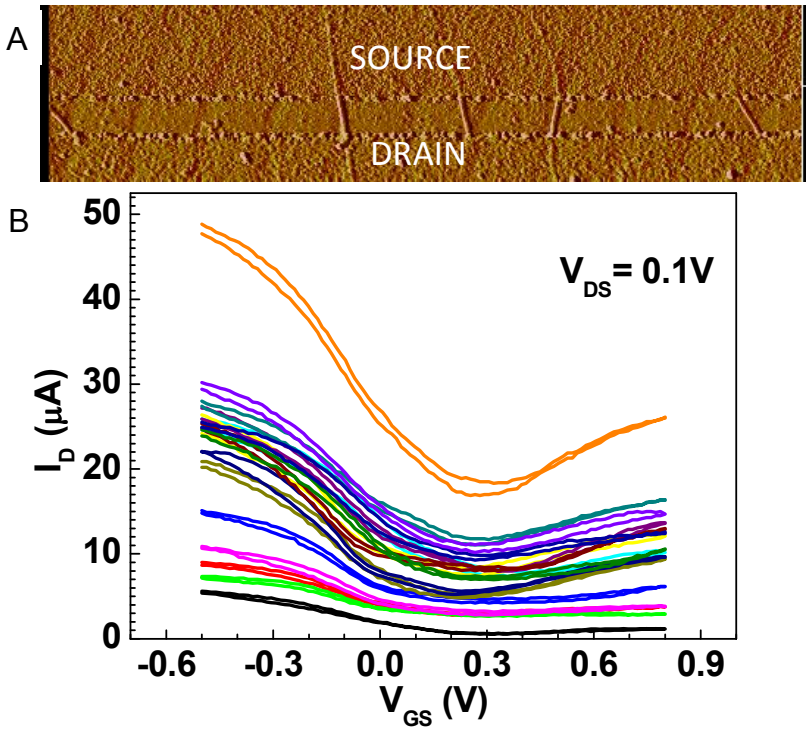

Figure 5.1: (a) AFM image of a part of a typical device fabricated on Si/SiO_2 substrate. The channel length is 500 nm. (b) Transfer curves for 16 SWNT FETs with channels of 500 nm in length and 200 μm in width on a Si/SiO_2 substrate.

have simultaneously fabricated short channel devices on arrays of SWNTs on single crystal quartz and Si/SiO_2 substrates. Figure 5.1 shows an AFM image of a fraction of a typical device channel on a Si/SiO_2 substrate and corresponding electrical measurements at room temperature by PEO electrolyte gating. We have chosen channel lengths to be 500 nm and SWNT density to be low enough that randomly grown SWNTs on Si/SiO_2 substrates do not cross one another in the channel for a direct comparison with aligned SWNT arrays on quartz. We have added up the transfer curves of 16 devices for both kinds of samples in order to minimize the uncertainty due to large device-to-device variations in electrical characteristics as observed in Figure 5.1(b). The results are displayed on Figure 5.2. The difference between threshold voltages is ~30 mV, which is not only less than the standard deviation of the presented data but also comparable to the uncertainty due to thermal fluctuations (~25 mV) at room temperature. We have not observed any measurable deviations in device performances due to substrate induced alignment of SWNTs on quartz at room temperature.

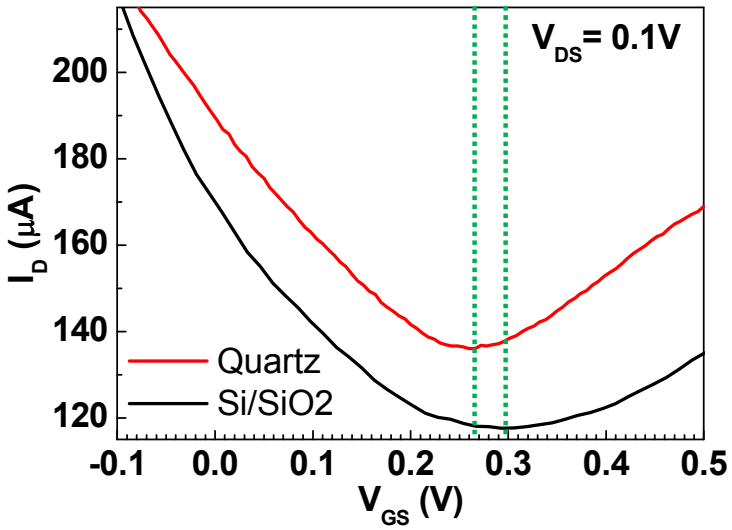

Figure 5.2: Sum over the 16 transfer curves shown on Figure 5.1(b) for devices on Si/SiO2 (black) and corresponding data for another set of 16 devices on quartz (red).

To assess the degree of effect on electron transport, strain induced band gap change is estimated. The sign and the magnitude of the change in the band gap, ΔE, due to uniaxial strain (ε) depend on the chiral angle (θ) following the simple relation:[1,7]

$$\frac{\Delta E}{\varepsilon} \cong 0.57 \times 3t_0 \,\mathrm{sgn}(2p+1)(1+\nu)\cos(3\theta) \qquad \text{Eq. 5.1}$$

This equation assumes the lattice to act as an elastic medium with Poisson ratio ν, t_0 is the graphene tight-binding overlap integral for the nearest π-bonds, and the factor p is either 0 (metallic) or ± 1 (semiconducting) so that $(n-m-p)$ is a factor of 3 for a SWNT with *(n, m)* chiral index.[7, 8] Figure 5.3 shows the change in the band-gap due to uniaxial strain as a function of the SWNT diameter following equation 5.1. Roughly the same percentage of SWNTs will have widening of the gap as those that have gap closing. The magnitudes of changes in the band gaps are also expected to be relatively small – most are within ~100 meV range for 2% uniaxial strain.[7] Therefore, the net effect of compressive strain due to the substrate in devices consisting of large number of SWNTs in parallel arrays is expected to be negligible at room temperature. This statement is also in agreement with our experimental results. In individual SWNT devices, on the other hand, there may be significant differences for certain chiralities. However, it is difficult to quantify differences in the electrical properties of individual SWNT transistors fabricated on quartz vs. on Si/SiO_2 substrates due to large device-to-device variations (e.g. contact resistance variations, different degree of disorder etc.).[9--13] On the other hand, further analysis is needed to figure out whether the substrate induced uniaxial compression observed for as-grown aligned SWNTs can be conserved after standard lithography and

other device fabrication steps.

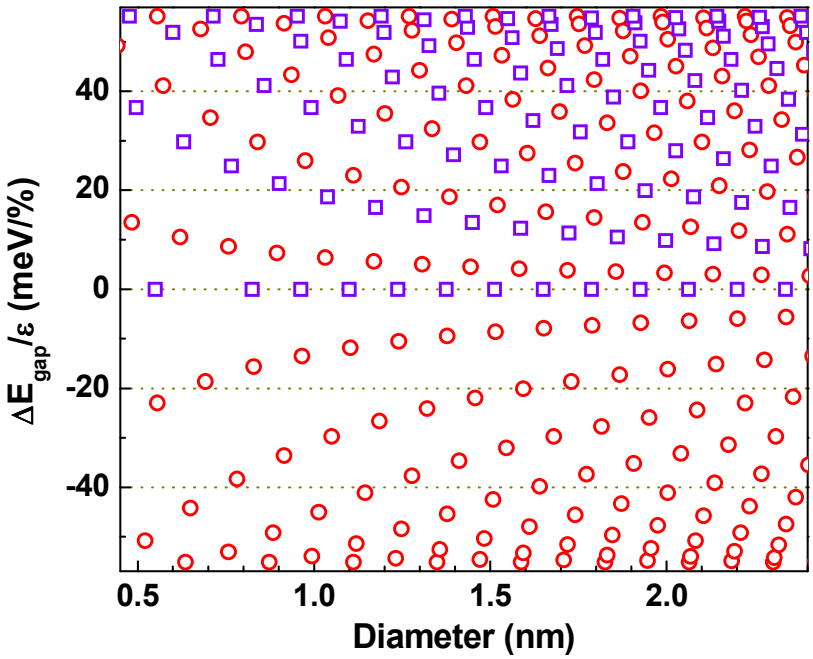

Figure 5.3: The change in the energy band-gap per percent uniaxial strain within the typical diameter range. Red circles indicate semiconducting SWNTs and blue squares indicate metallic SWNTs.

5.3. Substrate Induced Compressive Strain & Device Fabrication

5.3.1. Statistical Comparison of as-Grown and Micro-Fabricated Carbon Nanotubes: A Raman Study

While we have not observed any qualitative or quantitative differences in the electrical properties of individual SWNT transistors fabricated on quartz vs. on Si/SiO_2 substrates at room temperature, our Raman studies suggest that such differences should not even be expected at low temperatures.[14] Figure 5.4 shows that the average G^+-band frequency, ω_{G+}, down-shifts from 1603 cm^{-1} to 1591 cm^{-1} upon photolithography and metallization. The right inset in Fig 5.4 shows ω_{G+} along the length of two different

semiconducting SWNTs after device fabrication steps. While some of the fluctuations in ω_{G+} remain, the standard deviations are less than 1.5 cm^{-1} and the actual ω_{G+} vales are now much closer to the expected range of 1590 – 1595 cm^{-1} for the unstrained semiconducting SWNTs. These results indicate that most of the compressive strain due to the quartz substrate is relieved during device fabrication steps.

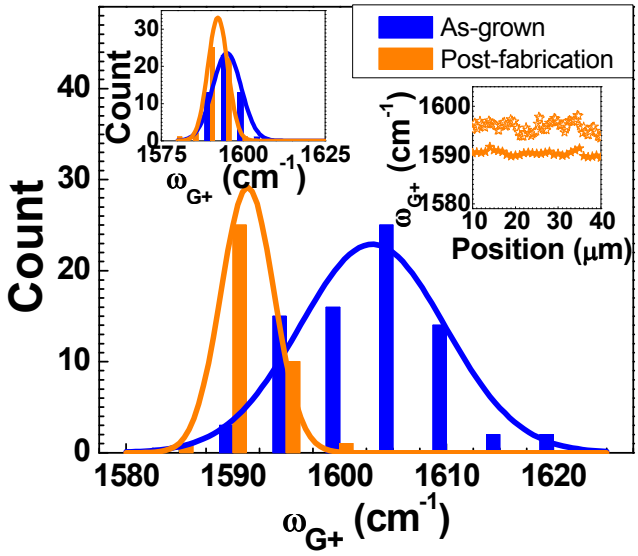

Figure 5.4: Distribution of Raman G^+ peak frequencies of as-grown SWNTs on single crystal quartz substrates before (blue) and after (orange) device fabrication. The upper left inset displays the same comparison for SWNTs on Si/SiO_2 substrates. The right inset shows the spatial profile of Raman G+ frequency along the length of two different SWNTs on quartz substrates after device fabrication.

We note that the average ω_{G+} of SWNTs on Si/SiO_2 substrates also down-shifts after device fabrication steps. Upper left inset of Figure 5.4 shows that SWNTs grown on Si/SiO_2 substrates also exhibit a down-shift from 1595 to 1592 cm^{-1} upon lithography and metallization. While the magnitude of this down-shift is smaller, it may not be negligible. We suspect that a combination of changes in doping level and in defects may be responsible for the down-shift in these unstrained SWNTs.

5.3.2. Effects of Solvent Exposure on the Substrate Induced Compression

Realizing observed uniaxial compression on aligned SWNTs grown on single crystal quartz is released after device fabrication, we will now try to understand which step or steps during micro-fabrication are responsible for the release of the substrate induced mechanical strain. Typical lithography steps expose SWNTs to water and alcohol based solvents, and metallization steps are realized in vacuum chambers, where the bulk metal electrodes come into mechanical contact with SWNTs. We believe the substrate induced mechanical strain on aligned SWNTs is released once SWNTs are exposed to certain solvents. In order to elucidate the effects of solvent exposure on the substrate induced compression, we have compared the Raman spectra of aligned SWNTs before, during and after exposing SWNTs to distilled (DI) water and isopropyl alcohol (IPA).

Figure 5.5 compares the effect of solvent exposure on the substrate induced compression on aligned SWNTs for DI water and IPA. As we have shown earlier the ω_{G+} is blue-shifted for as-grown aligned SWNTs due to substrate induced compression. The Raman spectra for two different aligned SWNTs, which are compressed along the length, are examined in Figure 5.5. Raman spectra for SWNTs have been collected after SWNTs were rinsed by solvents and dried by N_2 flow. We have initially exposed our samples to DI water. The G-band spectrum does not differ significantly after rinsing with DI water as shown in Figure 5.5. Once the same samples have been rinsed by IPA and dried by N_2 flow, the G-band Raman spectra red-shifts back to ~ 1590 cm^{-1} without any increase in the D-band intensity, indicating the uniaxial compression is relieved. Our results are in agreement with the reported results for monolayer graphene samples.[15] Xie et al. have

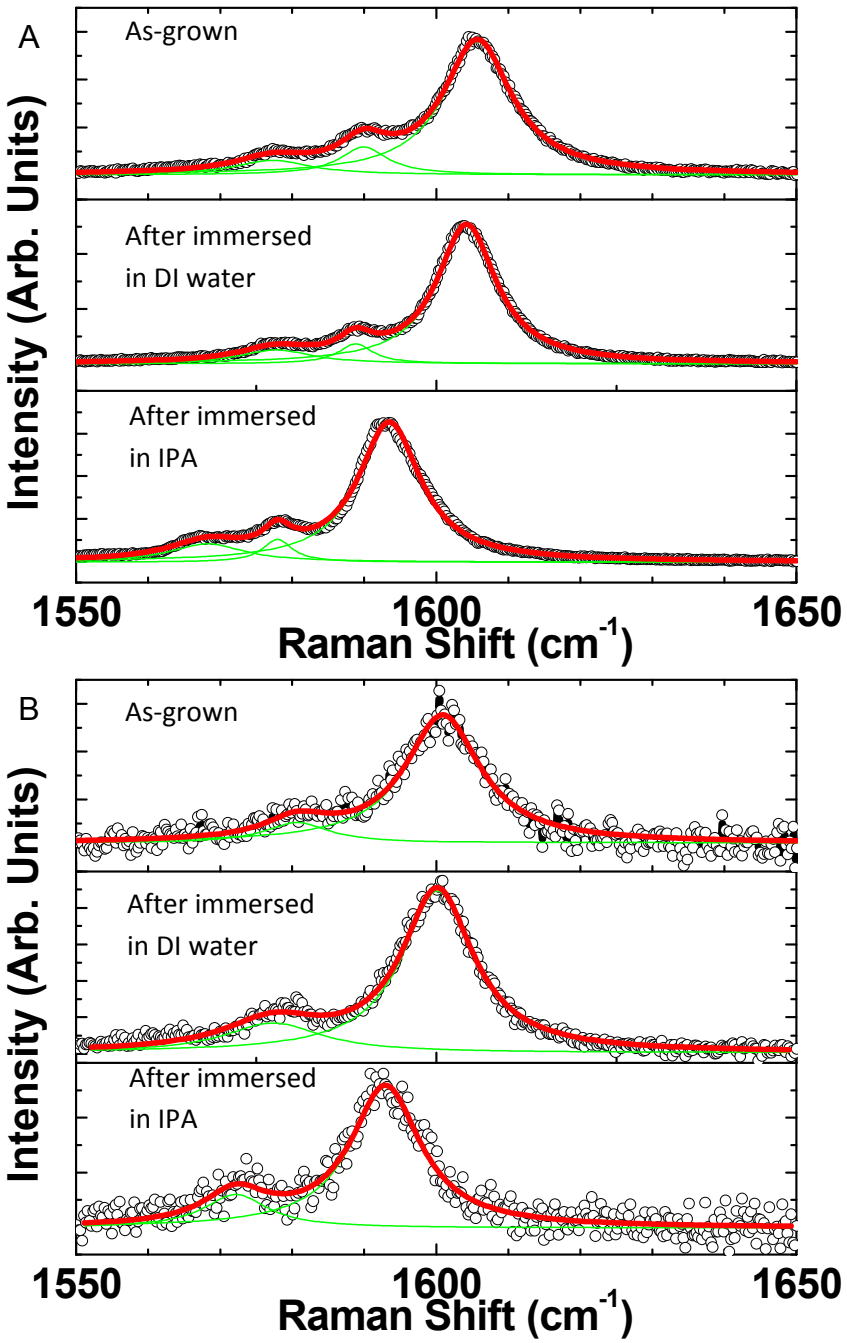

Figure 5.5: (a) Background subtracted G-band Raman spectra (black circles) of a SWNT after growth (top), after immersed in DI water (middle), and after immersed in IPA (bottom). The data were fit to multiple Lorentzian peaks. The green dotted lines are individual Lorentzian peaks and the red lines are the overall fits. (b) The same set of data collected on another SWNT. Very small D-band was observed for the SWNT in (a). No significant change in the D-band was observed after the SWNT was immersed in solvents. No D-band was observed for the SWNT in (b).

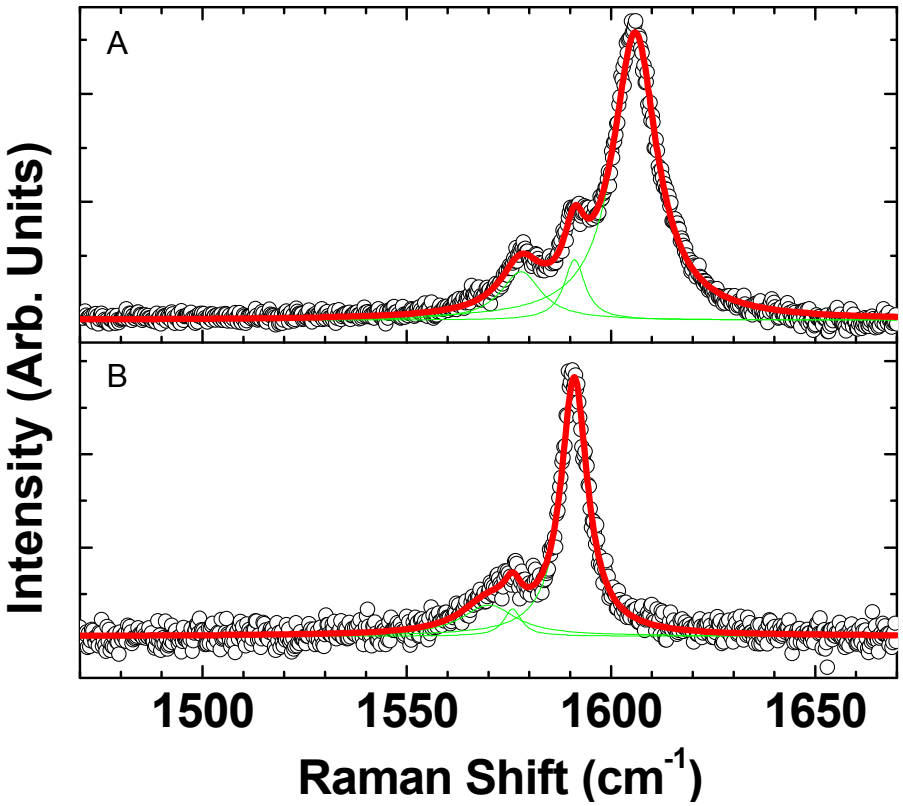

Figure 5.6: (a) G-band Raman spectrum of an as-grown aligned SWNT collected in air. (b) Corresponding data for the same SWNT in IPA.

shown that fragments of monolayer graphene samples are detached from underlying SiO_2 surface once exposed to IPA but no fragments of graphene samples are detached from the oxide surface after exposed to DI water.[15] It is possible that substrate induced uniaxial compression on the SWNTs is released when IPA wets the surface and fractions of the SWNT is detached from the surface momentarily as it happens with the graphene samples. Another possibility is that the substrate induced compression is mechanically released as IPA evaporates off the surface. In order to distinguish between these two scenarios, we have sandwiched a layer of IPA between the quartz substrate on which aligned SWNTs are grown and a cover slip so that IPA does not evaporate before we collect the Raman spectra. Figure 5.6 compares the G-band Raman spectra of a SWNT

as-grown in air and immersed in IPA. The G-band Raman spectrum is red-shifted back to ~ 1590 cm^{-1}, which means that the substrate induced compression is released before IPA is dried. Therefore, the compression may be released by the initial wetting of IPA.

5.4. Conclusions

As-grown strained SWNTs on single crystal quartz allow effects of difficult-to-achieve uniaxial compressive stress to be experimentally examined. Our results open up the possibility of comparing metallic vs. semiconducting SWNTs' responses and verification of chirality dependent responses to uniaxial compressive stress. We have also shown that typical device fabrication steps and exposure to IPA based solvents relieve the compressive strain in horizontally aligned SWNTs. Therefore the resulting electrical characteristics for horizontally aligned SWNTs grown on single crystal quartz substrates are expected and are observed to be similar to SWNTs grown on Si/SiO_2 substrates.

5.5. List of References

[1] E. D. Minot, Y. Yaish, V. Sazonova, J. Y. Park, M. Brink, and P. L. McEuen, Phys. Rev. Lett. **90**, 156401 (2003).

[2] C. Kocabas, S. H. Hur, A. Gaur, M. A. Meitl, M. Shim, and J. A. Rogers, Small **1**, 1110 (2005).

[3] S. J. Kang, C. Kocabas, T. Ozel, M. Shim, N. Pimparkar, M. A. Alam, S. V. Rotkin, and J. A. Rogers, Nat. Nanotech. **2**, 230 (2007).

[4] C. Kocabas, S. J. Kang, T. Ozel, M. Shim, and J. A. Rogers, J. Phys. Chem. C **111**, 17879 (2007).

[5] C. Kocabas, M. Shim, and J. A. Rogers, J. Am. Chem. Soc. **128**, 4540 (2006).

[6] C. Kocabas, N. Pimparkar, O. Yesilyurt, S. J. Kang, M. A. Alam, and J. A. Rogers, Nano Lett. **7**, 1195 (2007).

[7] M. Y. Huang, Y. Wu, B. Chandra, H. Yan, Y. Shan, T. F. Heinz, and J. Hone, Phys. Rev. Lett. **100**, 136803 (2008).

[8] R. Saito, G. Dresselhaus, and M. S. Dresselhaus, *Physical Properties of Carbon Nanotubes* (Imperial College Press, London, 1998).

[9] T. Ozel, A. Gaur, J. A. Rogers, and M. Shim, Nano Lett. **5**, 905 (2005).

[10] M. Shim, J. H. Back, T. Ozel, and K. W. Kwon, Phys. Rev. B **71**, 205411 (2005).

[11] M. Shim, Mater. Matters **2**, 16 (2007).

[12] M. Shim, A. Gaur, K. T. Nguyen, D. Abdula, and T. Ozel, J. Phys. Chem. C **112**, 13017 (2008).

[13] K. T. Nguyen and M. Shim, J. Am. Chem. Soc. **131**, 7103 (2009).

[14] T. Ozel, D. Abdula, E. Hwang, and M. Shim, ACS Nano **3**, 2217 (2009).

[15] X. Xie, L. Ju, X. Feng, Y. Sun, R. Zhou, K. Liu, S. Fan, Q. Li, and K. Jiang, Nano Lett. **9**, 2565 (2009).

CHAPTER 6

COMPLEX ARCHITECTURES OF CARBON NANOTUBE ARRAYS AND FUTURE APPLICATIONS

6.1. Introduction

In this chapter, I discuss architectures of carbon nanotubes for future electronic applications. Easy alignment and patterning of SWNTs by substrate template alignment and transfer printing combined with the exceptional electronic properties of SWNTs offer new directions for SWNT electronics. I will initially discuss the promise of substrate induced horizontal alignment for scalable patterning of SWNT electronic devices. Then I will move our discussion a step forward and evaluate the promise of transfer-printed multiple layers of aligned SWNT arrays as active electronic materials for molecular level memory devices.

6.2. Controllable Placement of Carbon Nanotubes on Substrates

I have already argued that both individual single-walled carbon nanotubes (SWNTs) and arrays of SWNTs are high-performance electronic materials to extend the capabilities of current and developing areas electronics. Proof-of-concept devices such as field effect transistors (FETs), logic circuits, sensors and ring oscillators have already been made on individual carbon nanotubes.[1] However, there remain many technical

challenges to overcome for integrating SWNTs into high performance microelectronic devices.[1] Besides the chirality distribution of SWNTs, the device characteristics are also altered by extreme sensitivity of the SWNT FETs to the local environment and even to fabrication processes. Researchers have recently reported techniques to disperse SWNTs with narrow chirality distributions in solution.[2--4] Another approach to overcome the uncontrolled the electronic variety in SWNTs has been selective chemical functionalization of SWNT arrays to eliminate metallic tubes, however scalability and reproducibility has been a significant issue with electronically selective chemical functionalization.[5] In order to reduce the dependence of device characteristics on the changes in the local environment, thin polymer and/or polymer electrolyte films have been used to isolate SWNTs and the contacts from the ambient as discussed in Chapter 2.[6--8]

Another critical technical challenge to be addressed is the alignment and patterning of SWNTs for scalable device fabrication.[1] Two recently reported methods are arguably the best efforts for controlled patterning of SWNTs. Carbon nanotubes dispersed in solutions have been shown to be successfully patterned between metal electrodes by radio frequency dielectrophoresis.[9] Even though this method is successful to limit the number of SWNTs in the channel, it is limited by poor metal-nanotube contacts and the low performance of solution processed nanotubes. On the other hand, near perfect horizontal alignment on crystalline substrates is another important advancement that has been made towards patterning and aligning pristine SWNTs.[10--13] In this section, I will suggest a number of easy-to-apply techniques for the realization

of scalable arrays of SWNT devices by taking advantage of horizontally aligned arrays of SWNTs grown on single crystal quartz substrates.

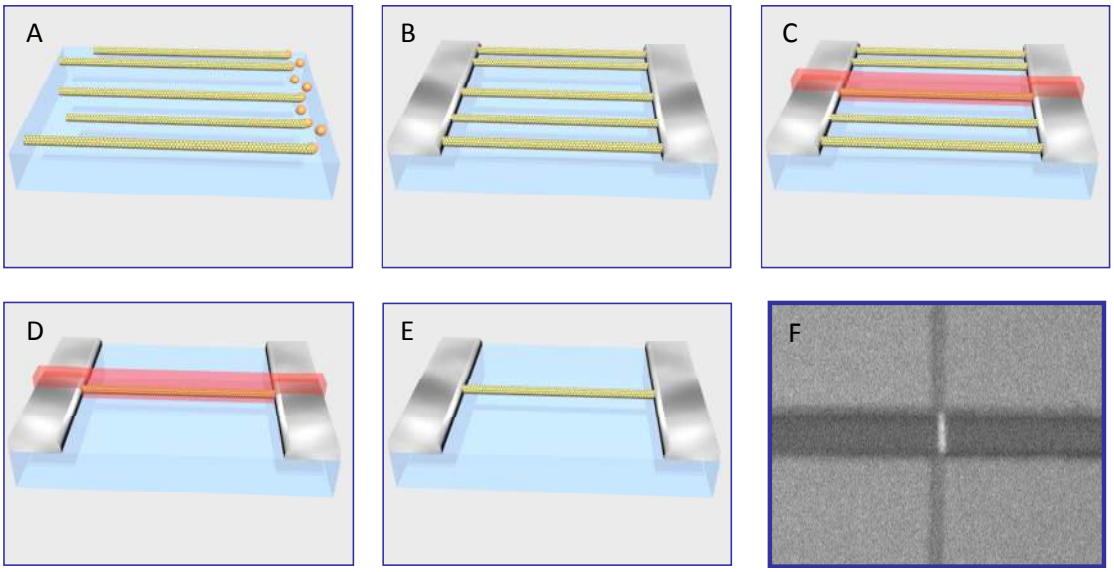

Figure 6.1: Schematics of the microfabrication steps for single connection SWNT FET. (a) Horizontally aligned SWNTs are grown from the patterned catalyst lines on ST-cut quartz. SWNTs may be either kept on the original substrate or transferred on another substrate. (b) Metal electrodes are evaporated on aligned arrays of SWNTs. (c) A very thin line of photoresist material is patterned in the channel so that only one SWNT is covered by the photoresist. (d) The device is kept in O_2 plasma for 30 seconds so that all uncovered SWNTs are etched. (e) The photoresist is lift-off by acetone rinsing. (f) An exemplary SEM image of a single connection SWNT FET. All patterns were realized by photolithography.

Here I will offer three techniques to realize arrays of SWNT FETs which include one or a few SWNTs in the channel by taking advantage of substrate template alignment during CVD growth. Figure 6.1 shows the critical steps for the first technique. Briefly, we have grown aligned SWNTs following our previous works. Catalyst lines are patterned on pre-annealed ST-cut quartz substrates and an ultra thin and fragmented layer of Fe is e-beam evaporated as the catalyst as discussed in chapter 4. SWNTs are grown from the catalyst lines by thermal CVD as depicted in Figure 6.1(a) and shown in Figure 3.7(a). The CVD grown arrays of aligned SWNTs can either be left on the quartz

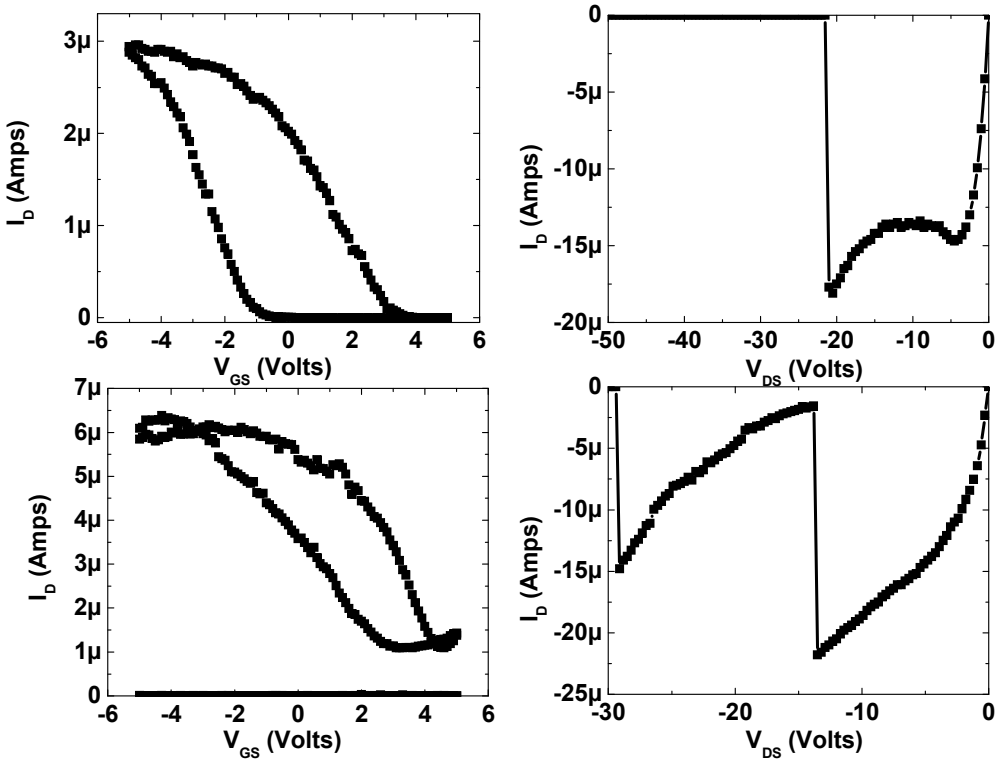

Figure 6.2: (a) The transfer curve of a SWNT FET with a semiconducting SWNT in the channel. (b) The electrical breakdown of the SWNT in (a) at a high source-drain bias. (c) The transfer curve of a SWNT FET with a semiconducting and a metallic SWNT in the channel. (d) The electrical breakdown of the SWNT in (a) at a high source-drain bias.

substrate or they can be transferred onto another substrate following Kang et al.[13,14] depending on the demands of the application. There are two ways to fabricate single connection devices after this step. You either pattern wide electrodes and etch extra SWNTs or pattern narrow electrodes and isolate the neighboring devices. For the latter one, we simply pattern metal electrodes on top of SWNT arrays and etch the SWNTs by O_2 plasma everywhere in the channel except a very thin stripe as depicted in Figure 6.1. The width of this stripe, i.e. the width of the not-etched part of the channel, can be chosen to be close to the average nanotube-to-nanotube distance in order to increasing the statistical chance of ending up with a single SWNT in the channel as the statistical details

will be discussed later.

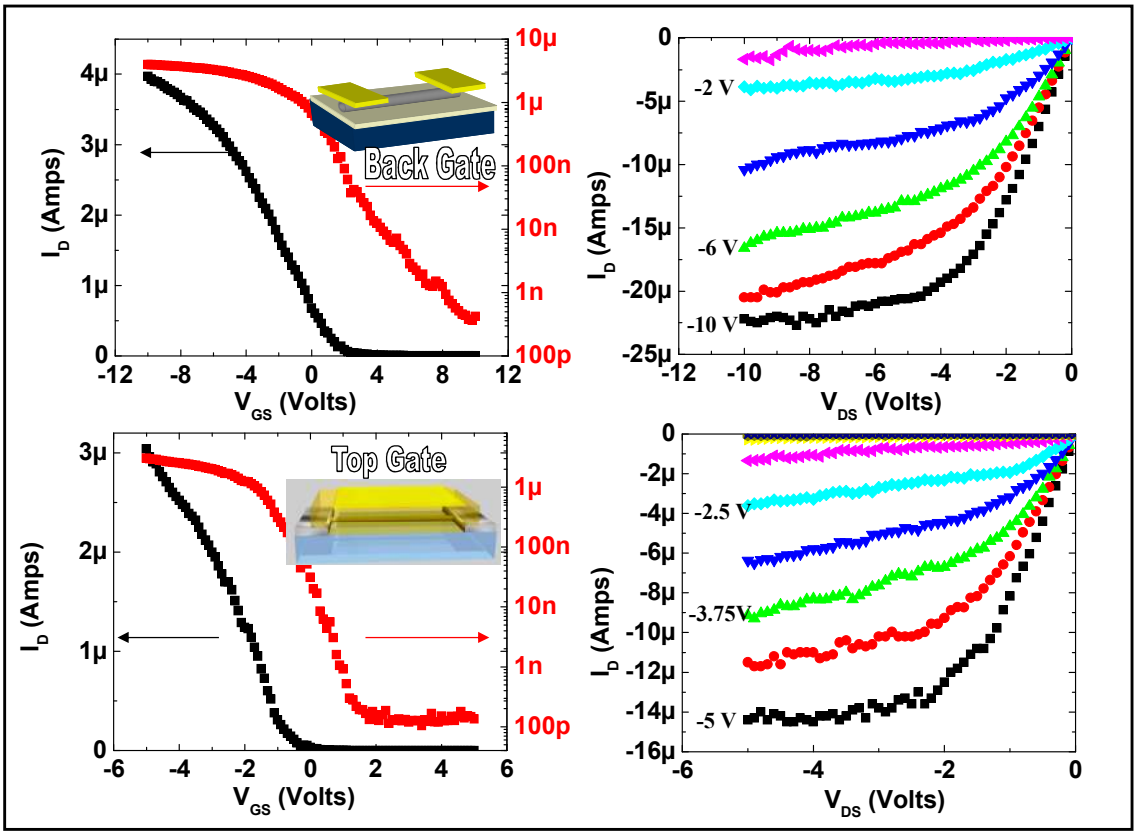

Figure 6.3: (a) Transfer curve plotted both in linear and semi-log scales for a single connection SWNT FET fabricated from aligned arrays of SWNTs transferred on a Si/SiO_2 (100 nm thermal oxide) substrate. (b) Corresponding output curves for the device in (a). (c) Same measurement as in (a) on a single connection SWNT FET fabricated on ST-cut quartz. (d) Corresponding output curves for the device in (c).

In order to test the device performance of arrays of single connection SWNT FETs fabricated by the method mentioned above, we have measured both top-gated (on quartz substrates) and back-gated (on Si/SiO_2 substrates) devices on quartz. As a top-gate dielectric we have spin-coated a film layer of hydrogen silsesquioxane (HSQ) and deposited 15 nm of HfO_2. The reason why we have chosen HSQ / HfO_2 gate dielectric over polymer electrolytes is to simply take advantage of the porous structure of the HSQ so that we can electrically burn the SWNTs in the channel to make sure there is only one

SWNT that spans the channel after measuring the device.[15] Electrical burning is not possible with polymer electrolyte gating due to since polymer may breakdown may occur before SWNTs are burnt. Figure 6.2 illustrates the electrical breakdown (burning) of SWNTs in the channel of an FET. The sharp decreases in the current in Figs. 6.2(b) and 6.2(d) indicates the electrical breakdown of SWNTs. The sudden increase in the current right before semiconducting SWNT is burned as shown in Figure 6.2(b) has been recently explained by the avalanche generation of free electrons and holes.[16]

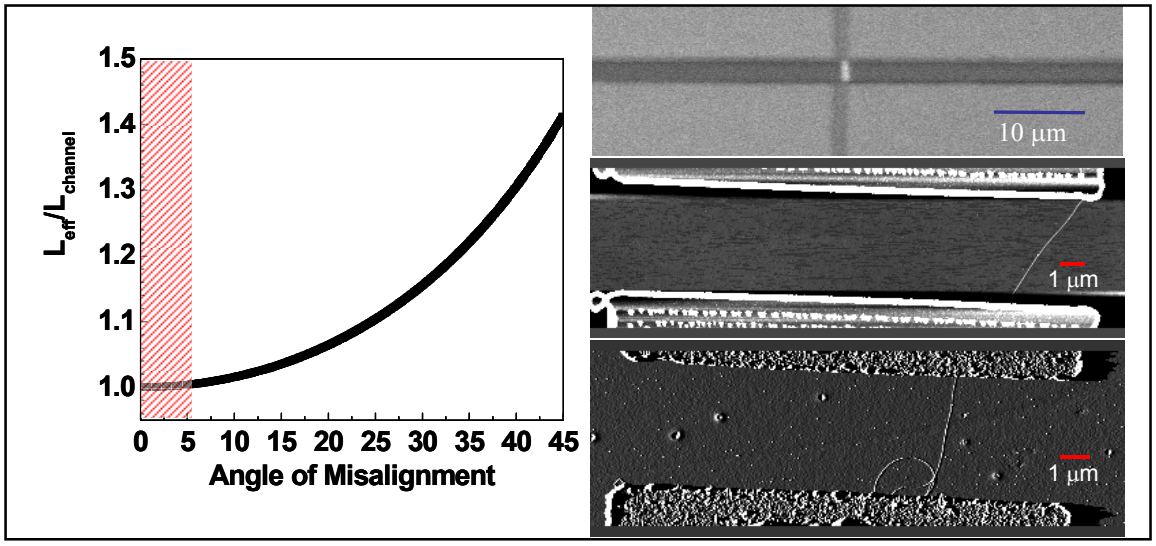

Figure 6.4: (a) A simple trigonometric relation between the fabricated channel length and the effective channel length (length of the SWNT in the channel) for a device with a linear SWNT in the channel. (b) An SEM image of a single connection device fabricated on an aligned SWNT. (c&d) AFM images of single connection devices with an almost linear but misaligned SWNT (a), and a non-linear SWNT.

High DC performance is achieved for both back-gated and top-gated devices as examples of the transfer and the output curves of such devices are shown in Figure 6.3. A certain advantage of these devices is the lack of curvature induced defects on the carbon nanotubes due to the linearity of the as grown nanotubes and the accurate assignment on the effective channel length due to the alignment besides the easiness in the maintaining

large number of FETs with single nanotube in the channel. Figure 6.4 compares single connection devices fabricated on aligned and randomly grown SWNTs and shows the discrepancy between the fabricated channel length and the effective channel length of misaligned SWNT FETs.

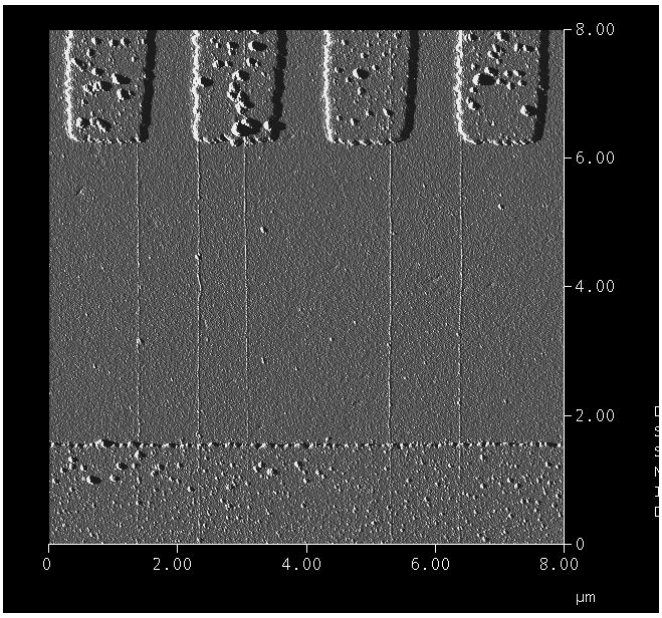

Figure 6.5: AFM image of a set of four devices. Three of them have a single SWNT and the other has two SWNTs bridging the device gap. All the devices have a common drain electrode and no plasma etching was necessary in the channel since the width of the source electrodes is close to the average nanotube-to-nanotube spacing. The electrodes were patterned by e-beam lithography.

AFM image in Figure 6.5 shows an array of SWNT devices fabricated by an alternative approach. This method simply requires patterning a packed set of narrow electrodes, which are as narrow as the average distance between two neighboring nanotubes. The critical step with this method is to isolate the packed set of channels in order to avoid device-to-device interconnects. This method follows the same statistics as the previous one, but the latter one produced not only cleaner channels but also offers to

pack more devices per unit area.

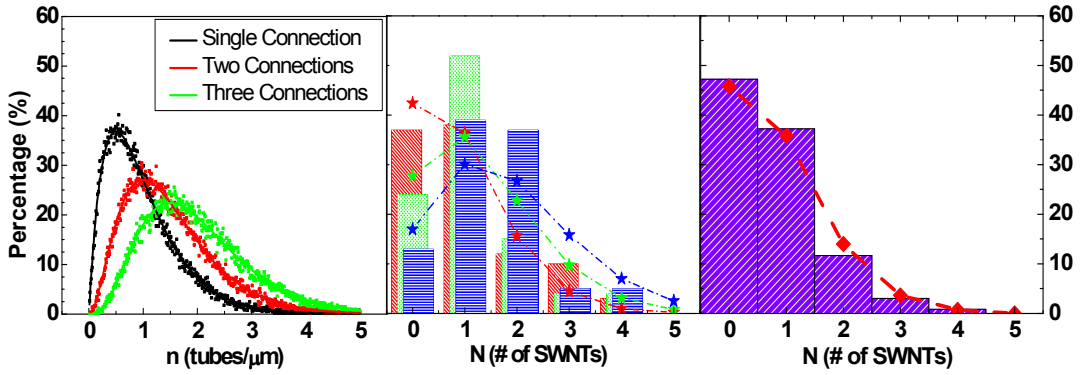

Figure 6.6: (a) Calculated percent probability of having single (black), two (red) and three (green) SWNTs connecting the source and drain electrodes by Monte Carlo simulations (scattered dots) and Poisson distribution (lines). The effective width was taken as 500 nm for the calculations. (b) Percentage of devices (bar columns) with N number of SWNTs in the channel. The data were collected by electrical burning and SEM imaging for devices fabricated by the first method on three different chips with different yields of SWNT density (n). Fits to Eq. 6.1 are also plotted (stars and segmented lines). The only fitting parameter is n, and it was estimated to be 0.43, 0 .64 and 0.89 tubes/μm for those three different chips. (c) Percentage of devices (bar columns) with N number of SWNTs in the channel. The data were collected from SEM images of devices fabricated by the second method. Fits to Eq. 6.1 are also plotted (diamonds and segmented lines). The fitting parameter n is 0.78 tubes/μm, which is in agreement with large area SEM images.

Being able to fabricate high performance single connection devices, I will now discuss the statistics for the number of nanotubes spanning the channel in the SWNT FETs and how can control the number of SWNTs in the channel. Figure 6.6(a) predicts the probability of getting one, two and three SWNTs spanning the channel of our devices as the nanotube density on the substrate varies. The simple Monte Carlo modeling applies to both of the suggested methods, and fits very well to Poisson distribution as expected. The Monte Carlo model assumes the nearest possible distance between two nanotubes to be 10 nm, which is in agreement with current observations,[17] and the probability of nanotube growth is uniform along the catalyst. Therefore, the probability (P) of getting N

nanotubes in the channel of effective width of w on a substrate which has n tubes per unit length is:

$$P = \frac{e^{-n \cdot w} \cdot (n \cdot w)^N}{N!}. \qquad \text{Eq. 1}$$

The effective width is the width of the line patterns which are not etched for devices fabricated following the first method (Figure 6.1), or the width of the electrodes for devices fabricated following the second method (Figure 6.5). From Eq. 6.1, I conclude that we expect higher yield of single connection devices as we pattern effective width to be closer to the reciprocal of the tube density per unit length.

Having estimated the relationship between the number of nanotube connections and the nanotube density, I will now compare our experimental results with our theoretical expectations. Figure 6.6(b) plots the percentage of the occurrence of devices with varying numbers of connections (0 to 5 nanotubes), which has been determined by etching all the nanotubes in the channel except a region defined by a 2 μm line. The different colored and patterned bars are from three different substrates with different nanotube densities in the 0.4 to 1 tubes/μm range. The data were collected from electrical burning and complimentary SEM imaging data from 178 measured devices. The plotted histograms were fit by Eq. 6.1. The fit parameters for n are 0.43, 0.64 and 0.89 tubes/μm for an effective width of 2 μm. As the density increases the peak of the histograms are shifted to the right, the number of not-connected devices decreases and the width of the distribution increases, as expected. We have repeated a similar experiment with devices for which we patterned electrodes which are 1 μm in width (second method). We have

not etched any nanotubes in the channel region of these devices as discussed earlier. We have imaged 231 samples with SEM on the same substrate. The plotted histogram fits precisely to the expected Poisson distribution given in Eq. 6.1 with fitting parameter n = 0.78 tubes/μm. For this sample, we have obtained ~37% single-connection, ~12% double-connection and ~3% three-connection devices for this sample.

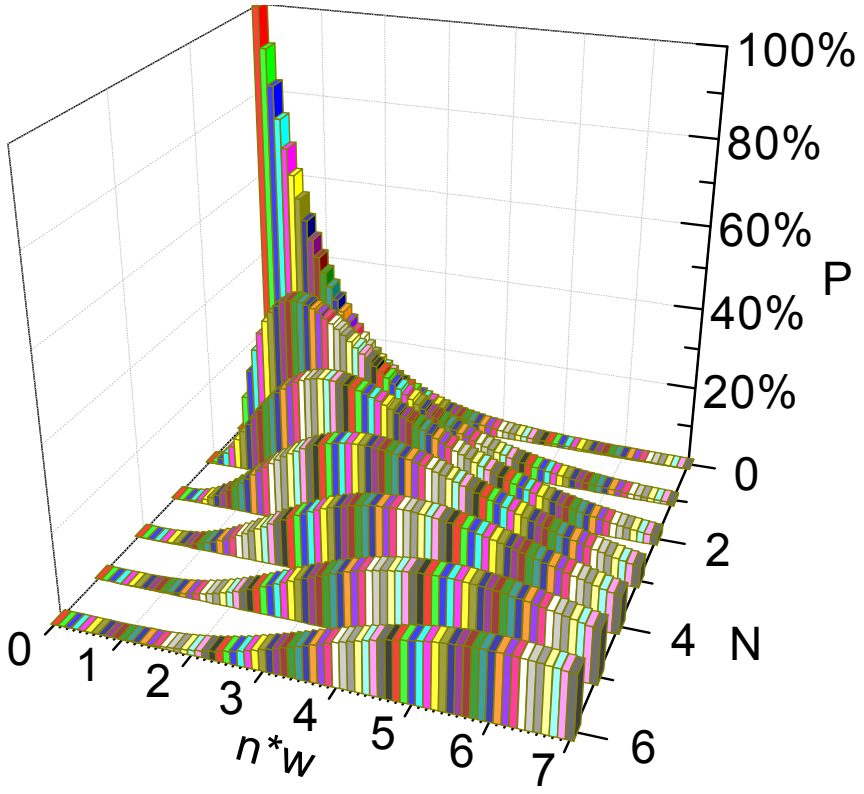

Figure 6.7: The probability of getting a fixed number of SWNT connections (N) as a function of the geometry independent parameter $n \times w$, i.e. number per unit length yield of SWNTs times the effective width.

Figure 6.7 summarizes our findings on the statistical chance on getting devices with a fixed number of SWNT connections. As seen in Figure 6.7, the statistical chance of getting a single SWNT connection is limited by ~ 37% ($1/e$). 37% is much better than the 8% we get for randomly grown SWNTs, and there exists a need for a better yield of

single connection devices for a realistic integration of SWNTs into microelectronics.

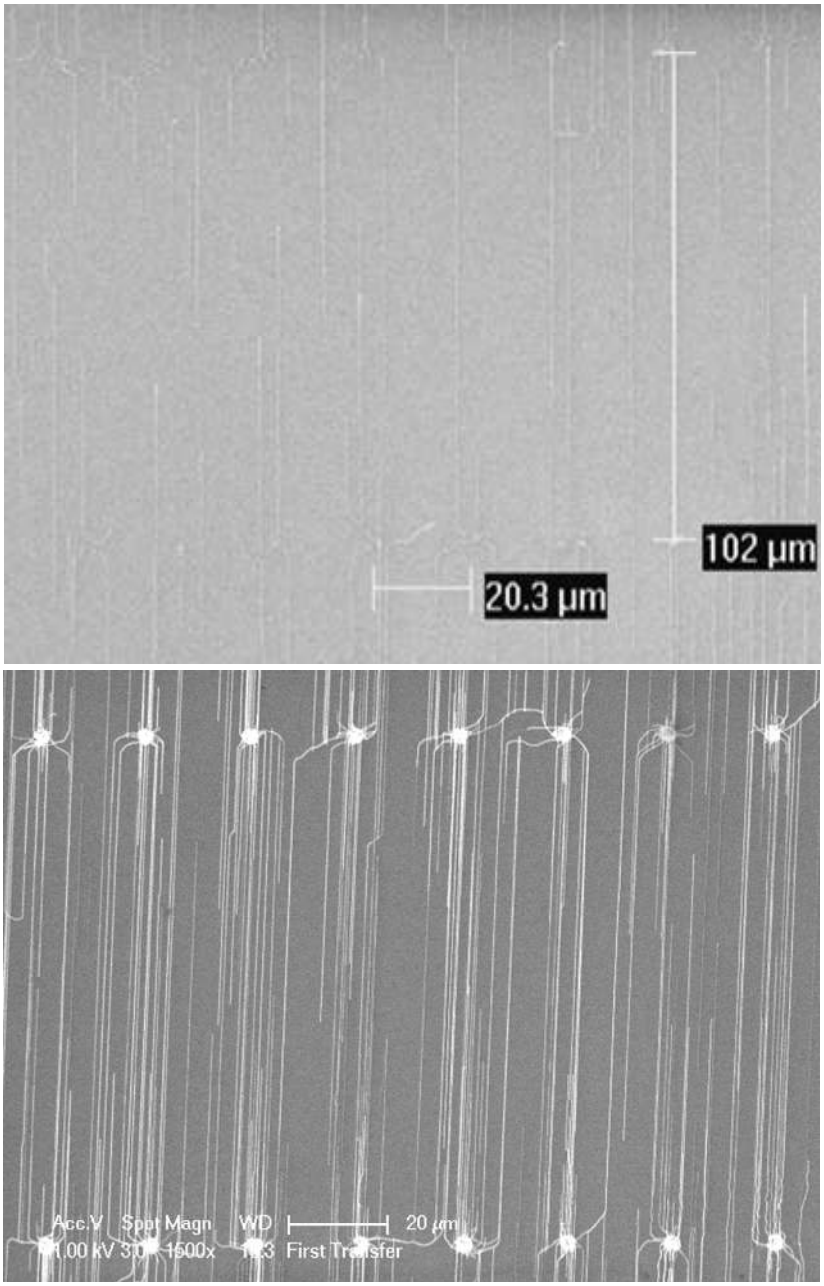

Figure 6.8: SEM images of two samples with different catalyst widths (2 and 4 µm) and SWNT yields. Aligned SWNTs were grown on ST-cut quartz and transferred onto Si/SiO_2 substrates.

Here, I offer another method to fabricate arrays of single connection SWNT devices by limiting the size of the catalyst patterns prior to CVD growth so that

statistically only one SWNT grows from each catalyst island. Figure 6.8 shows different yields of SWNTs grown from different sizes of catalyst islands. As of now this method obeys the same statistics with the previously mentioned techniques shown in Figure 6.7, where the effective width is the width of the catalyst islands. However this method can potentially be improved for better statistics if it can be integrated with more sophisticated patterning methods, which can successfully pattern individual catalyst particles rather than bulk catalyst islands.[18]

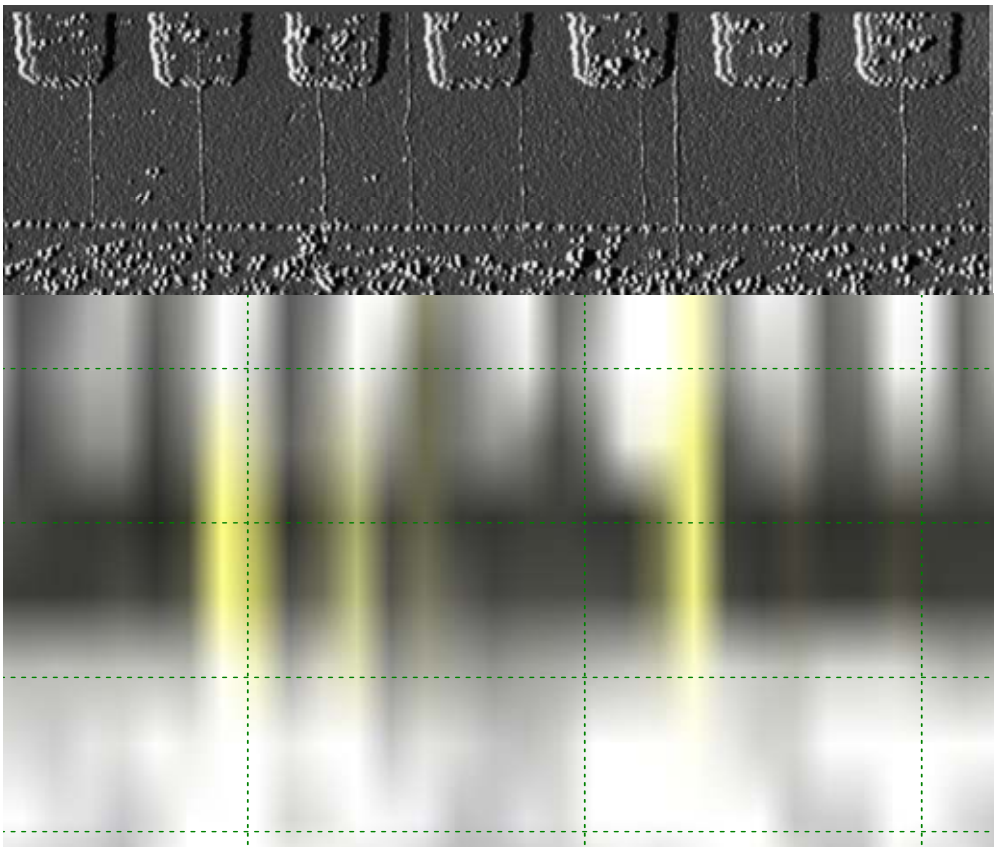

Figure 6.9: (a) AFM image of seven consecutive devices which all have single SWNT connections and a common drain electrode. The width of the electrodes is 1 μm. (b) Corresponding Raman map collected around 1590 cm^{-1}.

Having fabricated large arrays of single connection SWNT FETs and analyzing the capabilities and limitations of our methods, we are ready to offer our method as a tool

to question a scientific problem. The as-grown nanotubes have inhomogeneous electronic properties due to different chirality of the nanotubes. One question of interest would be to correlate device performance with the Raman scattering on individual nanotubes, which is a measure the electron-phonon coupling, i.e. how the device conductivity changes with

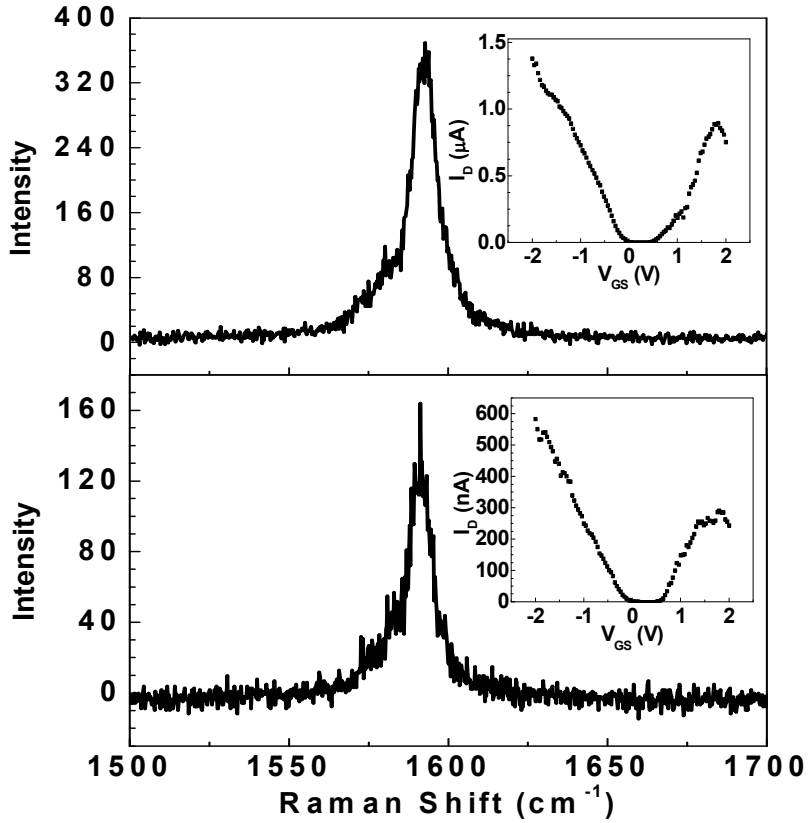

Figure 6.10: G-band Raman spectra collected for two SWNTs spanning two of the channels shown in Figure 6.9. Insets are corresponding transfer curves of top-gated devices with 100 mV of source-drain

varying electronic property of the SWNTs. In Figure 6.9 an AFM image of 7 consecutive single connection devices are shown along with the micro-Raman image corresponding to G-band intensity map of the same region with a 632 nm HeNe laser. As expected only a fraction of the nanotubes are resonant with the continuous laser source, and thus observed. Having large number of samples is critical for such a study. Therefore, having all the observed nanotubes aligned linearly in the same direction is critical for further

analysis. While a more detailed study for correlating device performances and Raman response of SWNTs is necessary, here we present examples of tangential mode Raman response of two single connection devices along with their transfer curves in Figure 6.10.

However, variations in contacts and other fabrication related issues make direct comparison of electrical and optical measurements difficult as exemplified in Figure 6.11 on minor sets of single connection devices. Figure 6.11 is an example of how electrical performances of single connection devices vary from device to device even on very small areas on a single chip, and why electrical data is only statistically meaningful by comparing our data to earlier studies on contacts.[19]

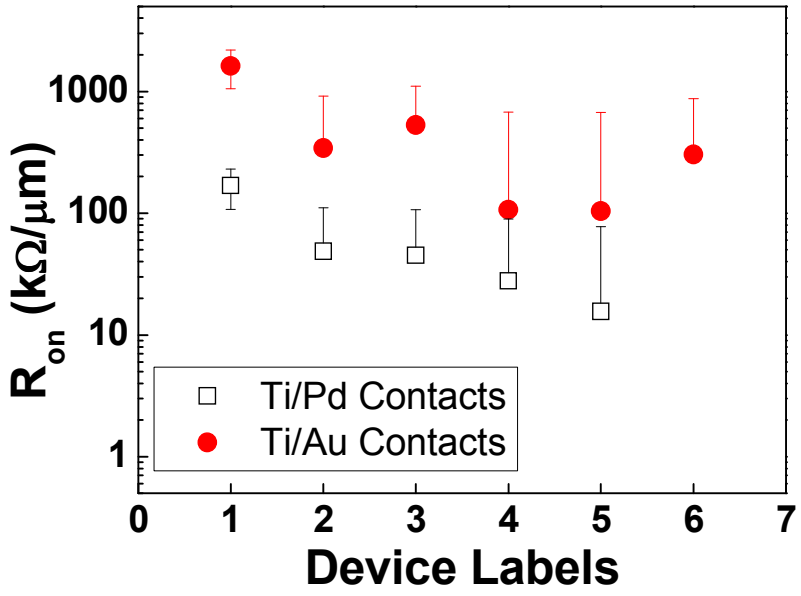

Figure 6.11: On-resistance given for two minor sets of devices with both Ti/Pd and Ti/Au contacts. The error bars are standard deviations of the data sets. Pd is known to make better electrical contacts with SWNTs than Au.[19]

Therefore, we rely on statistical analysis for comparison of electrical device performance and Raman scattering. On the other hand, a very obvious correlation

between Raman scattering and the electrical performance can be made by comparing the ratio of integrated D-band to G-band to the channel resistance. The ratio of integrated D-band to G-band is an indication of the defects on SWNTs. The exceptional electrical performance of SWNTs is degraded.

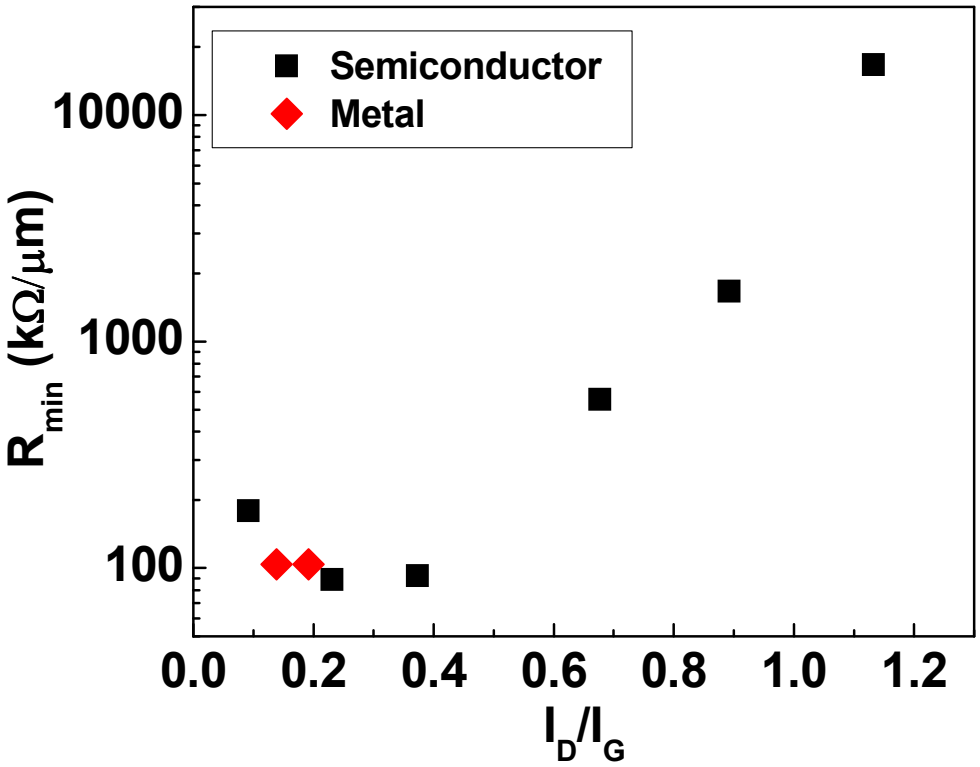

Figure 6.12: The on resistance of a set of single connection SWNT FETs with respect to integrated D- to G-band ratio.

We have offered several methods to fabricate large arrays of single connection devices by taking advantage of substrate template growth of perfectly linear and perfectly aligned SWNTs. We have analyzed the strength and the limitations of the proposed methods. We have observed that the number of connections for nanotube FETs follow a

Poisson distribution, and we can optimize and control the most probable outcome for number of nanotubes spanning the channel by selecting different effective channel widths and nanotube densities. Our work also shows that it is theoretically possible to improve the single connection device statistics beyond Poisson distribution if the catalyst size is reduced as such patterning has been shown to be possible by Javey et al.[18] We have also shown that complimentary Raman spectroscopy and electrical measurements can be used to correlate the structure and electrical performance of SWNTs within a statistical context. Future scientific studies can make use of these scalable methods to correlate electrical and Raman measurements, and future technical studies may combine our methods with more sophisticated catalyst patterning methods in order to realize perfectly scalable arrays of all single connection SWNT microelectronic devices.

6.3. Carbon Nanotube Crossbar Arrays & Molecular Memory Devices

Having discussed the possibility of realizing scalable arrays of single connection SWNT microelectronic devices, I will now suggest device designs that incorporate multiple layers of aligned SWNT arrays. In the previous chapter, I have mentioned that the arrays of aligned SWNTs grown on single crystal quartz can be transferred on different substrates. For our devices designs each layers of aligned SWNT arrays will be grown on separate substrates and will be transferred on the same donor substrate. In this section, I will first discuss the transfer-and-print process for SWNT arrays. I will then discuss the feasibility of our device designs.

6.3.1. Transfer and Print Method

Aligned arrays of SWNT grown on single crystal quartz substrates are transferred on other substrates by the help of a sacrificial Au and partially cured polymer membrane. Figure 6.13 summarizes the steps of the transfer-and-print process. 100 nm of Au is evaporated on SWNTs and subsequently a polymer layer is spin-coated on the Au layer.

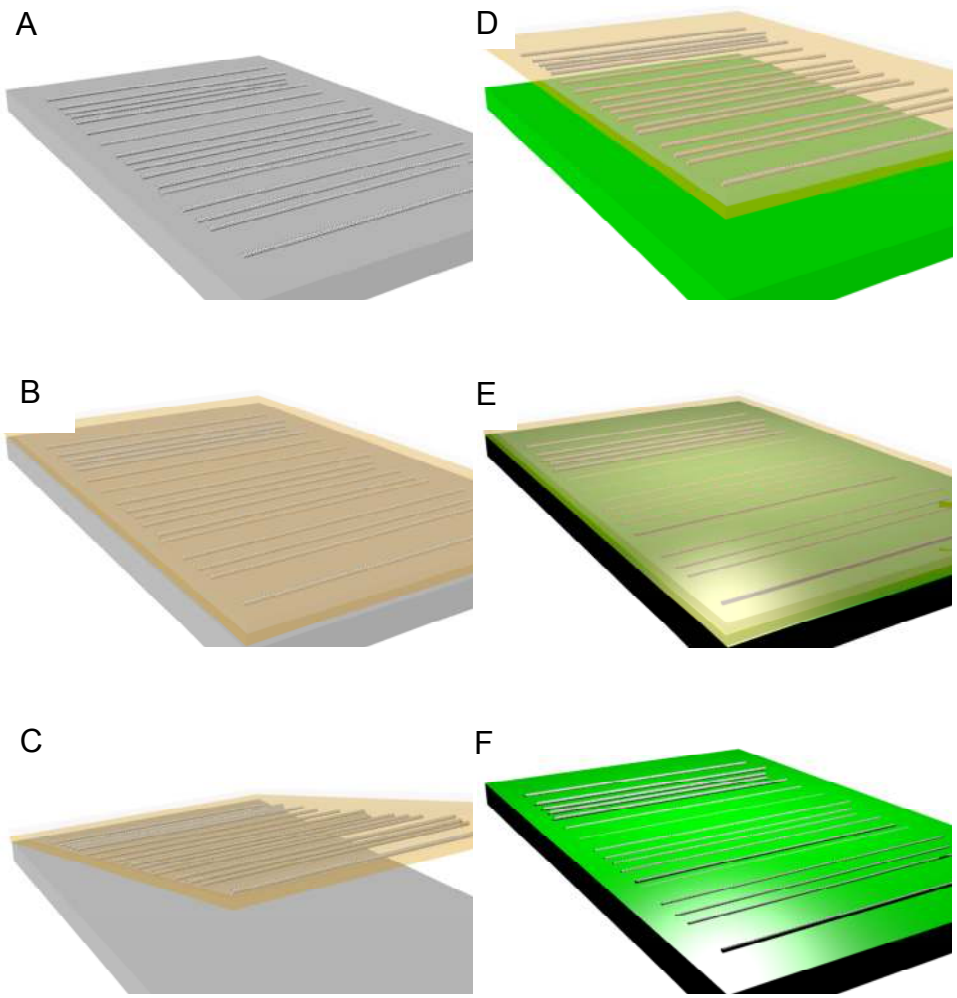

Figure 6.13: Schematics showing the steps of the process for SWNT transfer from a donor to another substrate. (a) Aligned arrays of SWNTs grown on a single crystal quartz substrate. (b) SWNTs are covered by a layer of Au and partially cured polymer such as PVA or PI. (c) SWNT-Au-Polymer film is peeled off the donor substrate. (d) The film is laminated on the acceptor substrate. (e) Polymer and Au are etched. PVA is etched by water and PI is etched in O_2 plasma. (f) Aligned arrays of SWNTs transferred on the acceptor substrate.

For our process we prefer to use either polyimide (PI) or 10 wt% polyvinylalcohol in DI water (PVA) as our sacrificial polymer layer. PI is applied by spin coating and PVA is applied by solution casting and both are partially cured at $80^0 C$ briefly (2-5 minutes). The edges of the SWNT-Au-polymer film are trimmed by a clean razor blade and the film is peeled off the quartz substrate and placed on top of the acceptor substrate. Once the polymer and Au layers are removed, transfer process is completed. PVA is dissolved in DI water and PI is typically etched by O_2 (80% O_2, 20% CF_4) plasma in an RIE (20 sccm of gas flow, 200 mTorr of chamber pressure, 100 W of power) for 30 minutes. After the polymer layer is removed, we etch Au by a KI based ionic solution (10% KI, 5% I_2 and 85 % DI water) instead of using acidic etchants so that the chemical integrity of SWNTs is protected. Electrical measurements carried out on transferred arrays of aligned SWNTs have not suggested any degradation of electrical conductivity after transfer process.[13] Figure 6.8 shows SEM images of arrays of transferred SWNTs on a Si/SiO_2 substrate. The spatial alignment of SWNT arrays is not affected by the transfer process.

6.3.2. Carbon Nanotube Crossbar Arrays

Carbon nanotube crossbar arrays have been realized by multiple methods. These methods have taken advantage of flow induced, electric-field induced alignment and electrospinning, but suffered from low yields of SWNT growth and/or complex synthesis methods.[20--22] On the other hand, transfer-and-printing of aligned arrays of SWNTs grown on crystalline substrates offer a relatively easier method to realize carbon nanotube arrays with controllable yields. It has already been shown that multiple layers of SWNTs

can be transferred on top of one another without any noticeable damage to underlying layers by forming superstructures of SWNTs including crossbar arrays.[14] We offer a set of devices which are fabricated on SWNT crossbar arrays. Even though SWNTs are very good conductors, tube-tube junctions are highly resistive.[23] Therefore, an immediate application of crossbar arrays of SWNTs is to fabricate arrays of Joule heaters localized to areas as small as ~ 1 nm^2. These nanoscale heaters can individually be controlled if individual SWNTs are electrically contacted. If the pitch between neighboring SWNTs is not controlled, the probability of an M by M array of single SWNTs to be contacted can be calculated by following Eq. 6.1. Therefore, the lower limit for the probability of getting a device of an M by M array is:

$$P_M = \left(e^{-n \cdot w} \cdot n \cdot w\right)^{2M}. \qquad \text{Eq. 2}$$

The probability exponentially decays as the size of the array increases if the intertube distance is random. Therefore, scalable SWNT crossbar array devices can be realized if the intertube distance can be restricted within a range.

6.3.3. Carbon Nanotube Molecular Memory

In the early days of carbon nanotube electronics, aligned arrays of SWNTs have been proposed to be the active electronic materials for a new keen of molecular random access memory devices.[24] The idea has been to separate two perpendicular layers of aligned arrays of SWNTs by a small air gap, and to make use of electrostatic attraction to attach or detach the SWNTs in the suspended layer to the underlying SWNTs so that bits of information is stored at each node. Only limited success has been achieved for

MWNTs and yet there has been no proof-of-concept devices have been demonstrated for aligned arrays of SWNTs.

Figure 6.14 summarizes the critical steps for a similar design of a memory device based on aligned arrays of SWNTs. In this design two perpendicular layers are separated by an thin layer of insulating amorphous material which changes into a crystalline phase once heated and becomes conducting. For instance $Ge_2Sb_2Te_5$ can be used as a phase changing material (PCM) for this purpose.[25] Reversible local changes in the electrical resistance of the PCM interface can be used to register bits of information at each node.

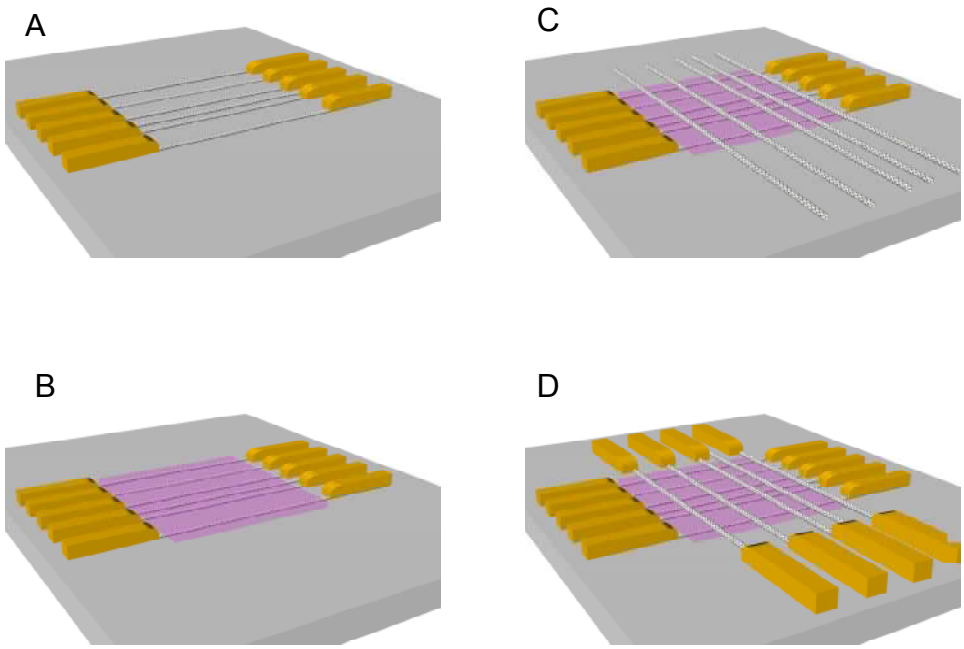

Figure 6.14: Schematics for a SWNT phase change data storage device. (a) Aligned SWNT arrays are contacted by lithographically patterned metal electrodes. (b) The channel is covered by a layer of phase change material. (c) Another layer of aligned arrays of SWNTs is transfer printed on top of the PCM perpendicular to the underlying layer of SWNT arrays. (d) The upper layer of SWNT arrays are electrically contacted by metal electrodes. The device shown is a 4 X 5 = 20 bit memory device.

Considering that the typical size of a NAND memory device is 1.5 cm^2 and horizontally aligned SWNTs can currently be grown at densities as high as 45 SWNTs per micron,[26] theoretically 38 GB of information can be stored in non-volatile PCM devices based on SWNTs with existing technology, which is comparable to the state of the art NAND flash memory devices. However future experiments are necessary to test this argument.

6.4. Conclusions

Here, I have offered molecular level devices that can be fabricated on aligned arrays on SWNTs in a scalable routine. Substrate template horizontal alignment of SWNTs and applicability of transfer-and-print method on SWNTs are milestones in SWNT electronics that have addressed many technical problems related to scalable fabrication of SWNT electronic devices. However better level of control on SWNT chirality and pitch sizes between neighboring SWNTs is essential prior to industrial production of the aforementioned scalable device designs.

6.5. List of References

[1] M. Shim, Mater. Matters **2**, 16 (2007).

[2] M. S. Arnold, A. A. Green, J. F. Hulvat, S. I. Stupp, and M. C. Hersam, Nat. Nanotech. **1**, 60 (2006).

[3] A. Nish, J. Hwang, J. Doig, and R. J. Nicholas, Nat. Nanotech. **2**, 640 (2007).

[4] M. Zheng and E. D. Semke, J. Am. Chem. Soc. **129**, 6084 (2007).

[5] C. J. Wang, Q. Cao, T. Ozel, A. Gaur, J. A. Rogers, and M. Shim, J. Am. Chem. Soc. **127**, 11460 (2005).

[6] M. Shim, A. Javey, N. W. S. Kam, and H. J. Dai, J. Am. Chem. Soc. **123**, 11512 (2001).

[7] G. P. Siddons, D. Merchin, J. H. Back, J. K. Jeong, and M. Shim, Nano Letters **4**, 927 (2004).

[8] T. Ozel, A. Gaur, J. A. Rogers, and M. Shim, Nano Lett. **5**, 905 (2005).

[9] A. Vijayaraghavan, S. Blatt, D. Weissenberger, M. Oron-Carl, F. Hennrich, D. Gerthsen, H. Hahn, and R. Krupke, Nano Lett. **7**, 1556 (2007).

[10] A. Ismach, L. Segev, E. Wachtel, and E. Joselevich, Angew. Chem. Int. Ed. **43**, 6140 (2004).

[11] S. Han, X. Liu, and C. Zhou, J. Am. Chem. Soc. **127**, 5294 (2005).

[12] C. Kocabas, S. H. Hur, A. Gaur, M. A. Meitl, M. Shim, and J. A. Rogers, Small **1**, 1110 (2005).

[13] S. J. Kang, C. Kocabas, T. Ozel, M. Shim, N. Pimparkar, M. A. Alam, S. V. Rotkin, and J. A. Rogers, Nature Nanotech. **2**, 230 (2007).

[14] S. J. Kang, C. Kocabas, H. S. Kim, Q. Cao, M. A. Meitl, D. Y. Khang, and J. A. Rogers, Nano Lett. **7**, 3343 (2007).

[15] P. G. Collins, M. S. Arnold, and P. Avouris, Science **292**, 706 (2001).

[16] A. Liao, Y. Zhao, and E. Pop, Phys. Rev. Lett. **101**, 256804 (2008).

[17] C. Kocabas, S. J. Kang, T. Ozel, M. Shim, and J. A. Rogers, J. Phys. Chem. C **111**, 17879 (2007).

[18] A. Javey and H. Dai, J. Am. Chem. Soc. **127**, 11942 (2005).

[19] A. Javey, J. Guo, Q. Wang, M. Lundstrom, and H. J. Dai, Nature **424**, 654 (2003).

[20] S. Huang, B. Maynor, X. Cai, and J. Liu, Adv. Mater. **15**, 1651 (2003).

[21] J. Gao, A. Yu, M. E. Itkis, E. Bekyarova, B. Zhao, S. Niyogi, and R. C. Haddon, J. Am. Chem. Soc. **126**, 16698 (2004).

[22] A. Ismach and E. Joselevich, Nano Lett. **6**, 1706 (2006).

[23] M. S. Fuhrer, J. Nygard, L. Shih*, et al*, Science **288**, 494 (2000).

[24] T. Rueckes, K. Kim, E. Joselevich, G. Y. Tseng, C. Cheung, and C. M. Lieber, Science **289**, 94 (2000).

[25] J. Hegedus and S. R. Elliott, Nat. Mater. **7**, 399 (2008).

[26] S. W. Hong and J. A. Rogers, submitted to Adv. Mater. (2009).

CHAPTER 7

CONCLUSIONS

Single-walled carbon nanotubes (SWNTs) are promising materials for future high performance electronics. However, uncontrolled variations in characteristics and lack of scalable methods to integrate SWNTs into electronic devices are current obstacles for device applications of individual SWNTs. One relatively new direction in SWNT electronics, which avoids these issues, is using arrays of SWNTs, where the ensemble average may provide uniformity from device to device, and this new breed of electronic material can be integrated into electronic devices in a scalable fashion.

In this dissertation, I have described methods for characterization of SWNT arrays (Chapters 1-2), how the electrical transport in these two-dimensional arrays depends on length scales and spatial anisotropy (Chapter 3), the interaction of aligned SWNTs with the underlying substrate (Chapter 4-5), and methods for scalable integration of SWNT arrays into electronic devices (Chapter 6).

The electrical characterization of SWNTs by polymer electrolyte-gating has been shown to addresses many technical difficulties inherent to electrical characterization by gating through oxide-dielectrics, including hysteresis-free measurement, n-type operation in air, and highly-efficient gating. Having shown polymer electrolyte-gating can also be successfully applied on SWNT arrays; the length scaling dependence of electrical transport in SWNT arrays has been studied experimentally. The experimental data has been compared to a two-dimensional stick percolation model, which gives a good

qualitative picture of the electrical transport in SWNT arrays in terms of surface coverage, length scaling, and spatial orientation. We have observed that the resistance of a random network of SWNTs in the form of a sub-monolayer film is indeed non-linear with the normalized length across which the transport occurs. The two-dimensional electrical transport has been shown to depend not only on the length scales, but also on the nanotube-nanotube junction resistances and the spatial orientation of SWNTs in the two-dimensional film. The carrier mobilities for random networks of SWNTs have been shown to be ~ 2 orders of magnitude smaller than the carrier mobilities individual SWNTs. This observation has been attributed mostly to the existence of highly resistive nanotube-nanotube junctions in random networks. The nanotube-nanotube junction resistances contribute to the overall resistance of the random network proportional to the channel length. Therefore, aligned arrays of SWNTs have been studied and compared to the random networks.

The growth of aligned arrays of SWNTs in a moderately easy and scalable fashion has allowed us to study the electrical transport in anisotropic arrays of SWNTs. However, the effects of the anisotropic interactions associated with the quartz lattice and SWNTs, which allow near perfect horizontal alignment on substrate along a particular crystallographic direction, were not known. In order to address this issue, we have compared the substrate-SWNT interactions for random networks of SWNTs grown on Si/SiO_2 substrates and aligned arrays of SWNTs grown on single crystal quartz substrates by Raman spectroscopy. We have demonstrated that the interaction between the crystal quartz substrates and aligned SWNTs leads to uniaxial compressive strain in as-grown SWNTs. This has been the first experimental demonstration of the hard-to-achieve

uniaxial compression of SWNTs. Temperature dependence of Raman G-band spectra along the length of individual nanotubes has revealed that the compressive strain is non-uniform and could be larger than 1% locally at room temperature. I have argued that the substrate-induced uniaxial compression should, theoretically, have minimal effects on the ensemble electrical characteristics of aligned arrays of SWNTs, even though the bandgaps of individual SWNTs are expected to alter. We have also observed that typical device fabrication steps releases the uniaxial strain induced by single crystal quartz substrates.

Based on our findings, there have been discussions about device performances and designs included in this dissertation. The channel length dependences of device mobilities and on/off ratios of SWNT thin film transistors have been elucidated. Time response of polymer-electrolyte gated SWNT TFTs has been measured to be ~300 Hz, and a proof-of-concept logic inverter has been fabricated by using polymer electrolyte gated SWNT TFTs for macroelectronic applications. Finally, I have suggested scalable device designs based on aligned arrays of SWNTs, including a design for SWNT memory devices.

VITA

Taner Ozel was born in Eskisehir, Turkey in 1981. In the early years of his education, he was supported by *the State Boarding School Scholarship of the Turkish Government* (‘92-‘96), *Fatih Science High School Fellowship* (’96-‘99), *Bilkent University Fellowship* (’99-‘03), and *the Scholarship of the Scientific and Technical Research Council of Turkey* (’00-‘03). He received his B.S. in physics from Bilkent University (Ankara, Turkey), ranking first in his class, in 2003. Beginning graduate study in Physics at the University of Illinois at Urbana-Champaign in 2003, he received his M.S. in 2004. During graduate school, he developed a keen interest in materials physics, solid state device physics, nanotechnology and optical spectroscopy. He worked towards his doctoral dissertation under the supervision of Prof. Moonsub Shim. Following graduation, Taner is scheduled to join the Laboratory of Chemical Physics in the National Institutes of Health as a postdoctoral fellow.